THE SEARCH FOR LIGHTLY IONIZING PARTICLES IN THE LARGE UNDERGROUND XENON DETECTOR

A Dissertation

by

PAUL AUGUST TERMAN

Submitted to the Office of Graduate and Professional Studies of
Texas A&M University
in partial fulfillment of the requirements for the degree of

DOCTOR OF PHILOSOPHY

Chair of Committee,	Robert C. Webb
Committee Members,	Bhaskar Dutta
	David Toback
	Sherry Yennello
Head of Department,	Grigory Rogachev

August 2020

Major Subject: Physics

ABSTRACT

Observations as early as the 1930s indicated significant disagreements between anticipated gravitational galactic rotations based upon solar luminous intensity and the observed rotations of galaxies. The cause of the observed increased rotational velocity in galaxies was ascribed to a large invisible mass termed $dark\ matter$. Various indirect observations affirmed the notion of dark matter and also suggested that the dark matter consists of non-baryonic material. Dark matter currently stands as one of the great mysteries in modern physics.

A leading candidate for dark matter is known as the Weakly Interacting Massive Particle (WIMP) which nicely fits dark matter projections. The Large Underground Xenon (LUX) experiment, located in the Homestake Mine of the Sanford Underground Research Facility (SURF), was a xenon-based direct detection experiment designed and built for the detection of WIMPs. LUX had a dual-phase Time Projection Chamber (TPC) which allowed for precise energy and position reconstruction of events. Reanalyzing the LUX data, it becomes possible to search for more exotic theoretical dark matter forms and new physics.

The Lightly Ionizing Particle (LIP), a theoretical particle with a charge of $f \cdot e$ with $f < 1$ and e the electron charge, arises in a variety of dark matter conceptions associated with additional dark sectors as well as other physical constructs such as monopoles and quantized charges. This work seeks to use data from the first underground run of LUX Run03, and reanalyze it to search for tracks in the detector as a result of LIP interactions. Throughout the reanalysis new techniques in simulation, data analysis, and data processing are developed, including pulse $chopping$ to separate merged signals. The LIP search, making use of traditional cut methods as well as machine learning for event classification, places new limits on LIP flux in the charge range $0.01e$ to $0.3e$ as low as 10^{-10} cm^{-2} s^{-1} sr^{-1}.

DEDICATION

For my parents, of blessed memory.

ACKNOWLEDGMENTS

ב''ה

With God's Help

First, I would like to thank Bob Webb for the countless hours working on ideas, poring over graphs and waveforms, and figuring out how to make the analysis work. You showed me the wonderful world of experimental physics, as well as the value of dedication and persistence. Thank you to my lab mates Ty Stiegler, Rachel Mannino, the late James White, and especially Clement Sofka.

I would like to thank the entire LUX experiment team of researchers who supported my work and provided me with the amazing opportunity to work as part of the experiment. Many people helped me, in small ways and in big ways, over the course of this work. To the LUX group at Brown University, Rick Gaitskell, Samuel Chan, Casey Rhyne, Will Taylor, and especially DQ Huang for taking me in as part of your team and for helping me to understand the many details of LUX software. Scott Hertel, I appreciate your early suggestions regarding pulse $chopping$. Thank you, Matthew Szydagis for getting me started with simulations. Kate Kamdin, thank you for your work on the MUSUN based generator for simulations, and your aid with the LIP filter. Thank you, Scott Kravitz, as well as the Machine Learning Group, for teaching me machine learning techniques. I would especially like to thank Jingke Xu, who is a brilliant person of many talents. Jingke, thank you for your help with adding the monopole package to LUXSim, for your guidance regarding data analysis cuts, and your overall spirit of encouragement throughout this process; not only did you make my analysis stronger, but also I could not have done this without you. Although I was isolated for much of my time in the collaboration, the support all of you provided from afar proved integral. Thank you to the now-former LUX group at Yale University, because it was through you that I met my beloved wife, Sharon.

I would like to thank my parents for always working to try to do the best for me. You were taken from me far too soon; I wish that you could have seen me reach this accomplishment. I would especially like to recognize my mom, who sacrificed throughout my early education, who fought for me at every opportunity, and who taught me that I could do anything I set my mind to.

I could not have done this without the memory of your guiding light.

To Holly and David Davies, as well as the boys, Morgan, Jonah, and Jacob, thank you for making me part of your family. Thank you for your love, encouragement, and care. Thank you for being with me in times of joy and for being there for me in times of struggle.

To all those friends and family who helped me throughout my life, to Aunt Sherry, Grampa Irv, Steve and Marsha Rudin, Matt Grant, Rabbi Plotkin, and many others, thank you for being there for me. You have all given me strength and wisdom over the years.

To my beloved Sharon, thank you for being a part of my life. I know that you have worked hard to support me and to give me strength. Your hugs, smiles, and kind words always touch my heart. Also, thank you for helping to edit this dissertation. To my dear daughter, Esther Bracha, though you are new to the world your constant curiosity about the world is a refreshing representation of what it means to be a true scientist. I hope that this dissertation can serve as an example of the benefit of perseverance, as well as show you a glimpse of the wonders of the universe. I cannot wait to see what you will do and what you will discover.

CONTRIBUTORS AND FUNDING SOURCES

Contributors

This work was supported by a dissertation committee consisting of Professor Robert C. Webb, and Professors Bhaskar Dutta and David Toback of the Department of Physics & Astronomy and Professor Sherry Yennello of the Department of Chemistry.

The data analyzed was collected by the Large Underground Xenon (LUX) dark matter search experiment.

All other analyses conducted for this dissertation were completed by the student independently.

Funding Sources

Research was supported by Ed Rachel Chair in High Energy Physics at Texas A&M University and U. S. Department of Energy Grant Number DE-SC0010813.

NOMENCLATURE

ACRS	Automated Controlled Recovery System
ALP	Axion Like Particle
ASP	Anomalous Single Photon experiment
BBN	Big Bang Nucleosynthesis
BDT	Boosted Decision Tree
CDMS	Cryogenic Dark Matter Search
CMB	Cosmic Microwave Background
CP	Charge-Parity
DAQ	Data AcQuisition system
D-D	Deuterium to Deuterium neutron generator
DOF	Degrees Of Freedom
DPF	Data Processing Framework
EPTL	Energy Per Track Length
FCP	Fractionally Charged Particle
GMSB	Gauge-Mediated Supersymmetry Breaking
IQ	Important Quantity
LHC	Large Hadron Collider
LIP	Lightly Ionizing Particle
LLNL	Lawrence Livermore National Laboratory
LRF	Light Response Function
LSD	Liquid Scintillation Detector
LUX	Large Underground Xenon detector

LZ	LUX-Zeplin detector
MACHO	MAssive Compact Halo Object
MACRO	Monopole, Astrophysics, and Cosmic Ray Observatory
MJD	MaJorana Demonstrator experiment
MSM	Minimal Standard Model
MSSM	Minimal Supersymmetric Standard Model
MUSUN	MUon Simulated UNderground
NEST	Noble Element Simulation Technique
PAI	Photo-Absorption Ionization
PA(PS)	Pulse Area (Per Sample)
PDG	Particle Data Group
PMT	Photo-Multiplier Tube
POD	Pulse Only Digitization
PTFE	PolyTetraFluoroEthylene
PVC	PolyVinylChloride
QCD	Quantum ChromoDynamics
RQ	Reduced Quantity
S1	Primary scintillation pulse
S2	Secondary scintillation pulse caused by ionization
SDP	Single Detected Photon, comparable terminology to single photoelectron or sphe
SE	Single Electron, same as a single liquid electron
SLAC	Stanford Linear Accelerator Complex
SM	Standard Model
SRP	Select ReProcessing of the DPF
SRV	Storage and Recovery Vessel

STP	Standard Temperature and Pressure
SURF	Sanford Underground Research Facility
SUSY	SUperSYmmetry
TPC	Time Projection Chamber
WIMP	Weakly Interacting Massive Particle

TABLE OF CONTENTS

Page

LIST OF FIGURES

FIGURE Page

LIST OF TABLES

TABLE Page

1. INTRODUCTION

1.1 The Question of Dark Matter

> "[I]t seems probable that most of the grand underlying principles have been firmly established, and that further advances are to be sought chiefly in the rigorous applications of these principles to all the phenomena which come under our notice."
> - A. A. Michelson, 1894 [1]

The sentiment that all of the underlying principles of physics have been discovered and all that remains is to calculate the numbers was a notion that occurred within the physics community in the late 19th century. However, not too much time had passed before the aforementioned feeling had changed and the universe appeared more complex than it had initially.

1.1.1 Missing Mass

In 1933, Fritz Zwicky observed, using red-shift measurements, objects within the Coma Cluster rotating at a relative velocity much greater than expected based upon calculations of the velocity accounting for all of the estimated visible mass within the cluster [2]. Zwicky compared his observation to the standard Virial Theorem calculation where the average kinetic energy $\langle K \rangle$ is equal to half of the average potential energy $\langle V \rangle$ of the system, $\langle K \rangle = -1/2 \langle V \rangle$ with

$$\langle K \rangle = \sum_{i=1}^{N} M_i \langle v_i^2 \rangle \tag{1.1}$$

where M_i and v_i are the mass and velocity of each member in the system of N mechanically bound components. Assuming that the mass is uniformly distributed in a sphere of radius R then

$$V = \frac{-3GM_{total}^2}{5R} \tag{1.2}$$

with M_{total} now representing the total mass of the cluster, and G being the universal gravitational constant. It is also possible to write

$$\sum_i M_i \langle v_i^2 \rangle = M_{total} \langle \overline{v^2} \rangle \tag{1.3}$$

with $\langle \overline{v^2} \rangle$ denoting an average over time and average over mass. Finally, putting these together, the total mass of the cluster becomes [3]

$$M_{total} = \frac{5R\langle \overline{v^2} \rangle}{3G} \tag{1.4}$$

Taking into account the above calculation, observing a velocity distribution of 700 km/s, Zwicky found the mass of the cluster to be $4.5 \cdot 10^{13}$ solar masses with 1,000 nebulae, hence an average of $4.5 \cdot 10^{10}$ solar masses per nebula. Whereas calculations of the average mass of the nebulae based upon their luminosity found that the cluster should contain $8.5 \cdot 10^7$ solar masses [3]. Thus, Zwicky concluded that the luminous to non-luminous ratio of masses differed by approximately a factor of 500. Such a great discordance between calculations indicated a large unseen mass within the cluster. At that time, Zwicky, whilst using the term *dark matter*, thought that it referred to a mass of matter in the form of cooler stars, interstellar gas, and other bodies. His conception of dark matter was not something that did not interact with luminous matter, but rather something unseen, which could also be acting as a visual dampener, blocking luminous matter from observation. Similar observations of the Virgo Cluster by Smith [4], the NGC 3115 Galaxy by Oort [5], and the Andromeda Galaxy by Babcock [6] yielded luminous to dark matter ratios of 200, 250, and 50, respectively. While the later observations showed smaller luminous to dark matter discrepancies, the ratios remained a concern.

In 1970, Rubin and Ford gathered data that would further indicate the existence of dark matter by observing HII and NII emissions to determine the rotational velocity of objects within the Andromeda Galaxy [7]. The measurements of Rubin and Ford made use of new technology called the spectrograph which used HII emissions to measure objects within 3 kpc of the galactic center

and the narrow NII line for objects between 3 to 24 kpc of the galactic center. Based upon the amount of luminous matter, Rubin and Ford expected the velocity profile of the galactic rotation curve to be greater nearer to the galactic center, whilst further from the center the velocity profile would diminish. However, the observed result showed a decreased velocity near the center and indicated an increase and later flattening out of the velocity profile of rotating stars which indicated large unseen masses farther out in the galaxy, which appears in figure 1.1 [7]. By 1980, there were galactic rotational curves calculated for 21 galaxies showing similar results indicating faster rotational velocities at distant radii. The additional calculated rotation curves indicated that the initial observations of Rubin and Ford were not a mere mischance of observation or anecdotal happenstance of the Andromeda Galaxy but instead revealed a fundamental notion of the universe; that fundamental notion being that there appeared to exist large quantities of unseen mass or *hidden mass* beyond the stars of the galactic plane, which became part of the foundation of indirect evidence for dark matter in the universe.

A simple illustration of the problem of angular velocity can be shown approximating the trajectory of stars around the galactic center as circular, it becomes possible to apply Newtonian mechanics to the system. Newton's second law summarized as a force F equals mass m times acceleration a can be applied to centripetal force, where v_r is the rotational velocity, and r is the circular path radius.

$$F = m \cdot a = \frac{m v_r^2}{r} \tag{1.5}$$

Similarly, Newtonian gravity states that

$$F = \frac{GMm}{r^2} \tag{1.6}$$

where G is the gravitational constant and M is the mass of all objects within radius r.
Setting equal equations 1.5 and 1.6 and solving for v_r gives the result

$$v_r = \sqrt{\frac{GM}{r}} \tag{1.7}$$

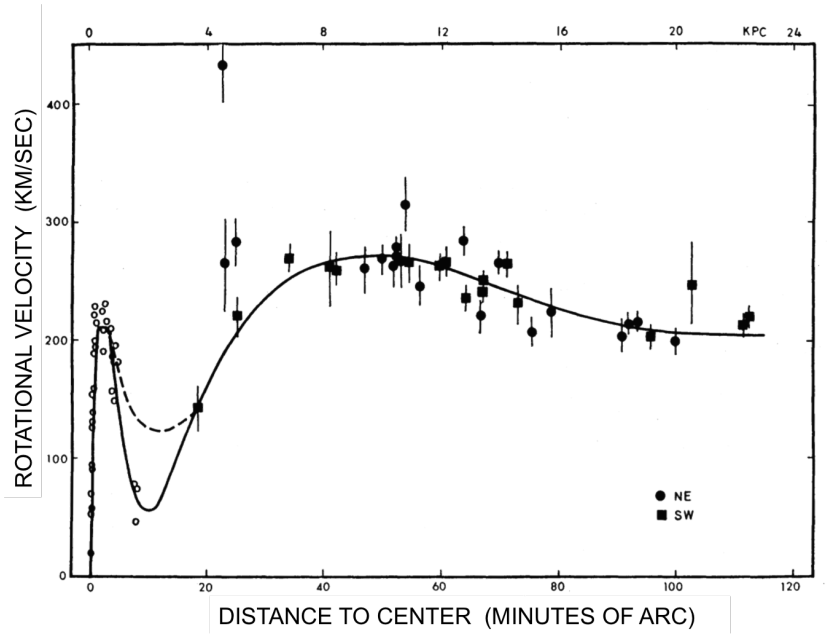

Figure 1.1: Rotational velocity vs distance to galactic center for objects in the Andromeda Galaxy (M31). The solid curve is the fit for a 5th order polynomial when $R \leq 12'$ and 4th order for $R > 12'$ which is required to be flat at $R = 100'$. The dashed curve at $R = 10'$ is a second rotation curve with a higher inner minimum. Image came from the data of Rubin and Ford reprinted from [7].

The above result of course has proportionality to $\frac{1}{\sqrt{r}}$, and if there existed only a $\frac{1}{\sqrt{r}}$ dependence then the rotational velocity would decrease according to the radius. However, if there existed a larger mass incorporated within the radius r, it must require that M exists as a non-negligible function of radius. Thus,

$$v_r(r) = \sqrt{\frac{GM(r)}{r}} \tag{1.8}$$

With large enough increased mass in the extremities, the $\frac{1}{\sqrt{r}}$ decease could be counteracted and arrive at the observed velocity profiles. Similar calculations would show the same dependence on mass and radius for objects with non-circular obits as well.

1.1.2 Gravitational Lensing

Additional experiments noted gravitational lensing, which caused distortion or duplication of celestial images occurring in regions of space where no mass appeared to exist [8]. Gravitational

effects of dark matter play an important role in the understanding of dark matter because it does not emit or reflect electromagnetic radiation, instead primarily interacting with regular matter via gravity. Gravity will deflect an approaching light ray with an angle defined by

$$\theta_{Deflection} = \frac{4GM}{c^2 b} \tag{1.9}$$

where M is the deflecting object mass, c is the speed of light, and b is the distance between the light ray path and the center of the deflecting object.

Strong lensing is where there exists a high-mass object in the line of sight of the source object which produces the light ray, and that high-mass object has sufficient mass to create multiple images of the source object. At times when strong lensing occurs, light becomes deformed into a ring around the object known as an Einstein ring. The result of strong lensing comes from the fact that light rays traverse different paths as they curve past the massive object. Weak gravitational lensing, in contrast, occurs when light from a source object becomes merely distorted, elongated, or magnified due to gravitational effects of weaker magnitude. Between strong and weak lensing, flexion curvature describes small arc effects. Even weaker than weak lensing is called micro-lensing, which would otherwise be too small to detect, but can be observed by noting small fluctuations in light in an area of space over time, as the massive object passes the light source. Studies that observe gravitational lensing around seemingly empty space would indicate the presence of large unseen pockets of dark matter. The mass of the dark matter in a region in which gravitational lensing is observed can be calculated based upon the extent to which an image becomes distorted.

Perhaps the most famous of all stellar objects illustrating the existence of dark matter as inferred by gravitational lensing is the Bullet Cluster, which is actually a galaxy cluster that has resulted from the collision of two previous clusters. In the case of the Bullet Cluster, the two previously existing galaxies or proto-clusters have passed through each other. Gravitational lensing observations combined with measurements of x-rays coming from interstellar gas have shown interactions between the respective gases from the proto-clusters which trail behind the clusters [10].

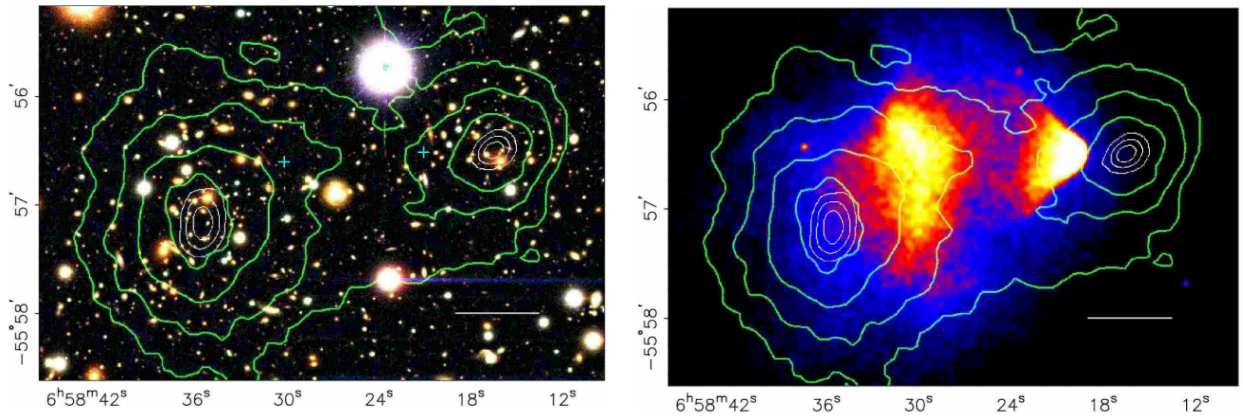

Figure 1.2: The left shows the visible light image of the Bullet Cluster made by the Magellan telescope. The right shows the Chandra x-ray image of the same region in false color. Weak lensing contour peaks of 1σ, 2σ, and 3σ confidence level overlay both images. Figure reprinted from [9].

The interstellar gas, which is baryonic matter, has emitted x-rays upon collision with gas from the second proto-cluster and has had its velocity greatly diminished in the process. The slowing of interstellar gas in this fashion, referred to as *bow shock*, exists as a well-understood notion in astrophysics, with the Bullet Cluster considered a prime example of the *bow shock* phenomenon [11]. Weak lensing of the cluster indicates the majority of the mass has followed the visible stellar component of the proto-clusters, with the stars passing each other without interaction, the expected characteristic of dark matter as shown in figure 1.2. Observations of x-rays coming from the gas have indicated a separation in the mass peaks of the gas, being baryonic matter, and the non-visible matter implied by gravitational lensing with a spacial offset of 8σ confidence [9]. Therefore, the interstellar gas cannot explain the gravitational lensing, hence the majority of the matter in the cluster must be dark matter.

1.1.3 Cosmic Microwave Background

The Cosmic Microwave Background (CMB), an observed phenomenon where the universe contains isotropic microwave photons conforming to a blackbody spectrum, has provided even further evidence for the existence of dark matter. The early universe had temperatures so high as

to prevent the formation of neutral hydrogen. Baryonic matter and photons were held in thermal equilibrium where the photons provided a net negative pressure on the baryonic matter to counteract gravitational attraction of the baryonic matter. Photons could only interact with the baryonic matter due to the inability of photons to interact with cold dark matter. However, as the universe cooled, the photons in the primordial plasma lost sufficient energy to allow for neutral hydrogen to form, called recombination. The era of recombination, about 350,000 - 400,000 years after the Big Bang, resulted in a universe optically transparent to photons, meaning that the photons could decouple from matter. In this slightly cooler state of the universe, baryonic matter began to undergo sonic manipulation, propagating sound waves, the initial conditions of which came from fluctuations in cosmic inflation. The propagation of sound waves left the cold dark matter free to clump gravitationally, resulting in pockets of higher mass density as the universe expanded, and due to the optical transparency of the universe this was when photons from the CMB had been formed [1] [12]. Any relativistic dark matter, if it existed, would have escaped the gravitational wells produced from the cold dark matter clumping. As the universe expanded and cooled, gravitational pressure from the dark matter in the gravity wells would overpower the photonic pressure, and it would cause baryonic matter to amass alongside dark matter. The universe at recombination released the photons, which would no longer interact with free electrons and no longer maintain equilibrium with gravitational effects. The released photons would make up the CMB, and the gravity compressed fundamental wave became frozen in that phase. Thus, there would exist a higher temperature in areas where there had been less mass.

Though mostly uniform, the CMB retains areas of higher signal density which correlate to areas in the universe that contain matter. Indeed, regions of space devoid of visible matter appeared to have a mass density when cosmic microwave background experiments showed an excess signal in those regions [14]. The universe has cooled with expansion, retaining a relic temperature decreasing with time t proportionate to $t^{-1/2}$. These photons have cooled from ~ 3000 K during recombination to 2.7377 ± 0.0038 K today, which agrees with a black body spectrum [15].

[1] Any connection of the propagation of sound waves in the universe to other notions shall be left to philosophers and theologians.

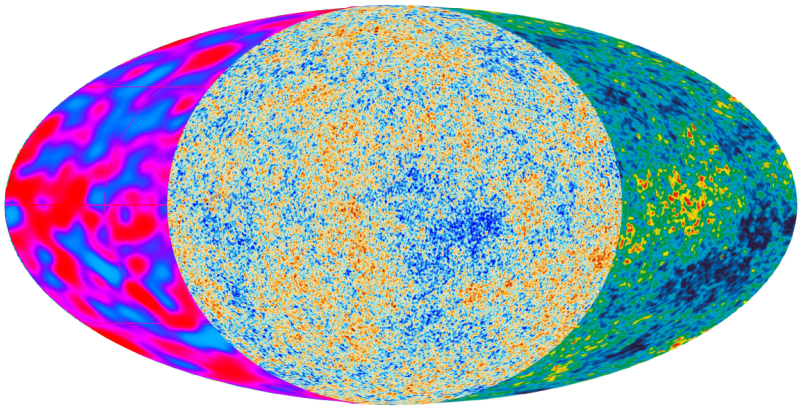

Figure 1.3: Overlay of the COBE (left), WMAP (right), and Planck (center) full sky maps which show temperature fluctuations of the CMB between -300 and +300 μK from dark blue to dark red. Note the improved sensitivity going from COBE to WMAP to Planck, the latter being the most sensitive. Figure reprinted from [13].

The first measurement of the CMB occurred in 1964 when Penzias and Wilson measured it as background noise in their communications antenna [16]. Since that initial detection, there have been several dedicated measurements taken of the CMB from the COBE, WMAP, and Planck satellite missions each providing more precise energy measurements than the one which preceded it (see figure 1.3). These missions provided strong evidence for Big Bang Cosmology as well as further evidence for cold dark matter.

A mathematical framework can provide further insight into CMB formation. The height and location of very tiny peaks in the power spectrum indicate various features of the universe. Spherical harmonics expansion can describe the fluctuations in temperature T_{fluct} given as [17]

$$T_{fluct}(\theta,\phi) = \sum_{l=0}^{\infty} \sum_{m=-l}^{l} a_{lm} Y_{lm}(\theta,\phi) \tag{1.10}$$

where l is the multipole number, which could be considered analogous to the k wave number in a Fourier decomposition. The monopole term occurs when $l = 0$ and represents the mean temperature. The $l = 1$, or dipole, term represents the Doppler shift resulting from the velocity of the Earth, including solar, galactic velocity, etc. relative to CMB radiation. Higher-order values of

l contain much more interesting information for further discussion.

Values of l equal to 2 or higher indicate the density perturbations of the early universe which became fixed at recombination. The values $l = 0$ and $l = 1$ are not of interest because only temperature fluctuations are relevant. Similarly, the power spectra could be redefined as the relative temperature variation $\Theta(\hat{n})$ at some direction $\hat{n}$

$$\Theta(\theta, \phi) = \frac{T(\theta, \phi) - \langle T \rangle}{\langle T \rangle} \tag{1.11}$$

$$\Theta(\hat{n}) = \sum_{l=2}^{\infty} \sum_{m=-l}^{l} b_{lm} Y_{lm}(\theta, \phi) \tag{1.12}$$

Parameterization of the sky coefficients averaged over all points in the sky with the same angular separation θ gives $C(\theta) = \langle \Theta(\hat{n}) \Theta(\hat{n}') \rangle_{\hat{n} \cdot \hat{n}' = \cos\theta}$. which is the angular correlation function. Substituting the above equation 1.12 for $\Theta(\hat{n})$ into the value for $C(\theta)$ gives

$$C(\theta) = \sum_{ll'mm'} \langle b_{lm} b^*_{l'm'} \rangle Y_{lm}(\theta, \phi) Y^*_{l'm'}(\theta', \phi') \tag{1.13}$$

Note that due to orthonormality

$$\langle b_{lm} b^*_{l'm'} \rangle = \delta_{ll'} \delta_{mm'} C_l \tag{1.14}$$

where the δ functions are Kronecker deltas. Substituting the Y_{lm} terms for Legendre polynomials P_l gives [18]

$$C(\theta) = \frac{1}{2\pi} \sum_{l=2}^{\infty} l \left(l + \frac{1}{2} \right) C_l \frac{P_l(\cos\theta)}{l} \tag{1.15}$$

The associated plotted angular power spectra of the temperature fluctuations is given by

$$D_l = \frac{l(l+1)}{2\pi} C_l \tag{1.16}$$

where one should note that there the quantities no longer have an m dependence, and l has a correspondence to the θ value, being approximately $l \sim 180°/\theta$. Values for D_l can be seen in

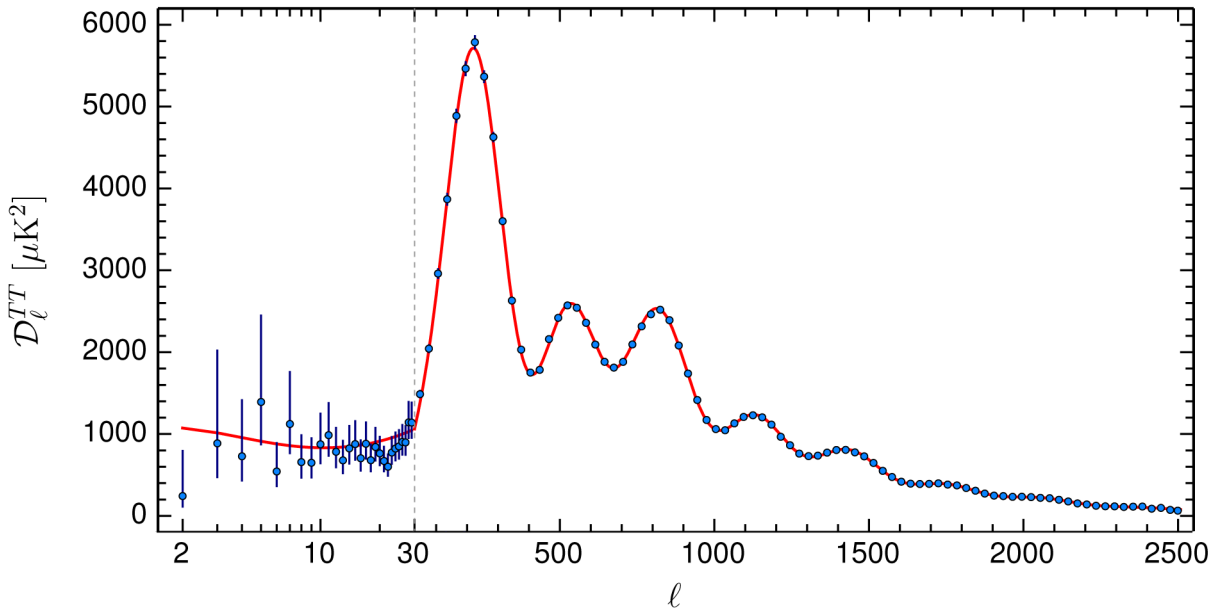

Figure 1.4: This figure shows the Cosmic Microwave Background anisotropy power spectrum reprinted from the 2015 Planck collaboration results [19]. The dashed vertical line indicates where the scale shifts from log to linear on the x-axis, which notes the multipole value l. The red line shows the best fit for a six parameter ΛCMB cosmology.

figure 1.4.

Local maxima and minima in the power spectrum give insight to physical phenomena, with odd peaks showing over-densities or compression modes and even peaks showing under-densities or expansion modes, both resulting from the previously mentioned sonic manipulations. The presence of baryons causes inertia which breaks the symmetry between both modes and creates a separation in the peaks favoring compression [20]. Therefore, the CMB power spectrum will have a net higher power for the odd peaks compared to the even peaks. All matter in the universe, both baryonic and dark matter, drives the oscillator for the odd peaks, while only the baryonic component affects the even peaks. Thus, the measurement of the second and third peaks will give an estimate of the baryonic proportion of the universe Ω_B compared to the total matter Ω_m.

The position of the first peak indicates the dark energy density Ω_Λ, and curvature of the universe Ω_k. Whether the distance light can travel since recombination is less, more, or equal to the apparent distance indicates whether the universe is open, closed, or flat. The shape of the universe

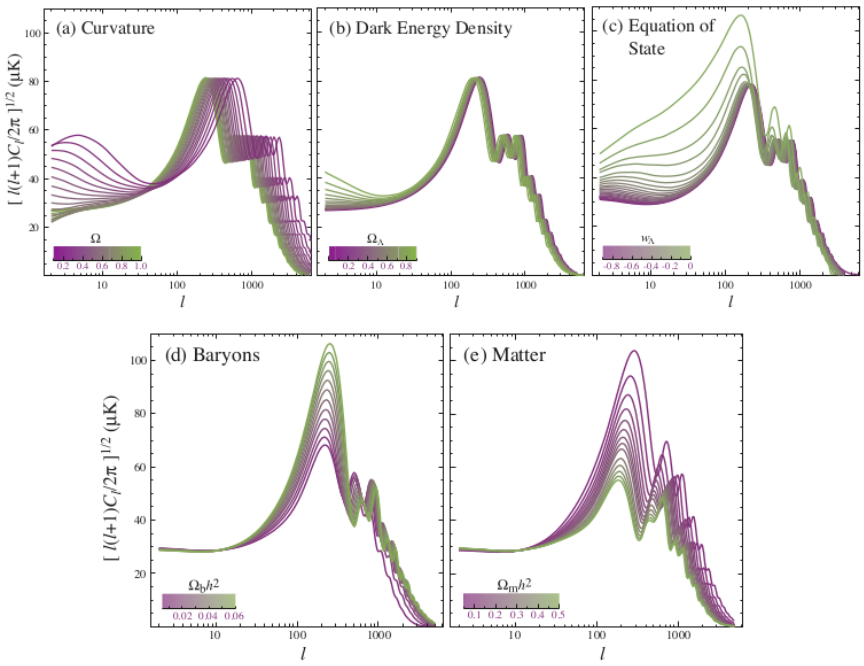

Figure 1.5: These figures show the effect of universe curvature (a), dark energy proportion (b), equation of state (c), baryonic matter proportion (d), and total matter proportion (e) on the magnitude and location on CMB power spectrum peaks as a function of the multipole. Figure adapted from [20].

is dependent upon the aforementioned distance because the light traveling from the edge of the visible universe becomes distorted as a result of the shape of the universe. The first peak would indicate a positive, sphere-like, curvature if the first peak is left of the flat universe monopole point, and conversely, a negative, or saddle-shaped, curvature would be indicated by that peak being right of the flat point. It has been shown that the first peak position indicates that the demarcation point for a flat universe would be for $l \sim 200$, which the CMB spectrum upholds as the actual shape of the universe (see figure 1.5) [20]. Furthermore, the remaining portion of the universe, the part that has not been determined from the matter or dark energy densities, would make up the dark energy component of the universe (see equation 1.30).

1.1.4 Standard Cosmology

The Einsteinian general theory of relativity makes the assumption that all points in the universe have equivalence, a notion called the cosmological principle, essentially indicating that the

universe is generally homogeneous. The previously mentioned CMB as well as common experience indicates heterogeneity in the universe, but the principle holds true when considered on larger scales. Knowledge of relativity along with the CMB can help to further understand the makeup of the universe and dark matter.

Four-dimensional space-time motion is described by the Robertson-Walker metric [21]:

$$ds^2 = -dt^2 + a^2(t)\left[\frac{dr^2}{1-kr^2} + r^2\left(d\theta^2 + \sin^2\theta d\phi\right)\right] \tag{1.17}$$

where t, r, ϕ, and θ are co-moving four dimensional polar coordinates, which remain fixed for non-moving objects in an expanding universe, and the parameter k indicates the scalar curvature of three-dimensional space where $k = 0$, $k > 0$, or $k < 0$ correspond to a flat, closed, or open universe, respectively. The dimensionless scale factor of the universe $a(t)$ describes cosmological expansion. Normalizing at the present time t_0 by taking $a(t_0) = 0$, the radial distance is given by

$$R = a(t)\int_0^r \frac{dr}{\sqrt{1-kr^2}} \tag{1.18}$$

In the flat universe case, the object would be $\bar{R} = a(t)\bar{r}$, where $\bar{R}$ is the physical vector in 3-space and $\bar{r}$ is a co-moving vector. The velocity of the co-moving object would be its time derivative

$$\bar{V} = \frac{d\bar{R}}{dt} = \frac{\dot{a}}{a}\bar{R} + a\frac{d\bar{r}}{dt} \tag{1.19}$$

This equation becomes

$$\bar{V} = \frac{\dot{a}}{a}\bar{R} \equiv H(t)\bar{R} \tag{1.20}$$

assuming that the co-moving velocity $\bar{v} = a\dfrac{d\bar{r}}{dt} = 0$, where $H(t) \equiv \dfrac{\dot{a}(t)}{a(t)}$ is the Hubble parameter. Equation 1.20 states the Hubble Law, stating that velocities of objects moving away from each other are proportional to their distances.

The Einstein equations have their most general form [22]:

$$R_{\mu\nu} - \frac{1}{2}\mathcal{R}g_{\mu\nu} = 8\pi G T_{\mu\nu} + \Lambda g_{\mu\nu} \tag{1.21}$$

where $R_{\mu\nu}$ is the Ricci tensor, $\mathcal{R}$ is the Ricci scalar, $g_{\mu\nu} = diag(-1,\, a^2,\, a^2,\, a^2)$, G is the Newtonian gravitational constant, $T_{\mu\nu}$ is the stress-energy tensor for all fields present, and Λ is the cosmological constant.

Assuming an isotropic and homogeneous universe would imply that the energy-momentum tensor of the diagonal form $T^{\mu}_{\nu} = diag(-\rho,\, p,\, p,\, p)$, where ρ is the energy density of the universe and p the pressure, both of which have an assumed time-dependence, and with the conservation of energy indicating that $T_{\mu\ ;\nu}^{\ \nu} = 0$. The aforementioned assumptions result in the continuity equation

$$\frac{d\rho}{dt} = -3H(t)(\rho + p) \tag{1.22}$$

Then recalling that $H(t) \equiv \dfrac{\dot{a}(t)}{a(t)}$, multiplying each side by a factor of $4\pi a^2$, and rearranging the derivative, the previous equation could be rewritten as

$$d\left(\frac{4\pi}{3}a^3\rho\right) = -4\pi p a^2 da \tag{1.23}$$

Equation 1.23 indicates a co-moving sphere of radius a or proportionate thereto will have energy loss equal to the work done on its boundary by its expansion pressure. Solving the Einstein equation 1.21 for 0 and i components respectively give

$$\frac{\dot{a}}{a^2} + \frac{k}{a^2} - \frac{\Lambda}{3} = \frac{8\pi G}{3}\rho \tag{1.24}$$

and

$$2\frac{\ddot{a}}{a} + \frac{\dot{a}}{a^2} + \frac{k}{a^2} - \Lambda = -8\pi G\rho \tag{1.25}$$

which result in the Friedmann equation

$$H^2 \equiv \left(\frac{\dot{a(t)}}{a(t)}\right)^2 = \frac{8\pi G}{3}\rho - \frac{k}{a^2} + \frac{\Lambda}{3} \tag{1.26}$$

Assuming no cosmological constant and a flat universe, $k = 0$, removes the last two terms, and defines what is known as the critical density

$$\rho_c = \frac{3H_0^2}{8\pi G} \tag{1.27}$$

where $H_0 = \frac{\dot{a_0}}{a_0}$ and $a_0 = 1$ refers to the present Hubble rate. Taking the ratio of a given Hubble rate to the present one

$$\left(\frac{H}{H_0}\right)^2 = \frac{\rho_0}{\rho_c}\left(\frac{a_0}{a}\right)^3 + -\frac{k}{a_0^2 H_0^2}\left(\frac{a_0}{a}\right)^2 + \frac{\Lambda}{3H_0^2} \tag{1.28}$$

where ρ_0 is the present matter energy density. The above result is the basic ΛCMB cosmology equation:

$$\left(\frac{H}{H_0}\right)^2 = \Omega_m\left(\frac{a_0}{a}\right)^3 + \Omega_k\left(\frac{a_0}{a}\right)^2 + \Omega_\Lambda \tag{1.29}$$

where $\Omega_m = \frac{\rho_0}{\rho_c}$ defines the matter energy density, $\Omega_k = \frac{-k}{a_0^2 H_0^2}$ defines the curvature energy density, and $\Omega_\Lambda = \frac{\Lambda}{3H_0^2}$ defines the vacuum energy density.

Due to the fact that matter in the universe is split in some ratio of dark matter and baryonic matter, $\Omega_m = \Omega_B + \Omega_{DM} + \Omega_\nu$ for the baryonic, cold dark matter, and neutrino components respectively. To understand these values at the present time using equation 1.29 while allowing $a \to a_0$ and $H \to H_0$ it becomes

$$\Omega_m + \Omega_k + \Omega_\Lambda = 1 \tag{1.30}$$

in the present time. The best approximation of Ω_k has been determined to be near zero due to the flatness of space [23]. The Planck experiment, mentioned previously, measures anisotropies in the CMB and has found that $H_0 = 67.81 \pm 0.92 \frac{\text{km}}{\text{s Mpc}}$, as well as 69.2% of the energy density is in the

form of dark energy, 25.8% of the energy density is dark matter, and only about 4.8% of energy is in the form of baryonic matter [19]. Additionally, neutrinos contribute a small matter component as well, being distinct from the baryonic density (see section 1.2.2). Indeed, the vast majority of the composition of the universe remains currently unknown.

1.2 Dark Matter Candidates

The question of the existence of dark matter has shifted to hypothesizing regarding the nature of the substance as opposed to whether something exists in space; what could dark matter be? Myriad theories exist including various explanations within the Standard Model (SM) of particles such as dim dwarf stars or neutrinos, as well as new dark sector physics such as weakly interacting models or even particles with fractional charge. The list of possible dark matter candidates is too vast for inclusion here, however, some of the more historically or currently relevant candidates shall be discussed.

1.2.1 Baryonic Candidates

Explanations within the Standard Model had been formulated as some of the earliest contenders for dark matter, even being suggested in the 1937 paper by Zwicky [3]. Due to the fact that much of the noted missing mass of galaxies appeared to exist in galactic halos, one of the initial theories explained dark matter as MAssive Compact Halo Objects (MACHOs) taking the form of black holes, brown/white dwarfs, star remnants, Jupiter-Like Objects, or even large pockets of Hydrogen, all of which would appear generally non-luminous. However, experiments and astronomical surveys have largely excluded MACHOs and other baryonic candidates [24] [25]. Nonetheless, the MACHO Collaboration searching for MACHOs in the Milky Way galactic halo has estimated that about 20% of the galactic halo mass could be accounted for by these objects, specifically white dwarfs [24].

Furthermore, Big Bang Nucleosynthesis (BBN), the process when the universe started to form light nuclei from protons and neutrons, has indicated that dark matter consists of non-baryonic material[13]. Not long after the Big Bang, protons and neutrons formed out of the quark-gluon

plasma. The protons (p) and neutrons (n) along with electron neutrinos (ν_e) or anti-neutrinos ($\bar{\nu_e}$) and electrons (e) or positrons (e^+) freely decayed or combined, keeping the neutron to proton ratio close to one via

$$n + e^+ \leftrightarrow \bar{\nu_e} + p \tag{1.31}$$

$$n + \nu_e \leftrightarrow p + e \tag{1.32}$$

However, as the universe began to cool, the neutron to proton ratio reduced under equations 1.31 and 1.32 due to the slightly lighter mass of the proton than the neutron, until neutrinos decoupled, ceasing interactions with baryonic matter, at a time known as freeze-out. The era of freeze-out is known as such because as equation 1.32 indicates, the neutron to proton reactions required the existence of neutrinos, and neutrino decoupling largely fixed the ratios of neutrons to protons. The ratio of neutrons to protons continued to fall, but only due to neutron decay. Primordial abundances of light elements can be found in figure 1.6. Freeze-out became an important era because at that point deuterium could form, and then higher-order light elements until free neutrons became exhausted and electromagnetic forces prevented further nucleus fusion. Many of the free neutrons interacted with protons resulting in helium-4 and photons. The baryon to photon ratio η is the relative abundance of the baryons following BBN. A high η would indicate a shorter time for neutron decay and a longer overall time for light element formation and hence a greater overall light element, therefore baryon, quantity. However, a recent study has indicated that relic deuterium (D) to primordial ^{4}He and D + ^{3}He fractions would have required a longer time frame to develop and therefore would have indicated a non-baryonic nature to dark matter based upon the baryon to photon ratio [26]. Thus, it appears that a baryonic candidate for dark matter would be unlikely, however, the Standard Model could have non-baryonic candidates.

1.2.2 Neutrinos

Neutrinos, being weakly interacting and non-luminous and non-baryonic matter, were another logical explanation to the dark matter problem. Neutrinos become a stronger candidate taking into account the recently observed notion that neutrinos have mass due to observed neutrino flavor

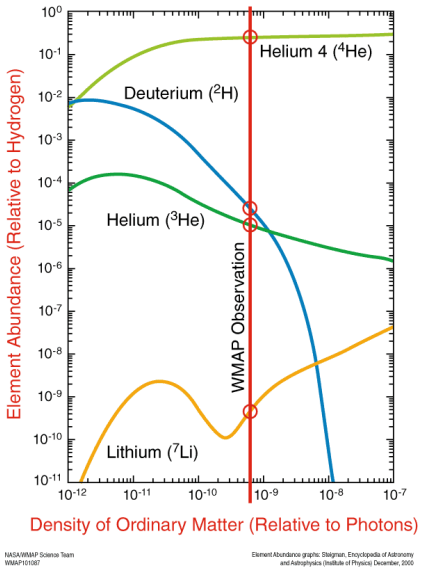

Figure 1.6: Element abundance relative to hydrogen vs density of matter relative to photons with WMAP Result. Image courtesy of NASA, reprinted from [27].

oscillation [28]. Current constraints on neutrino mass from ^{3}H beta decay and accelerator-based measurements are as follows [29]:

$$\begin{aligned} m_{\nu_e} &< 2.5 - 2.8 \text{ eV} \\ m_{\nu_\mu} &< 190 \text{ keV} \\ m_{\nu_\tau} &< 18.2 \text{ MeV} \end{aligned} \tag{1.33}$$

Theoretical constraints on neutrino mass indicate that the frequency of flavor has a dependence upon the mass difference of the two flavored neutrinos such that

$$\Delta m^2_{1\ 2} = m_2^2 + m_1^2 \tag{1.34}$$

Atmospheric cosmic ray collisions have been observed resulting in oscillations from muon neutrinos to tauon neutrinos. Also, solar neutrino observations have noted oscillations from electron

neutrinos to the other flavors; these observations have produced the following results [28] [30]:

$$\begin{aligned} \nu_\mu \rightarrow \nu_\tau \quad & \Delta m^2 \approx 2.4 \cdot 10^{-3} \text{ eV}^2 \\ \nu_e \rightarrow \nu_\mu,\ \nu_\tau \quad & \Delta m^2 \approx 7.6 \cdot 10^{-5} \text{ eV}^2 \end{aligned} \tag{1.35}$$

In the most extreme case, the difference in the neutrino masses between flavors would be such that the lighter of the two neutrino flavors would be zero. If the lightest neutrino is of zero mass this would imply the heaviest neutrino having mass $m_{heaviest\ \nu} = \sqrt{\Delta m^2_{\nu_\mu \rightarrow \nu_\tau}} = \sqrt{2.4 \cdot 10^{-3} \text{ eV}^2} = 0.05$ eV, considering significant figures. Inverting the mass hierarchy would instead give the result 0.10 eV. Combining this result derived from equation 1.35 and the results from equation 1.33, implies an overall upper bound on all neutrinos of $m_\nu < 2.5 - 2.8$ eV.

BBN implies that the relic abundance of all neutrinos is [31]

$$\Omega_\nu h^2 = \sum_{i=1}^{3} \frac{g_i m_i}{93\ eV} \tag{1.36}$$

given the case that all flavors had been in thermal equilibrium, where $g_i = 1$ in the case of a Majorana neutrino, $g_i = 2$ for the case of a Dirac neutrino, and $h \equiv \dfrac{H_0}{100\ \frac{\text{km}}{\text{s Mpc}}}$ is the present Hubble parameter. Thus, the result of equation 1.36 combined with results from Planck CMB give an overall neutrino energy density $0.0009 < \Omega_\nu < 0.048$ [32].

The non-zero value for Ω_ν indicates that neutrino contribution to the dark matter portion of the universe would be extremely small, and much smaller than the observed densities of dark matter. Furthermore, the relativistic nature of neutrinos indicates they would not be confined to the galactic halo, and even prior to that would have escaped the gravity wells responsible for large scale structure formation [14].

1.2.3 New Physics

There exists an old saying indicating that when all likely possibilities have been ruled out, whatever remains must be the answer, despite its unlikeliness. Such has been the historical development of the search for dark matter; having ruled out known contenders within the Standard

Model, theorists turned to new physics explanations to the dark matter problem.

1.2.3.1 Weakly Interacting Massive Particles

One of the most currently compelling explanations to the dark matter problem is what is known as the Weakly Interacting Massive Particle (WIMP), which does not interact electromagnetically with normal matter, but can interact gravitationally as well as kinematically through collisions with luminous matter [25]. Additionally, WIMPs satisfy what is known as a freeze-out requirement that the annihilation cross-section is such that the particle is stable and the abundance of the particle currently remains fixed, as shall be discussed.

Suppose that there exists a heretofore unknown fundamental particle in addition to known Standard Model particles which is stable. The thermal equilibrium number density n_χ^{eq} of this particle χ being

$$n_\chi^{eq} = \frac{g}{(2\pi)^3} \int f(p) d^3p \tag{1.37}$$

where $f(p)$ is the standard Fermi-Dirac or Bose-Einstein distribution and g is the number of internal degrees of freedom of the particle. When temperature T had been high in the universe such that it was much greater than the mass of χ, i.e. $T \gg m_\chi$, then n_χ^{eq} would be proportional to T^3 meaning that χ particles had abundance on par with photon abundance. Hence, the high temperature would mean that χ particles are constantly interacting with anti-χ particles to form Standard Model particle-antiparticle pairs and vice versa. However, as the universe cooled with T now measuring far below the mass of χ then

$$n_\chi^{eq} = g \left(\frac{m_\chi T}{2\pi} \right)^{3/2} e^{-m_\chi c^2/kT} \tag{1.38}$$

The number density of χ drops exponentially as the temperature falls as $e^{(-m_\chi c^2/kT)}$ under normal Boltzmann suppression. When T cools below m_χ then the annihilation rate becomes $n_\chi = \langle \sigma_A v \rangle H$, where σ_A is the thermally averaged annihilation cross-section into lighter particles, and v is the relative velocity. When $\frac{n_\chi}{\langle \sigma_A v \rangle}$ drops below the Hubble expansion parameter H the χ particles undergo freeze-out, also known as chemical decoupling, where there does not remain a sufficient number density for the particles to actually come close enough to interact, and at this

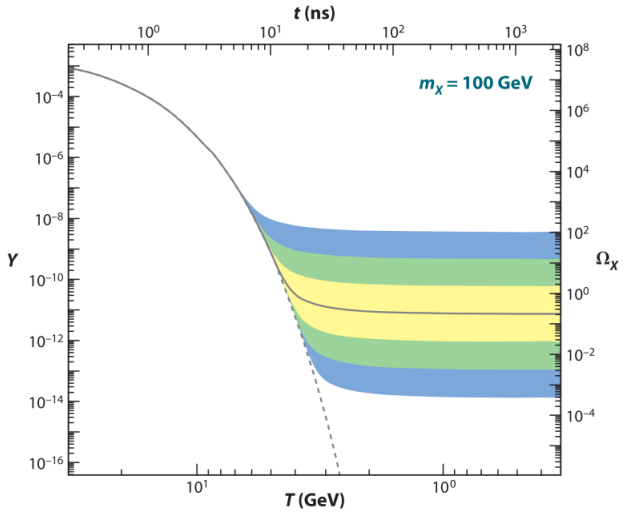

Figure 1.7: The figure shows the co-moving number density, represented here as $Y = n/s$, where s is the entropy, and n is the number density similar to equation 1.39. The number density indicates the relic density Ω_χ and is a function of Temperature T as it relates to cosmological time t. The case shown corresponds to a 100 GeV WIMP. The black line indicates the correct number density and associated time for WIMP freeze-out. The yellow, green, and blue regions indicate deviations from the number density by 1, 2, or 3 orders of magnitude, respectively. The dashed line indicates the case where the WIMPs never undergo freeze-out. Figure reprinted from [33].

point, χ number density becomes fixed at its relic density.

The Boltzmann equation for χ describes the process of χ number density time evolution $n_\chi(t)$

$$\frac{dn_\chi}{dt} = -\langle \sigma_A v \rangle \left[n_\chi^2 - \left(n_\chi^{eq} \right)^2 \right] - 3Hn_\chi \tag{1.39}$$

The squared terms in equation 1.39 come about as a result of both the χ into Standard Model particle-antiparticle interaction as well as the Standard Model into χ particle-antiparticle interaction. The solution to the Boltzmann equation becomes [33]

$$n_f \sim (m_\chi T_f)^{3/2} \, e^{-m_\chi/T_f} \sim \frac{T_f^2}{M_{Pl} \langle \sigma_A v \rangle} \tag{1.40}$$

where f denotes the freeze-out value and M_{Pl} refers to the Planck mass. Equation 1.40 occurs from

treating m_χ/T_f, which exists in the exponential, as constant, having a typical value of ~ 20 [33]. Figure 1.7 on the previous page shows the resulting number density as a function of freeze-out time; thus, predictions of the relic abundance can be determined resulting from differences in cross-section and freeze-out time. Equation 1.40 indicates that the thermal relic density of the χ particle does not have dependence upon the mass of the χ particle but does have inversely proportional dependence upon the annihilation cross-section σ_A. However, many theories indicate that $\langle \sigma_A v \rangle$ retains a mass dependence and have the resulting form when neglecting higher orders of v [33]

$$\sigma_A v = k \frac{g_{weak}^4}{16\pi^2 m_\chi^2} \cdot \left(1 + v^2\right) \tag{1.41}$$

where the first term in the expansion comes from S-wave annihilation and the second term comes from P-wave annihilation, referring to the orbital angular momentum of the initial state. The value $g_{weak} \approx 0.65$ is the weak interaction gauge coupling constant which becomes an essential part of the calculation, and k parameterizes deviations from the estimate. Allowing for a value of k between $\frac{1}{2}$ and 2, this would make a 100 GeV to 1 TeV WIMP have a relic density equal to that which has been determined from CMB measurements accounting for all of the dark matter in the universe. Figure 1.8 on the following page shows the relic density as a function of WIMP mass for a given k choice. This notion is referred to as the WIMP Miracle, because of the use of the weak interaction gauge coupling constant, and hence formulate χ as being weakly interacting particle of large mass.

1.2.3.2 Supersymmetry

Fortunately or unfortunately, the identity of the WIMP mass remains unknown. SUperSYmmetry (SUSY), a theory originally developed to solve problems dealing with hadrons within particle physics [34], indicates that every particle in the Standard Model has what is called a supersymmetric partner whose quantum numbers are the same as the Standard Model version with the exception of spin which differs by a half-integer, and the super-partner has a larger mass. Essentially there exists for each known fermion a corresponding boson, the theoretical partner being named with an

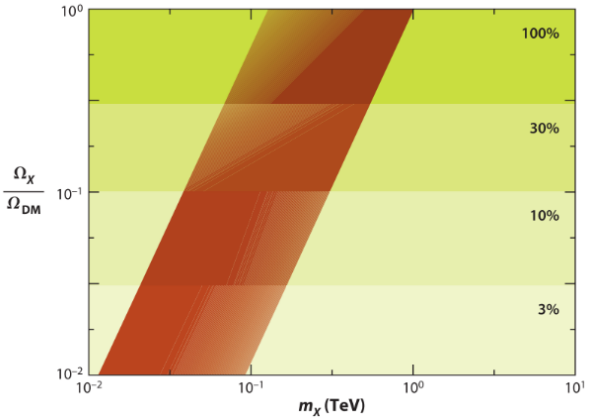

Figure 1.8: The figure shows a band indicating WIMP mass as it relates to the fraction of observed dark matter. The width of the band indicates the deviation of g from g_{weak} as defined in equation 1.41. Figure reprinted from [33].

's-' prefix, with the 's-' indicating that it is a scalar particle having zero spin, as well as a corresponding fermion for each known boson with its partner being named with an '-ino' suffix in some fashion. For example, the super-partner of the electron is called the selectron, and the super-partner of the Higgs boson is the higgsino. While supersymmetric theories make up a myriad of different theoretical possibilities, one of the most well developed and motivated WIMP candidates that remains is known as the Lightest Supersymmetric Particle (LSP), which comes from the Minimal Supersymmetric Standard Model (MSSM). From MSSM, good stable candidates for WIMP dark matter come in the form of some mixing of neutral half-spin fermions [31]. WIMP dark matter theories, of course, do not preclude the existence of charged super-partners with less stability which do not have notable relic abundance.

1.2.3.3 WIMP-less Miracle

Recall that in equation 1.40 the number density n_f for the χ particle had dependence as $\langle \sigma_A v \rangle$ and 1.41 where $\langle \sigma_A v \rangle \sim g_{weak}^4 / m_\chi^2$. The WIMP miracle came about because choosing $g_{weak} \sim 0.65$ would mean that there would be a relic density of χ consistent with Ω_{DM} for a massive WIMP. However, assuming that there existed other forces in the universe comprising a 'dark sector' of force, then particles such that the g_χ and the m_χ could exist as a myriad of different values while

maintaining the proper relic density for relic dark matter [35]. One motivated contender within the SUSY theory class is known as the Gauge-Mediated Supersymmetry Breaking (GMSB), and it is a good contender because it solves the new physics flavor problem. Simply put, the new physics flavor problem becomes an issue wherein some SUSY theories, flavor, baryon number, or lepton number might not remain conserved. GMSB includes fields with dynamically broken SUSY which mediates to MSSM through gauge interactions, including those with dark matter particles in additional sectors [33]. However, in GMSB models all Standard Model super-partners would decay into the gravitino, but dark matter becomes stabilized when there exists an additional $U(1)$ with charge conservation which implies massless gauge bosons in the hidden sector [33]. Additional $U(1)$ fermions could gain an additional fractional charge as discussed in section 1.2.4. Therefore, charged force carriers to the hidden sector can become a consequence of a WIMP-less SUSY as well.

1.2.3.4 Axions

Quantum ChromoDynamics (QCD) remains today as the foundational theory of the strong nuclear force, and it has a problem puzzling scientists to this day. The problem which plagues QCD comes by way of the inability of the theory to describe Charge-Parity (CP) violation, or rather, the lack thereof. C-symmetry means that the physics of corresponding particles and antiparticles should be the same, and P-symmetry states that the flipping of a spacial coordinate will not change the physics of the particle. Electro-weak theory has mechanisms for explaining CP violation observed in kaons, but strong force violating CP effect such as an electric dipole moment of the neutron has not been observed [36]. The quandary of CP violation in QCD is referred to as 'the strong CP problem'.

Concentrating only on the case with a single flavor quark, the gauge part of the QCD Lagrangian for mixing angle θ could be written as

$$\mathcal{L}_\theta = \theta g^2 \epsilon_{\mu\nu\rho\sigma} \frac{G_a^{\mu\nu} G_a^{\rho\sigma}}{32\pi^2} \tag{1.42}$$

where G refers to the gluon field strength and $\epsilon^{0\,1\,2\,3} = 1$, and g is the strong coupling constant. QCD will also have the mass term

$$\mathcal{L}_m = -\bar{\psi}\tilde{m}\psi \tag{1.43}$$

where $\tilde{m} = me^{i\gamma_5\phi}$ is called the fermion mass with chiral phase.

Both terms 1.42 and 1.43 conserve neither parity nor time reversal symmetry. The two aforementioned terms are related due to the triangle anomaly by chiral rotation so that $\psi \to \psi' = e^{i\alpha\gamma_5/2}\psi$ will result in $\phi \to \phi' = \phi + \alpha$ and $\theta \to \theta' = \theta - \alpha$ where $\bar{\theta} = \theta + \phi$. Note that $\bar{\theta}$ cannot change under the chiral rotation, therefore the parity-violating term G remains irremovable. Thus, $\mathcal{L}_\theta$ will retain θ dependence and therefore continue violating parity. As a consequence, as previously alluded, CP-violating observables would be expected, which would include electric dipole moment of the neutron d_e. Indeed, for a θ of ~ 1, the expected electric dipole moment would be of the order $\sim 10^{-16}$ e cm, however, current experimental constraints have excluded values of d_e greater than $2.9 \cdot 10^{-26}$ e cm [35].

A currently proposed theoretical solution to the strong CP problem becomes manifest through the introduction of a new pseudo-scalar field A with coupling

$$\mathcal{L}_A = -g^2\epsilon_{\mu\nu\rho\sigma}G_A^{\mu\nu}G_A^{\rho\sigma}\left(32\pi^2\right) \cdot \frac{A}{f_A} \tag{1.44}$$

where f_A is the new mass scale which is the decay constant of a new low mass particle, the axion. Thus, θ has been treated as a field requiring a new global symmetry which becomes spontaneously broken. The term f_A makes the $\mathcal{L}_A$ term dynamical, and the QCD effective potential $V\left(\bar{\theta}\right)$ depends on the $\dfrac{A}{f_A}$ coefficient. $V\left(\bar{\theta}\right)$ reaches a minimum when $\bar{\theta} = 0$, thereby solving the strong CP problem. Weak interactions create a small value for $\bar{\theta}$, but as a final result, the electric dipole moment of the neutron becomes very small and remains consistent with current experimental limits [33]. Interestingly, initially in the history of the axion, it had been thought that axion models would only have f_A of the order of weak-interaction, but it was later determined that f_A could have any value, ranging from the QCD scale to the Planck scale [37]. The same physical mechanism giving

rise to axions, that being the spontaneous breaking of $U(1)$ global symmetry at high energies, can also give rise to other theoretical particles called Axion Like Particles (ALPs) whose masses and couplings to photons remain independent parameters instead of being dependent upon f_A [38].

1.2.4 Lightly Ionizing Particles

The Lightly Ionizing Particle (LIP), also referred to in literature as a Fractionally Charged Particle (FCP), is a theoretical particle where the apparent charge of the particle q is reduced by a factor of the electron charge such that $q = f \cdot e$, where f is less than one, and e is the electron charge. LIPs would lose energy at a slower rate than a charge one minimally ionizing particle, such as a muon, proportional to f^2 [39]. Particles with a charge less than that of the electron are not foreign to the Standard Model, as quarks and anti-quarks are known as having $\pm\frac{1}{3}$ or $\pm\frac{2}{3}$ of an electron charge. However, the $\pm\frac{1}{3}$ or $\pm\frac{2}{3}$ charges are not known to exist unbound from a hadron due to strong interactions, forming particles that have charges that are integer multiples of e [40].

Note that the abelian theory of Quantum ElectroDynamics (QED) indicates that, theoretically, particles could have any electric charge because photons, carrying no charge, cannot directly couple to each other. However, the requirement that fields formed by the electromagnetic gauge group be commensurable and thus allow the gauge group to be compact means that charges must be integer multiples of some universal unit of charge [41]. Therefore, there must exist some yet undefined unit of charge e, which could be $\frac{1}{3}$ of the electron charge or it could be something much smaller, for which all other charges are an integer multiple.

There exist a variety of means by which the fabric of reality could include LIPs. Free states of quarks and new leptons with fractional charges are possible extensions to the Standard Model. The existence of magnetic monopoles could indicate new charged particles. Charge non-quantization could indicate small charges on neutrinos or charge differences in leptons [40]. These notions of sources of lightly charged particles shall be discussed in the following sections.

1.2.4.1 Additional $U(1)$ Groups

In the case of models containing more than one $U(1)$ group, $U(1)$ being the gauge group associated with electromagnetism, models can result in additional charged, or apparently charged particles. LIPs thus also come as a natural consequence in some string theories which have an additional $U(1)$. Theoretically, there could be a host of new $U(1)$ gauge groups with additional terms, as well. Normally, it would be thought that kinetic mixing of $U(1)$ symmetries are disallowed at the tree level within the framework of a Grand Unified Theory, however, radiative corrections can induce the effective charge because of kinetic mixing at the loop level.

Suppose there exists a gauge group containing two $U(1)$s which are $U(1)_A \times U(1)_B$, with gauge fields A_{A_μ} and A_{B_μ}, each with its own photon and its own electric charge. The Lagrangian would contain kinetic terms from the $U(1)$s that are given, in the most general case, by [42] [43]

$$-L^{kin}_{U(1)} = \frac{1}{4}F^{\mu\nu}_A F_{A\mu\nu} + \frac{1}{4}F^{\mu\nu}_B F_{B\mu\nu} + \frac{\chi}{2}F^{\mu\nu}_A F_{B\mu\nu} \tag{1.45}$$

where the first two terms are the kinetic energy of the $U(1)_A$ and $U(1)_B$ gauge fields, the last term in the equation represents kinetic mixing between the two types of photon, which can come about by radiative corrections, and χ is the mixing strength free parameter. $F_{\mu\nu}$ is the field tensor for the A and B fields, $F_{\mu\nu} = \partial_\mu A_\nu - \partial_\nu A_\mu$. Assume the case that there are fermions f_{AB} and f'_{AB} which have both A and B charge from both $U(1)$s, and with charge values (q_A, q_B) and $(q_A, -q_B)$. Furthermore, assume that there are two fermions f_A and f_B which have respective $U(1)_A$ and $U(1)_B$ charge only. Let the masses of the hypothetical fermions be such that $m'_{AB} > m_{AB} > m_A \approx m_B$. The Lagrangian from 1.45 will have the first two terms take χ_A and χ_B respectively, which are diagonal vacuum polarizations [43]. In the event that f_{AB} and f'_{AB} had unequal masses then the mixing of the respective photon types, shown in figure 1.9, would be non-zero [43] [44]. Specifically the kinetic mixing would be the additional term shown in equation 1.45, with χ given as

$$\chi = \frac{q_A q_B}{6\pi^2} \ln\left(\frac{M'_{AB}}{M_{AB}}\right) \tag{1.46}$$

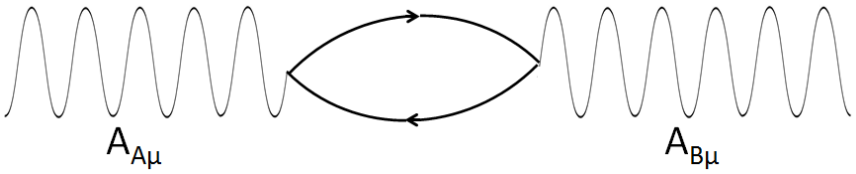

Figure 1.9: Two $U(1)$ groups have dynamical mixing fields mediated via virtual fermions which have charge under both $U(1)_A$ and $U(1)_B$. Figure reprinted from [40] based upon [44].

where M_{AB} and M'_{AB} are the respective masses of f_{AB} and f'_{AB} [43]. However, as long as fermions f_{AB} and f'_{AB} have masses larger than known fermions, there remains no restriction on their masses, which could even be of unification scale [45].

Now, define new gauge fields $A'_{A\mu}$ and $A'_{B\mu}$ in order to regain the diagonal kinetic terms under normalization. The new gauge fields have the following matrix represented relationship:

$$A'^{\mu} = D^{1/2} O^T A^{\mu} \tag{1.47}$$

where

$$\begin{pmatrix} \chi_A & \chi \\ \chi & \chi_B \end{pmatrix} = ODO^T$$

The fermions with charge under both groups, f_{AB} and f'_{AB}, can be integrated out leaving only f_A and f_B fermions with coupling to their corresponding $A_{A\mu}$ and $A_{B\mu}$. It can be shown, specifically from 1.47, that the two gauge fields are non-orthogonal combinations of the primed fields [43]. Thus, the f_A gauge field has a component associated with f_B and vice versa, with a shift such that

$$A_{B\mu} \to A'_{B\mu} + \chi A_{A\mu} \tag{1.48}$$

which gives the interaction between f_A and f_B. The coupling term from the B field results in coupling with the A gauge field, hence their interaction, where the A field is visible [46]. A result of the mixing is a non-zero coupling between the charged $U(1)_B$ fermions and the photon of

$U(1)_A$ amounting to an A type charge existing on the B type fermions. Hence, if type A is the SM electromagnetic charge, then there should be an apparent electromagnetic charge of ϵq_A on the B type photon given as [44] [46]

$$\epsilon = \frac{-\chi q'_B}{q'_A} \tag{1.49}$$

In the above equation, q'_B is the charge under field $A'_{B\mu}$ of f_B and q'_A represents the charge under field $A'_{A\mu}$ of f_A. If reality contained two massless $U(1)$ fields, then the orthonormal partner of the photon, which could be referred to as the paraphoton, would not couple to known Standard Model fermions. The paraphoton would couple to other fermions, and those fermions would couple to the Standard Model photon via either a new induced or altered coupling [43]. A paraphoton with large mass would result in an unbroken $U(1)$ such that there would not be coupling to the Standard Model photon [43]. The massless scenario has also been understood to be transferable to mirror dark matter theories and descriptions of the dark photon [47].

It follows that some dark matter models include a dark photon or paraphoton which could kinetically mix with the Standard Model photon to confer an effective small charge or even millicharge to particles in the dark sector [43]. The above equation results in the sought-after theoretical LIPs referred to throughout this work as having a charge of $f \cdot e$ where $f < 1$ and e is the electron charge. The notion that, resulting from an additional $U(1)$, particles in the hidden sector could receive an effective electric charge had been previously mentioned in section 1.2.3.3 for the case of a WIMP-less SUSY.

1.2.4.2 Monopoles

Maxwell's equations are known not to have a magnetic charge, however, the inclusion of a magnetic monopole would complete the symmetry of the electric and magnetic components of those equations. Dirac, while showing that monopoles were consistent with quantum electrodynamics, also showed that if monopoles did exist, they would constrain their charges under the following [48]:

$$eg = \frac{n\hbar c}{2} \tag{1.50}$$

with e being the electric charge, g the magnetic charge, n an integer relating the electric and magnetic charges, $\hbar$ the reduced Planck constant, and c the vacuum speed of light. Due to the existence of magnetic charge g, the relation derived by Dirac implies charge quantization for both electric and magnetic charges in the event that magnetic charge exists. In trying to find a unified gauge theory where strong force, weak force, and electromagnetic force gauge constants become unified at high temperatures, Polyakov and 't Hooft have shown that magnetic monopoles would be a natural consequence [45].

When monopoles become charged under the Witten Effect, the charge-parity violation remains a non-quantized parameter which would imply that the electric charge values could have any value. Thus, magnetic monopole theories become relevant to the notion of LIPs because monopole particles can have a non-zero electric charge under the Witten Effect caused by charge-parity violation [49].

1.2.4.3 Charge Quantization

Turning attention to the Minimal Standard Model (MSM), there has been much attention given to the question of whether or not charge quantization follows naturally from MSM [49] [50]. Consider a single generation of quarks and leptons and require constraints such that the Lagrangian must be $U(1)$ symmetric and that gauge anomalies are canceled; the constraints allow the theory to be renormalizable. The two previously mentioned constraints fix the hypercharges, allowing particles to have their standard values, and form the following relation between charge Q, hypercharge Y, and Isospin I_3:

$$Q = I_3 + \frac{Y}{2} \tag{1.51}$$

The above equation hinges on the notion that the electromagnetic group is such that there is $U(1)$ invariance left exact after electroweak symmetry breaking, making Q some linear combination of I_3 and Y. Therefore, particles have their standard quantized values under MSM. However, in consideration of the three generation MSM, charge quantization requires first finding all anomaly

free global $U(1)$ symmetries. The $U(1)$ symmetries are given by

$$L' = \alpha L_e + \beta L_\mu + \frac{L_\tau}{3} + \frac{-\alpha - \beta - (-\alpha^3 - \beta^3)^{\frac{1}{3}}}{3} B \tag{1.52}$$

where L_e, L_μ, and L_τ are the family lepton numbers. B is the baryon number, with α and β being free parameters. Assuming quantum gravity will then remove the mixed gauge-gravitational anomaly leading to L' characterized by three discrete sets

$$L' = \begin{cases} L_e - L_\tau = 0, \\ L_e - L_\mu = 0, \\ L_\mu - L_\tau = 0. \end{cases} \tag{1.53}$$

So, while using the extra imposition that the mixed gauge-gravitational anomaly cancels, electric charge may be dequantized through [51]

$$Q = I_3 + \frac{Y_{SM} + \epsilon L'}{2} = Q_{SM} + \frac{\epsilon L'}{2} \tag{1.54}$$

where $L' = L_i - L_j, (i, j = e, \mu, \tau; i \neq j)$, ϵ is an arbitrary parameter, and $Q_{SM} = I_3 + \frac{Y_{SM}}{2}$ is the SM electric charge. Thus, it occurs that there is charge dequantization in the three generation MSM but not in the single generation case, being at loggerheads with the notion of charge quantization implied by a compact gauge group. There exist a variety of ways to incorporate different models which could, however, extend charge quantization to the three generation case including extensions to the neutrino and lepton sector [50].

2. THE LARGE UNDERGROUND XENON DETECTOR

The Large Underground Xenon (LUX) detector is a retired gas-liquid dual-phase Time Projection Chamber (TPC) detector with a 370 kg (300 kg active) xenon volume, with a drift distance in the main volume of the detector of 48.32 ± 0.34 cm with a dodecagon face approximated as a circle of 23.65 ± 0.05 cm, which was 47.1 cm face to face when cold [52].

Although in general, dual-phase TPC physics applies to other noble element based detectors as well, xenon was used for the LUX detector because it is generally chemically and radioactively stable, and it can be easily scaled to larger detectors as is currently being done for the LUX-Zeplin (LZ) experiment [53]. Xenon has good properties as a scintillator, has a response such that one could discern electron recoils from nuclear recoils, and it has good electronegativity which prevents released electrons from recombining, as shall be discussed. Furthermore, xenon has the ability to self shield due to the high atomic number of xenon (Z=54), and because the liquid density of xenon is approximately 3 g/cm^3. The self-shielding ability of the liquid xenon allowed for fiducialization of the WIMP detector volume, where outlying background radiation would occur around the perimeter of the detector volume leaving the interior with a far reduced background. The detector made use of three-dimensional event tracking which could then be used to exclude such perimeter events.

LUX, functionally constructed as a WIMP detector, required a severely reduced background to ensure sensitivity. The detector was situated in the Davis Cavern of the Homestake Mine, at the 4,850 level, approximately one mile underground. After Homestake Mine stopped its gold production, the State of South Dakota modified parts of the mine for scientific use and re-branded it the Sanford Underground Research Facility (SURF). SURF is located in the town of Lead, South Dakota, in the heart of the Black Hills.

2.1 Detector Physics

The detector operates such that an incident particle makes a collision in the liquid region with either the xenon nucleus or surrounding electron, creating initial scintillation as well as ionization of the xenon atoms while casting off electrons. The scintillation and ionization occur in a two-pathed system of excited xenon and ionized xenon. The excited xenon atoms Xe^* combine with each other, forming an excited diatomic xenon molecule via $Xe^* + Xe \rightarrow Xe_2^*$ called an excimer or excited dimer. The resulting excimers form either a singlet or triplet spin state via $Xe_2^* \rightarrow 2Xe^* + \gamma$. The de-excitation of excimers occurs quite quickly, having respective 3 ns and 24 ns lifetimes for the singlet or triplet state. As excitation occurs, the xenon returns to ground state neutral pairs of xenon atoms while producing scintillation as a 178 nm photon.

The second path, which is called recombination, occurs as xenon ions combine with each other forming diatomic xenon ions with a plus one charge. These diatomic xenon atoms combine with some of the released electrons to become neutral excited diatomic xenon, of the character described in the first path, which returns to ground releasing additional 178 nm photons via

$$\begin{aligned} Xe^+ + Xe &\rightarrow Xe_2^+ \\ Xe_2^+ + e^- &\rightarrow Xe^{**} + Xe \\ Xe^{**} &\rightarrow Xe^* + \text{heat} \end{aligned} \tag{2.1}$$

The electrons released during ionization of the xenon which do not recombine move toward the liquid-gas interface via the guidance of an electric field, where the electrons are extracted by the electric field causing additional creation of light from fluorescence which is the ionization signal. Thus, the electric field in the bulk suppresses recombination, and only electrons that do not recombine contribute to the ionization signal. In instances without an electric field in the bulk, scintillation from the excitation of excitons produced from recombination would dominate the prompt scintillation signal. Some collision energy becomes lost to heat, with a greater proportion lost in a nuclear recoil than in an electron recoil.

Furthermore, there can be the case where two excitons could interact, partially de-exciting by emitting an ionization electron as $Xe^* + Xe^* \rightarrow Xe + Xe^+ + e^-$ in a process known as biexcitonic or Penning quenching [54]. The electron that results from biexcitonic quenching can either undergo recombination or extraction like the other electrons mentioned above. As above, the extracted electron will contribute to the ionization signal, whereas the recombined electron would produce a photon. Thus, the result would be that two excitons would produce an exciton and a photon, or a photon and an electron [55]. It is important to note that in either case, the number of observed scintillation photons reduces because two excitons resolve to produce either one photon or none at all.

Prompt scintillation, whether from initial excitation of xenon atoms, or resulting from recombination, is referred to as the S1 signal, whereas the secondary fluorescence from electrons extracted from the liquid is referred to as the S2 signal. The timing between the S1 and S2 signals allows for the measurement of the drift time of the electrons, as shown in the cartoon in figure 2.1. Knowledge of the drift time per centimeter of the liquid at a given electric field, as well as the x-y positions of the signals, recorded using Photo-Multiplier Tubes (PMTs, see section 2.2.1 on page 40) allow for reconstruction of the three-dimensional position of the event with 1 mm precision in the z dimension and 4 to 6 mm in the x and y dimensions [55].

Xenon atoms, having a large atomic size, will often become polarized by and exert an attractive force on excess electrons in the media. The gas-liquid boundary acts as a dielectric boundary with constant potential, due to greater polarization attraction in the liquid than the gas. An electron drifting toward the boundary encounters a potential barrier, known as the Schottky barrier, as a result of the image charge of the electron, which has the equation [56]

$$\phi_b = \frac{e^2}{8\pi\epsilon_0 z}\frac{\epsilon - 1}{\epsilon + 1} \tag{2.2}$$

where e is the electron charge, ϵ_0 the dielectric constant of vacuum, ϵ the dielectric constant of the material, and z is a characteristic dimension of the order of the lattice constant. Assuming liquid

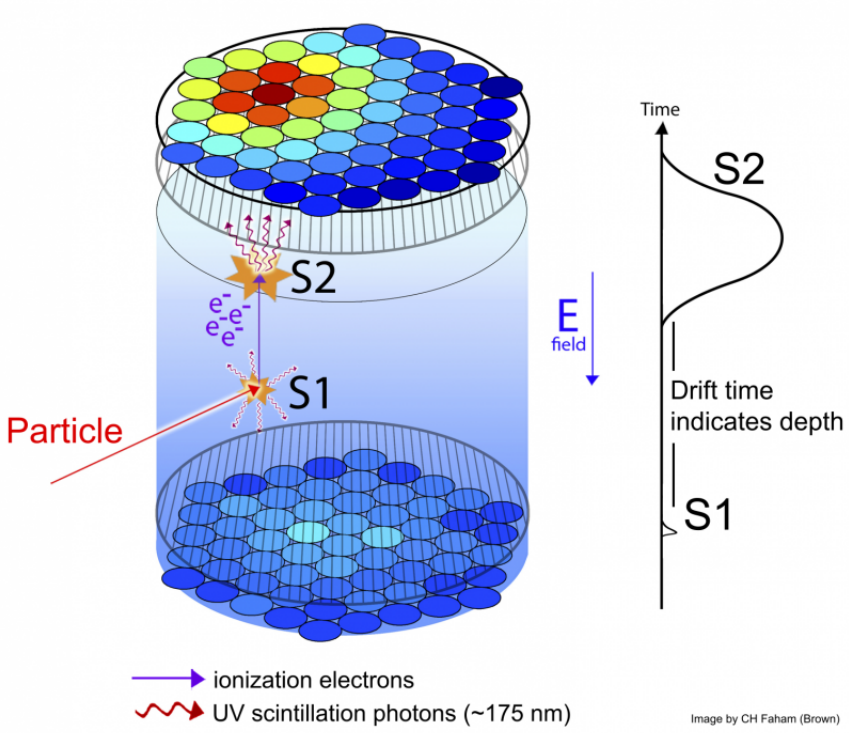

Figure 2.1: Drawing showing the propagation of light and charge in the LUX detector. Image reprinted from [18].

xenon atoms tend to arrange in a simple cubic lattice then $z \sim 4 \cdot 10^{-10}$ m [57]. In the absence of an electric field, the barrier at the liquid-gas boundary amounts to $\sim 0.6 - 0.85$ eV [58]. Whereas, the thermal energy of electrons is ~ 0.015 eV at liquid xenon temperatures, which is far below the boundary and thus too low to allow for many thermal electron emissions [58]. The electric field E results in the force that drifts the electrons from the interaction site to the gas-liquid interface, which would cause $\phi = eEz$. The Schottky Effect, where an electric field causes an applied force on the electrons which heats them and effectively lowers the height of the Schottky barrier by [56]

$$\Delta\phi_b = e\left(\frac{eE}{4\pi\epsilon_0 z}\frac{\epsilon-1}{\epsilon+1}\right)^{1/2} \tag{2.3}$$

Thus, it follows that the greater the electric field near the gas-liquid interface, the less energy would be required for electron extraction. When electrons in the liquid xenon have sufficient

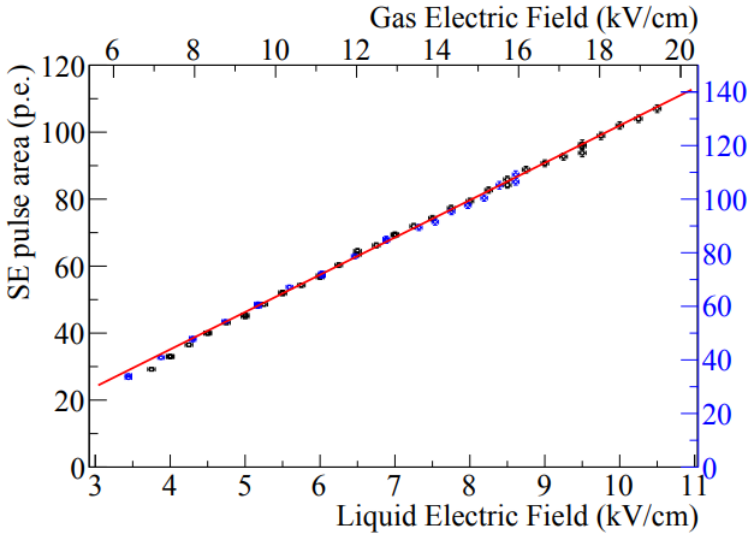

Figure 2.2: This figure shows the Single Electron (SE) pulse area size as a function of the applied electric field in the liquid xenon (shown as bottom scale) and in the gas (shown as top scale). This figure shows data reprinted from Lawrence Livermore National Laboratory (LLNL) [58] for both the high field (black squares and left axis) and low field (blue circles and right axis) measurements. These data show that there exists a linear relationship between SE pulse area and the applied electric field.

momentum greater than that needed to overcome the barrier they become extracted from the liquid xenon, where they encounter a higher electric field in the gas and produce additional scintillation as they collide with other xenon atoms. Liquid xenon has a dielectric constant of about 1.96, whereas gaseous xenon has a dielectric constant of approximately 1, meaning that at the gas-liquid interface the gas will have an electric field of nearly twice that of the liquid [59]. The amount of scintillation from an extracted electron increases with a linear relationship to the electric field as shown in figure 2.2 [58]. Additionally, single electron scintillation has some dependence due to detector pressure as well [56]. Assuming no changes in detector pressure or electric fields then the single electron pulse area should remain constant and be predictable following calibration. For more information on calibrations see section 2.3 on page 52.

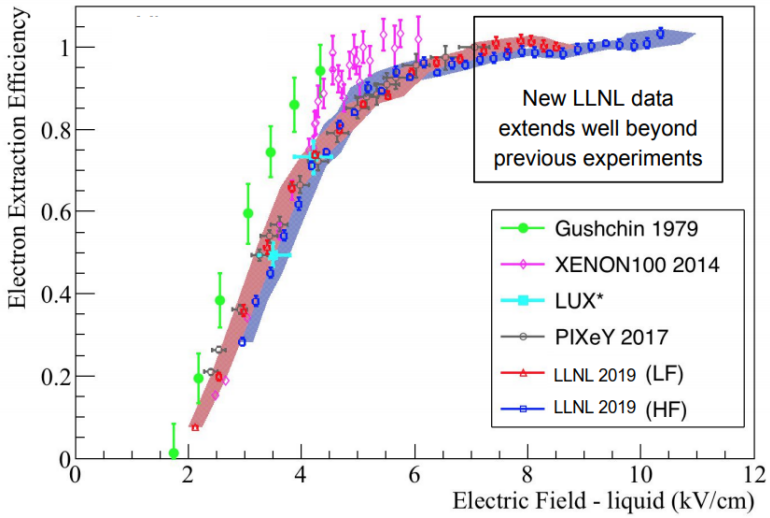

Figure 2.3: This figure shows gas-liquid TPC measurements of electron extraction efficiency as a function of electric field for the Xenon100, LUX, and PIXeY experiments, as well as the 1979 measurements of Gushchin (see [56]) and the new high field (HF) and low field (LF) measurements of LLNL. The LLNL measurements indicate efficiency saturation in the range 7.5-10.4 kV/cm. Figure reprinted from [58].

The electron extraction efficiency is defined as [56]

$$\kappa = \frac{\int_{\phi_b - \Delta\phi_b}^{\infty} \sqrt{\varepsilon} f\left(\varepsilon\right) d\varepsilon}{\int_{0}^{\infty} \sqrt{\varepsilon} f\left(\varepsilon\right) d\varepsilon} \tag{2.4}$$

with $f\left(\varepsilon\right)$ being the energy distribution of electrons, with the electrons having energy ε. Also note that the electron energy itself depends upon the electric field, thus $\varepsilon = \varepsilon\left(E\right)$. The $\sqrt{\varepsilon}$ term in the above equation has its form due to the fact that it only selects electrons with velocities towards the gas-liquid interface. The extraction efficiency, given in equation 2.4, represents the probability of electrons to successfully become extracted from the liquid. Electrons which fail to overcome the barrier will reflect back into the liquid, but can undergo several attempts over the course of a nanosecond to pass the barrier, having an overall probability of extraction of $\kappa_n = 1 - \left(1 - \kappa\right)^n$ for the nth attempt. Recent measurements have indicated electron extraction efficiency saturation in the range 7.5 - 10.4 kV/cm, and that saturation had nearly been achieved in previous dual-phase TPC experiments (see figure 2.3) [58].

Following a recoil, electrons liberated from the interaction site drift to the gas-liquid interface of the detector. The maximum drift time recorded in LUX was 324 μs with an averaged measured electron drift speed of 1.51 $\pm$ 0.01 mm/μs [52]. The Run03 WIMP search measured an electron extraction efficiency of 49 $\pm$ 3% [60]. Electrons extracted from the liquid which produce the S2 signal have the following relation to photon quantity [13] [61]:

$$\frac{n_{ph,SE}}{d} = \left(0.140\ \frac{E_{gas}}{N \cdot 10^{-17}} - 0.474\right) N \cdot 10^{-17} \tag{2.5}$$

where the mean number of photons produced by a single electron extracted from the liquid is $n_{ph,SE}$, E_{gas} is the electric field in the gas region with units of V/cm, N is the number density of the xenon gas in atoms/cm^3, and d is the length of the gas gap in cm. The gas gap in LUX, also known as the S2 region, defines the distance that the electrons will travel, and in LUX this would be the distance between the gate grid and the anode $d = 0.5$ cm. For LUX in Run03 $E_{gas} = 6$ kV/cm, $N = 6.9 \cdot 10^{19}$ atoms/cm^3, which resulted in an S2 yield of 256 photons per extracted electron [62]. Taking into account that the light collection efficiency for S2 signals was 9% [62], the resulting anticipated SE size should be approximately 23 photoelectrons detected (phd)[1] per extracted electron, which accords well with the 23.77 $\pm$ 0.01 phd SE size noted at the end of LUX Run03 [13].

2.1.1 Energy Reconstruction

Energy reconstruction in dual-phase TPC detectors comes from the quantization of photons and electrons represented by the S1 and S2 signals, which in turn are representative of the number of excitons Xe_2^* and the number of electron-ion pairs, respectively [63]. Calibration of the detector occurs via the measurement of known sources with known energies. The energy E has the reconstruction equation

$$E = \frac{W}{L}\left(n_{ex} + n_i\right) \tag{2.6}$$

[1]Sometimes the abbreviation phe is used for photoelectrons as opposed to phd, and at times the two are used interchangeably. However, the number of photoelectrons emitted might not be equivalent to those detected due to previously mentioned Penning quenching. The standard has moved to using phd.

where n_{ex} is the number of excitons and n_i is the number of electron-ion pairs. W is the work function, that is the average energy needed to produce a single excited or ionized atom, which is known to be $W = 13.7 \pm 0.2$ eV [64]. L is known as the Lindhard factor, which for electron recoil interactions is one, but for nuclear recoil interactions varies relative to the energy of the interaction. The Lindhard factor accounts for the greater amount of heat that becomes lost in a nuclear recoil and is in a sense built into the work function due to the fact that electron recoils have a known ratio of excitons to ions which has been experimentally determined as $\frac{n_{ex}}{n_i} = 0.2$ [65].

Measured quantities of photons from initial or recombination excitons n_γ can be expressed as

$$n_\gamma = n_{ex} + r \cdot n_i \tag{2.7}$$

with r being the fraction of the initial electron-ion pairs which undergo recombination to form additional excitons expressed as

$$r = 1 - \frac{n_e}{n_i} \tag{2.8}$$

Thus, the number of non-recombined electrons can be expressed as $n_e = (1 - r) \cdot n_i$.

Values for n_γ and n_e correlate directly to initial detected scintillation and ionization, which are the S1 and S2 signals in the detector. The value for the energy reconstructed can be rewritten as

$$E = W\left(n_\gamma + n_e\right) \tag{2.9}$$

In terms of S1 and S2 detected photons, which are the associated primary and secondary pulse signal, the equation becomes

$$E = W\left(\frac{S1}{g_1} + \frac{S2}{g_2}\right) \tag{2.10}$$

with g_1 and g_2 being the gains for the S1 and S2 pulse areas, and have units of phd/quantum; g_1 being representative of the prompt scintillation light detection efficiency, which also accounts for PMT quantum efficiency, and g_2 dependent upon the electron extraction efficiency at the gas-liquid interface. Technically, the above equation remains true for an electron recoil. The equation

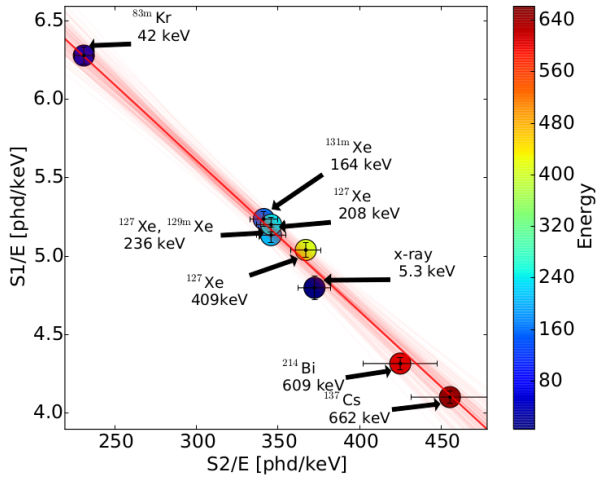

Figure 2.4: The Doke plot used to calculate values of g_1 and g_2. Figure reprinted from [13].

for nuclear recoil energy E_{nr} becomes modified as $E_{nr} = \frac{E_{er}}{L}$, which takes into account the appropriate Lindhard factor, with the electron recoil energy E_{er} given as in equation 2.10.

The Lindhard model effectively accounts for the additional processes known as Penning effects which occur in nuclear recoils, whereby two xenon molecular excitons could collide and de-excite while emitting less than two photons. Penning effects can occur by way of releasing one photon with additional heat loss known as Penning or biexcitonic quenching, or a photon and an electron-ion pair known as Penning ionization which is described earlier in section 2.1. From the outset, it is unknown whether an interaction is a nuclear recoil or an electron recoil, but knowledge of the Lindhard factor allows for the calculation of either energy scenario, either electron recoil or nuclear recoil, with units represented as keV$_{ee}$ or keV$_{nr}$ for their respective energies.

Knowledge of the mean energy of several calibration sources, and specifically, knowledge of the S1 and S2 responses of those sources allows for the calculation of g_1 and g_2 at any state of the detector. Similarly, using the same sources of known energy at different drift field settings can allow for the calculation of g_1 and g_2 as well. Such sources with known responses can be fitted on a line of $S1/E$ vs $S2/E$ in order to determine the gains with a fit for the slope = $-g_1/g_2$ and y-intercept = g_1/W [13]. The relative positioning of the points in this $S1/E$ vs $S2/E$ space indicate the relative amount of recombination occurring at a particular energy, where events that have

more recombination will see a greater contribution to S1 than S2 (see figure 2.4). The graphing and fitting of the slope of $S1/E$ vs $S2/E$ is known as a Doke plot, and for the final analysis of Run03 data, the gain factors were determined to have $g_1 = 0.117 \pm 0.003$ phd/photon and $g_2 = 12.1 \pm 0.8$ phd/liquid electron which indicated an overall electron efficiency of 49% for Run03 [66]. Energy calculations presented in the main analysis section of this work solely incorporate the Run03 values for g_1 and g_2. For Run04, the variable electric fields meant that there needed to be four separate time bins over the course of the run, with g_1 decreasing from 0.100 ± 0.002 to 0.097 ± 0.001 phd/photon and g_2 increasing from 18.92 ± 0.82 to 19.72 ± 2.39 phd/liquid electron with an overall electron extraction efficiency of $73\% \pm 4\%$ [66]. Another method used to resolve total S2 energy makes use of the bottom PMT array only, the rationale being that the top array can be subject to PMT saturation with high energy events. Thus, $g_{2,\,bottom} = 7.2$ calculated from the bottom PMT array could be considered an alternative method of determining the total S2 energy of the event [67]. Therefore, LUX employed several calibration sources in order to determine g_1 and g_2 and modify them as needed at various times of detector operation (see section 2.3 on page 52).

2.2 Detector Components

The following section details various components of the LUX detector including components relevant to the internal cryostat as well as external circulation and backup systems. An overview of the internal structure of the cryostat can be seen in figure 2.5 and include the photo-multiplier tubes, grids, and thermosyphons. External components include the getter purification system, the xenon storage and recovery vessel, the recovery balloon, and the data acquisition system.

2.2.1 Photo-Multiplier Tubes

Two hexagonal arrays of 61 Hamamatsu R8778 4.5 cm diameter Photo-Multiplier Tubes (PMTs) each at the top and bottom of the detector record the prompt light and charge signals (see figure 2.6) [68]. The tightly packed PMTs overlapped the sides of the detector in order to maximize light collection. The PMTs in LUX had total efficiency of 30%, having 33% quantum efficiency dictated by photon-photoelectron conversion, and with 90% photoelectron to signal retention efficiency [68].

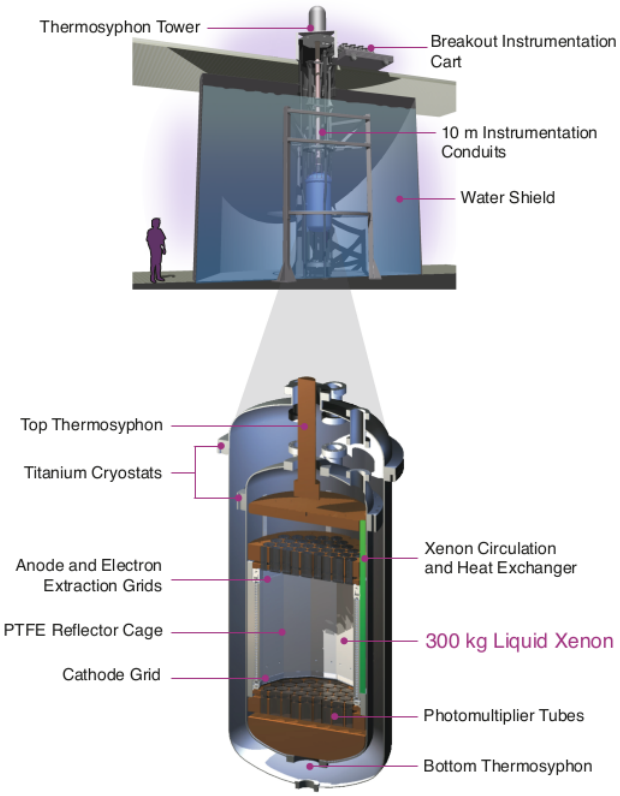

Figure 2.5: The LUX detector was a 370 kg liquid xenon time projection chamber designed to search for WIMP dark matter. 300 kg of the liquid xenon remained in the active region. It had two arrays of 61 PMTs, one at the top and one at the bottom of the detector. The top image shows the detector situated in the water shield compared to the height of a person, along with the thermosyphon tower and electronic instrumentation cart. The bottom image shows the inner cryostat, heat exchangers, drift and extraction grids, and the PMT arrays. Figure reprinted from [18].

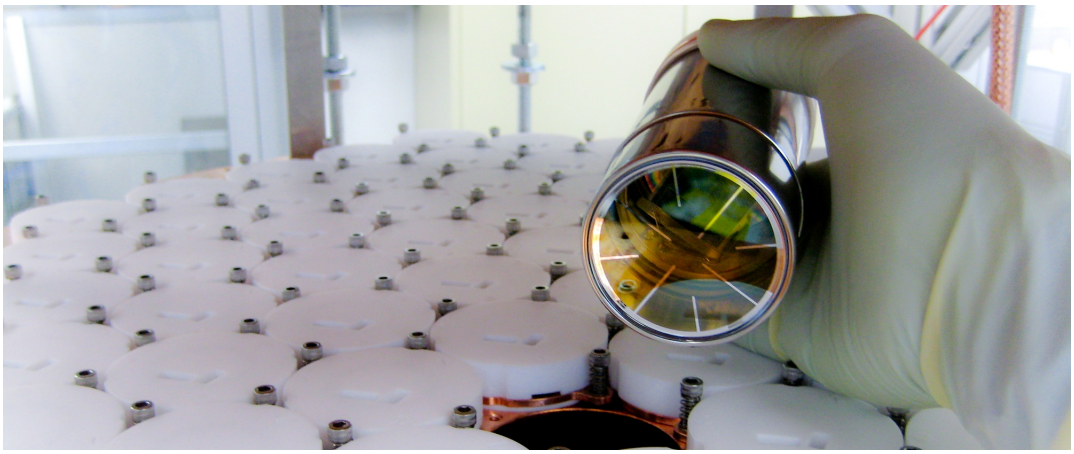

Figure 2.6: LUX used two hexagonal arrays of 61 Hamamatsu R8778 4.5 cm diameter Photo-Multiplier Tubes (PMTs). PMTs in LUX had total efficiency of 30% at 175 nm. Figure reprinted from [18].

Figure 2.7: This photograph shows PMTs being installed into the top array in LUX. Note that the area between the PMTs is filled by a PTFE surface. Figure reprinted from [18].

The PMTs had a spectral range of 160 to 650 nm with a maximum sensitivity at 420 nm [59]. The Hamamatsu R8778 had been designed for use at liquid xenon temperatures ranging from 165 to 180 K, and their behavior in liquid xenon had been well documented prior to their deployment in LUX [68]. Each PMT received individual calibration to determine the operating voltage and dark count of the PMT. Each tube had been biased to achieve an average gain of $5.08 \cdot 10^6$ with an average bias of -1216 V needed to achieve that gain [60]. Radio-pure materials were used in the creation of detector components, and every material used was assayed, with a radiation budget allotted to the entire experiment (see section 2.4 on page 59). Although a crucial element of the detector, the PMTs used a large portion of the radiation budget, and had measured radioactivity of 9.8 ± 0.7 mBq/PMT and 2.3 ± 0.5 mBq/PMT for ^{238}U and ^{232}Th respectively [69]. The PMT arrays themselves were constructed of oxygen-free high conductivity copper, with an outer face of the arrays being made of reflective PolyTetraFluoroEthylene (PTFE), also known colloquially as Teflon. See figure 2.7 for a picture of the top PMT array.

Both above the top PMT array and below the bottom PMT array resided a 5 cm thick circular copper plate with a diameter of 55 cm [13]. Both copper plates served dual functions of radiation shielding and temperature regulation, with the top plate helping to maintain the xenon at the top of

the detector as a gas, and the bottom plate, known as the Filler Chiller Shield, helping to equalize the temperature of newly filtered liquid xenon with the temperature of the liquid bulk. Detector walls constructed from PTFE, chosen for its high light reflectivity in liquid xenon at 178 nm, allowed for maximum light collection [70]. Indeed, because of PTFE, LUX had an optical rate of reflectivity at 178 nm in liquid xenon consistent with 100% at the 1σ level [69] [71]. Care was taken to assure that gaps or voids would be filled with copper or PTFE in order to prevent light loss and minimize the amount of xenon that would not be in the fiducial volume of the detector. Titanium struts suspended various detector components in their required locations.

2.2.2 Xenon Circulation

In order to maintain the high purity of the xenon from either inner detector materials and cables outgassing or non-noble element contamination, constant circulation of the xenon was necessary. Xenon first needed to be returned to its gaseous state before being piped over to the SAES Mono-Torr getter (PS4-MT15-R-1) [59]. The getter assured that circulating gas had non-noble impurities reduced to less than one part per billion [59]. Liquid xenon traveled from the weir reservoir, which set the liquid level in the detector as halfway between the gate and anode electric grids, through a series of two heat exchangers. The first of the heat exchangers vaporized the liquid, heating the xenon leaving the detector with xenon returning to the detector after purification, and liquefying the incoming xenon in the process. Now a cold gas, the outgoing xenon passed through concentric piping where the outgoing gas cooled incoming warm xenon. Upon return of the purified xenon, the material would pass through the previously mentioned heat exchangers, finally being equilibrated with the liquid xenon bulk by the aforementioned Filler Chiller Shield [67].

Very cold stable temperatures, which were managed through the use of four thermosyphon cold heads, maintained the liquid xenon inside LUX to within one degree Kelvin of 180 K for the main dark matter runs [13]. One of the cold heads was attached to the top upper radiation shield over the top PMT array; one attached to below the Filler Chiller Shield which, in turn, was below the bottom PMT array. Located along the middle of the length of the TPC, the two other thermosyphons had been mounted to a thin copper sheet which wrapped around the inner cryostat,

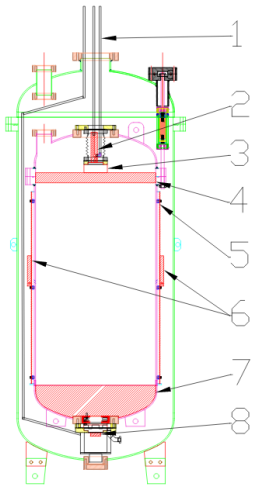

Figure 2.8: This figure depicts thermosyphon couplings of the LUX detector. Labels: 1. nitrogen gas inlets, 2. thermosyphon evaporator head TS1, 3. coupling between upper copper radiation shield and TS1, 4. upper copper radiation shield, 5. cylindrical copper thermal shield mounted outside the inner cryostat, 6. thermosyphon evaporator heads TS2 and TS3 attached to the cylindrical copper thermal shield, 7. Filler Chiller Shield, 8. thermosyphon evaporator head TS4 coupled to the Filler Chiller Shield. Figure reprinted from [59].

and these thermosyphons maintained the cold temperature of the outer perimeter. In truth, there existed a fifth thermosyphon which did not cool the TPC but instead resided within the vacuum space between the inner and outer cryostat and served as a charcoal trap.

The thermosyphons consisted of a series of loops filled with gaseous nitrogen in thermal contact with the inner cryostat (see figure 2.8). Liquid nitrogen was added to the top portion of the thermosyphons, referred to as the condenser, which would cool the nitrogen gas, causing it to condense into the bottom of the loop where the now liquid nitrogen in the thermosyphon would cool the inner cryostat. Upon warming, the liquid nitrogen inside the thermosyphons would vaporize and return to the top of the condenser to start the cycle anew. Each thermosyphon could cool with a power of 200 - 400 W. Detector operators had the ability to fine-tune the temperature, adding heat if needed, through the use of two cold heads with 50 W heaters. Additional 750 W heaters were attached to the Filler Chiller Shield and the upper copper radiation shield, which provided extra heat when needed, such as when removing xenon at the end of the science run.

The xenon circulated by means of a twin-headed KNF double-diaphragm pump (PM-23480-

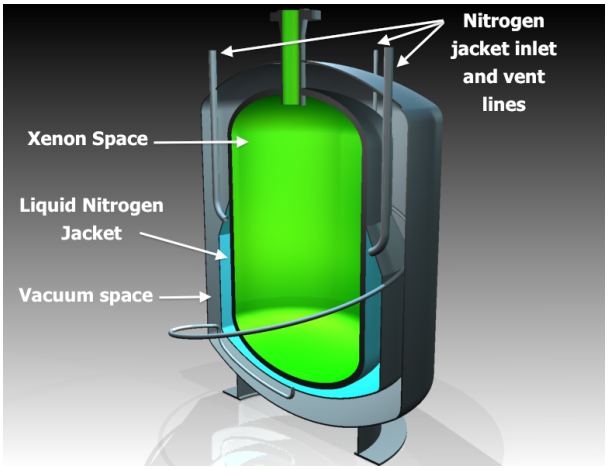

Figure 2.9: This figure depicts a cross-section of the Storage and Recovery Vessel (SRV), showing the nitrogen and vacuum layers surrounding the xenon space. Figure reprinted from [59].

150-3-1.2) [13]. Two high-rate mass flow controllers (Brooks SLA6951) assured a flow rate of approximately 25 standard liters per minute, which meant that approximately 200 kg, about two-thirds of the xenon in LUX, proceeded through circulation and purification per day [13]. Additional mass flow controllers were used to ensure a movement of xenon near cables where outgassing occurred, in order to ensure that outgassed impurities were removed. The LUX pipe system also contained flow paths for the xenon from which to sample measurements of detector impurities at various areas along the xenon flow path. Also, there existed routes along the length xenon piping through which various calibration sources could be added. When sampling, the residual gas analyzer detected impurities by measuring the partial pressures of oxygen, nitrogen, argon, and krypton, which then compared their levels to xenon sampled from a source with known impurity levels.

2.2.3 Xenon Storage and Recovery

For storing or removing excess xenon from the experiment, a compressor was used to direct the xenon to a series of bottles piped into the system. For emergency recovery of xenon, lest the precious resource become lost to atmosphere, LUX developed two means of recovery: the Storage and Recovery Vessel (SRV), and a xenon inflatable vessel.

The SRV was a multi-layered pressurized cryogenic container capable of storing up to 400 kg of xenon. The inner layer of the SRV stored the xenon, and the outermost layer was a vacuum; the SRV had a nitrogen jacket layer on its bottom half, between the xenon and vacuum layers, which served as its cooling source (see figure 2.9). The positioning of the layers, with the nitrogen and xenon layers protected from ambient temperatures, reduced overall heat loss and helped keep the SRV at temperatures cold enough to freeze incoming xenon. Various pressure releases were incorporated in order to release pressure from the nitrogen as it heated and vaporized. The SRV had a maximum allowable working pressure of 1190 psig at 100 °F [59].

Xenon recovery was triggered by an instrument known as the Automated Controlled Recovery System (ACRS). Before starting a recovery, the ACRS would ensure that conditions inside the SRV remained suitable for xenon recovery. At the normal operating pressure of the SRV it would have lower pressure than the operating pressure of the main detector, ensuring that the flow of xenon would be towards the SRV. The ACRS would recover xenon to the SRV in the event that there remained insufficient liquid nitrogen to keep the detector cold, triggering at the point where it had only enough nitrogen to perform the recovery. Furthermore, the ACRS would recover xenon in the event of a sustained power outage, if communication with the main computer or backup had ceased for more than 48 hours[2], or if over-pressure had been detected.

Finally, in the unlikely event that there had been a disaster such that the ACRS and SRV could not prevent loss of xenon, installed burst disks venting to a Seaman 8130 XR-5 polyester geomembrane inflatable vessel, measuring approximately 10 ft by 10 ft by 26 ft and colloquially referred to as 'the balloon', had the capacity to hold all of the xenon in LUX at room temperature (see figure 2.10) [59]. Through both the SRV and the balloon, in the event of an emergency, the precious xenon detector material would not become lost and released to the atmosphere.

2.2.4 Grids

The LUX detector made use of five high voltage grids throughout the length of the detector. The upper portion of the detector as labeled in the 'top grids' section of figure 2.13 were, in descending

[2]Which almost occurred following a computer failure on 24 December 2014.

Figure 2.10: This photograph shows a test of the recovery balloon underground. The 70 m^3 volume balloon could hold 370 kg of xenon at standard temperature and pressure which would inflate the balloon to 95% of its capacity. Photograph reprinted from [18].

order, the top PMT shield, the anode, and the gate grid. The 'bottom grids' section consisted of the cathode grid located above the bottom PMT shield grid. The two PMT shields were usually just referred to as the 'top' and 'bottom' grids respectively. Like the detector itself, the grids in LUX had a dodecagonal form. The grids had different consistently applied voltages for each detector run; LUX used the following voltages for Run03: top -1 kV, anode +3.5 kV, gate -1.5 kV, cathode -10 kV, and bottom -2 kV [59]. The grids had a cold separating distance between them of 3.8 cm, 1 cm, 47.1 cm, 4 cm, respectively (see figure 2.11) [18]. The liquid level remained 0.5 cm from both the anode and gate grids throughout the duration of the experiment. The top and bottom grids were situated 1 cm from their corresponding PMT arrays.

The anode grid had a unique form compared to the others, being made of a mesh as opposed to wire planes. The mesh of the anode had 0.025 cm wire spacing with wires constructed of 316 stainless steel of diameter 0.003048 cm [59]. In constructing the anode, the mesh was placed

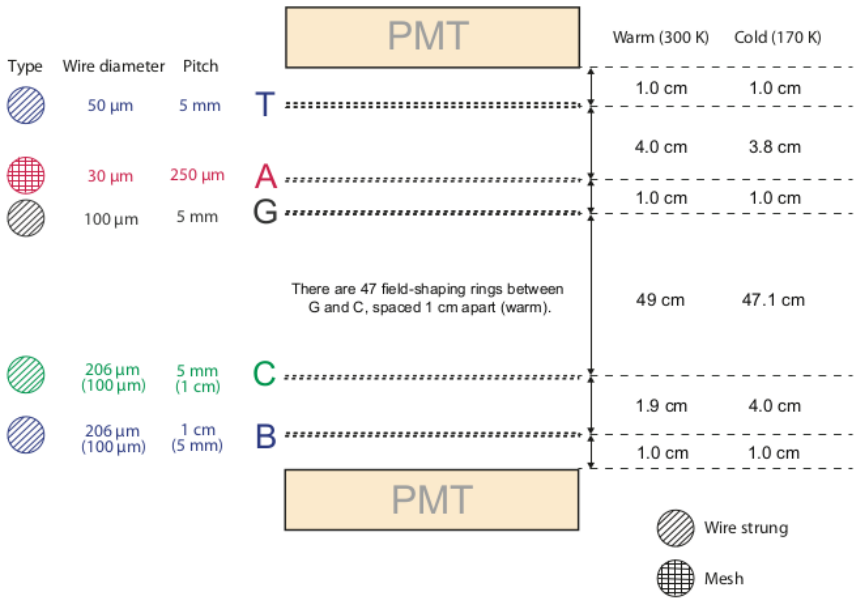

Figure 2.11: This diagram shows the spacing and positioning of the various grids, the grid pitch, and the grid wire type. The primary values shown correspond to those during the WIMP science runs, Run03 and Run04, whereas information in parentheses indicates the value during the surface run, Run02. Key for the figure: T - top PMT shield, A - anode, G - gate, C - cathode, and B - bottom PMT shield. Figure reprinted from [18].

above the first half of its frame, and the sides of the mesh iteratively stretched in order to avoid wrinkles, and then the top half of the frame secured the mesh in place. Tensioning of the anode was fine-tuned by the use of a torsioning driver on the set screws. Each of the set screws, which were adjusted in a star-shaped pattern, was tensioned to 2 oz/in^2 [59].

The experiment had the remaining cathode, gate, and top and bottom PMT shield grids constructed of wire planes. The cathode grid and bottom PMT shield grid used 0.0206 cm ultra-finish 302 stainless steel wire with 0.5 cm pitch and 1.0 cm pitch, respectively. The top PMT shield grid and gate grid used 304 stainless steel, with their respective diameters constructed as 0.00508 cm and 0.01016 cm, with both having 0.5 cm pitch (see figure 2.12 for an example) [59]. Figure 2.11 summarizes information regarding the form and spacing of the grids. To construct the wire plane grids, each frame contained machined holes at their pitches, with the wires held in place by copper washers and secured by silver-plated screws. The proper tensioning of the grids was measured by

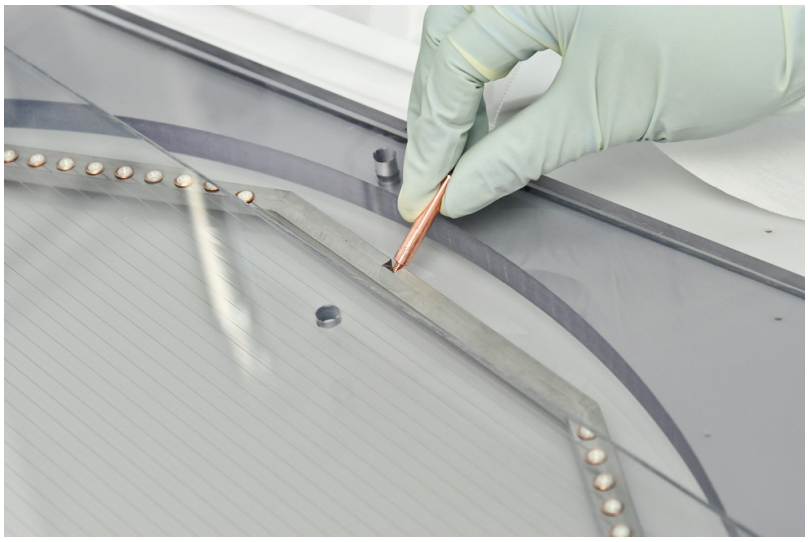

Figure 2.12: This photograph shows a close view of the cathode grid which had 0.5 mm spacing. The copper cylinder shown served as part of the high voltage connection. Photograph reprinted from [59].

noting the standing wave patterns that result from an induced mechanical resonant frequency on the wires. Knowing the linear density of the wires and calculating the frequency from the wave patterns, enabled the calculation of wire tension. The optical transparency of each grid used in the main science runs was as follows: top 99%, anode 88%, gate 99%, cathode 96%, and bottom 98% [18]. It is simple to note that the non-anode grids had a significantly improved optical transparency in comparison to the anode. Indeed, the collaboration chose wire plane grids instead of mesh grids in order to improve optical transparency and facilitate the high level of light collection demanded by the experiment [18].

Along the length of the fiducial volume of the detector, 47 field-shaping rings were placed at 1 cm intervals between the gate and cathode grids as in figure 2.13. The rings helped to maintain the electric field throughout the length of the electron drift region. The field-shaping rings were machined from oxygen-free high conductivity copper, and similar to the rest of the detector internal structure, had a dodecagonal form. Two identical copper pieces formed each ring, one breakpoint held together by a stainless steel staple and the other breakpoint had a copper spacer with a stainless steel spring to allow thermal contraction. Twelve ultra-high molecular weight polyethylene panels

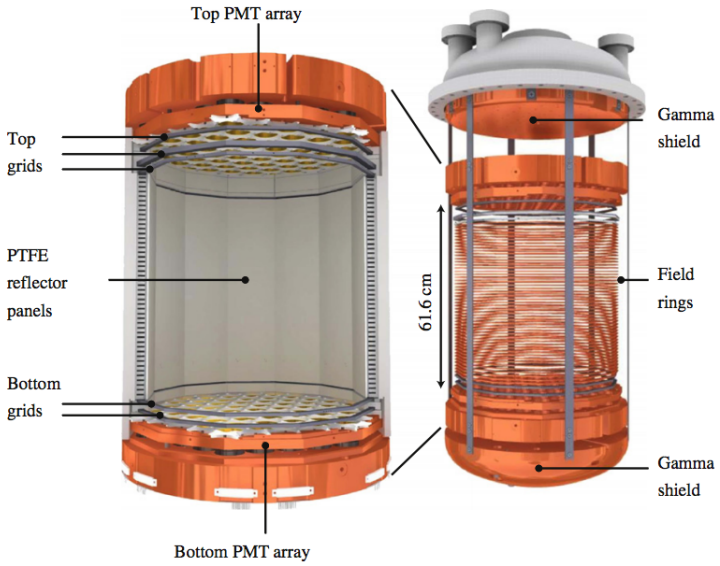

Figure 2.13: This figure shows the internal structures of the LUX detector. Important features here include the grid layout and the electric field rings. The order of the grids from the top of the detector to its bottom were: top PMT shield, anode, gate, cathode, and bottom PMT shield. The 'top grids' section labeled here consisted of the top three grids, whereas the 'bottom grids' section consisted of the final two grids. Figure reprinted from [13].

provided support for the field rings, also arranged to form a dodecagon, and were suspended from the copper top PMT support structure.

A resistor voltage divider connected to the field-shaping rings linearly stepped down the voltage between the gate and cathode grids. By stepping down the voltage, the divider ensured that field lines in the drift region remained vertical near the radial edges. The voltage divider consisted of 1 GΩ resistors in parallel with adjacent field-shaping rings. Then 0.875 GΩ and 1.25 GΩ resistors in turn connected the gate and cathode grids in parallel to the rest of the divider. Mounting each pair of resistors on Cirlex®[3] board gave the voltage divider added support (see figure 2.14).

2.2.4.1 Grid Conditioning

Before the initial and primary science runs (Run03 and Run04) electric field grids were conditioned in order to attempt to raise the possible operating voltages of the grids. Despite LUX having

[3]This work follows the conventions used by the most authoritative published description of LUX components, reference [69], for use of the Registered Trademark symbol.

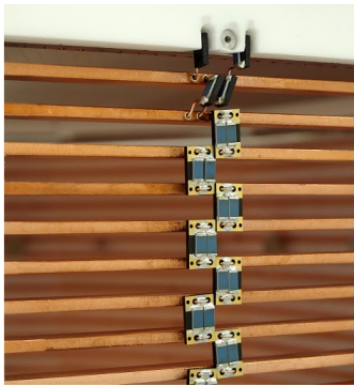

Figure 2.14: This shows the voltage divider which connected to the field-shaping rings and helped to maintain a vertical drift field in the fiducial volume. This upper portion shows how it connected to the gate grid and shows how the resistor pairs were mounted on Cirlex® board. Photograph reprinted from [59].

been constructed in a cleanroom environment, there existed concerns that the grids could become contaminated from dust, hair, Tyvek material, or copper flakes that could have nonetheless gotten into the detector. In the process known as conditioning, or in some places in the literature known as *burn-in*, the voltage of the grids is slowly increased until there is noted current, then the voltage is held constant until hopefully, the current decreases as asperities on the grid wires burn off, and this cycle continues until no more benefit becomes apparent or frequent breakdown occurs. An example of discharge under grid conditioning can be seen in figure 2.15.

Initial conditioning was carried out at Texas A&M University prior to Run03, before installation into the detector. Specifically, for Run03 the gate and cathode grids were conditioned in liquid xenon, but this campaign was considered unsuccessful [59]. Prior to Run04 the anode and gate grids were conditioned in cold xenon gas while the bottom PMT shield and cathode were conditioned in warm xenon gas, all while the grids remained inside the detector. After the conditioning campaign ended, the anode and gate grids could operate at a higher voltage, but the cathode could no longer operate at its Run03 voltage. The diminished capabilities of the cathode could have been the result of damage from the conditioning campaign; the post-Run04 deconstruction of LUX noted seemingly burnt and distorted wires which may have received damage from conditioning (see figure 2.16). The overall drift fields however did increase, resulting in a higher electron ex-

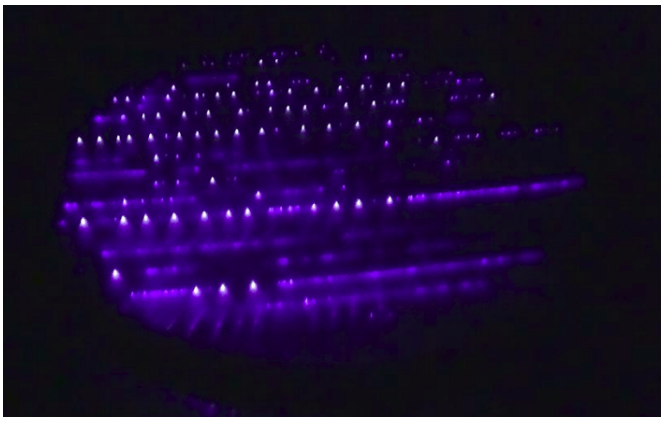

Figure 2.15: The above photograph shows grid discharge in argon under conditioning. Conditioning aims to allow discharge to occur while burning off any residual material with the aim of increasing the maximum voltage maintained by the grids.

traction field at the gas-liquid interface. Following the conditioning, unfortunately, the PTFE walls did see increased luminescence, which postponed the start of Run04, and Run04 was beset with a time-dependent radial electric field in a manner unseen in Run03. A likely cause for the high currents introduced into the detector was charging of the PTFE walls during the extensive conditioning campaigns for the grids [13]. Due to the time-dependent fields present in Run04 and the difficulties associated with position reconstruction throughout the bulk of the detector, the analysis presented here shall remain limited to Run03 data exclusively.

2.3 Calibrations

Several calibration methods were devised in order to fine-tune the signals from LUX, with each one regularly performed during the science runs, or, in the case of more complicated calibration sources, done at major benchmarks. Internal calibration sources had been incorporated into the design of LUX and its plumbing structure such that the circulation path allowed for the xenon to be able to pass through the source and draw it into the detector. The internal sources used in LUX were metastable krypton-83 ^{83m}Kr and tritiated methane CH_3T. External sources such as ^{137}Cs and a deuterium to deuterium (D-D) neutron generator were also implemented.

Figure 2.16: The above photograph shows a damaged grid wire discovered during the LUX post-mortem investigation of the grids. The image appears to show a wire that had been heavily burnt and deformed, possibly having resulted from the conditioning campaign.

2.3.1 Tritiated Methane

Tritiated methane (CH_3T) provided an ideal source for electron recoil calibrations of the detector due, in large part, to the fact that the β particle energy spectrum emitted from tritium has a mean of 5.6 keV, a maximum value of 18.6 keV, and the majority of its interactions have energies below mean [59]. Following an injection, over the course of several hours, or days for larger injections, the methane produced clear S1 and S2 signals to be seen by the detector. Although its energies span the range of dark matter experiments, the getter purification system was required to be able to remove the methane, lest it linger in the detector with a 12-year half-life. The residual gas sampling system confirmed the removal of the methane with a time constant of 5.9 $\pm$ 0.07 hours [66]. Detected light from an event plotted as $\log(S2/S1)$ vs $S1$ integrated pulse areas reveals distinct electron recoil and nuclear recoil bands. Through tritiated methane calibrations, LUX determined the electron recoil band, which was expected to be Gaussian in $S1$, via plotting the aforementioned $\log(S2/S1)$ vs $S1$. Proper determination of the electron recoil band in LUX was essential because the dominant background form in the detector was electron recoil leakage into the nuclear recoil band. The nuclear recoil band occurs directly below the electron recoil band in the aforementioned

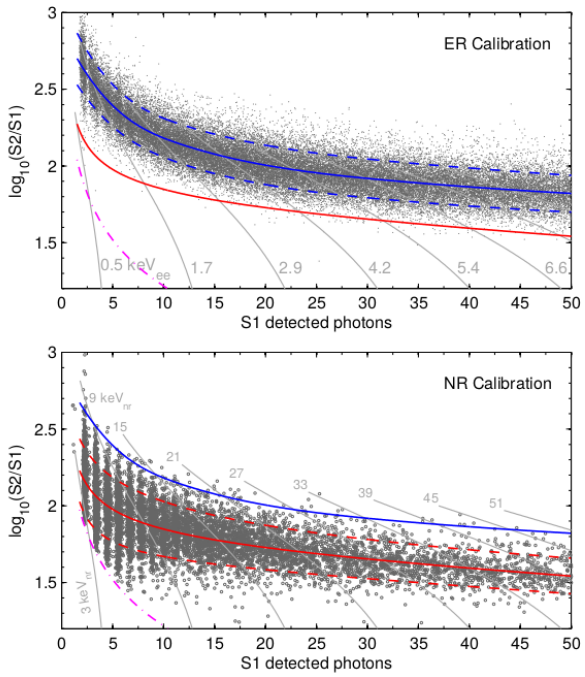

Figure 2.17: The top figure shows the electron recoil band defined by the results from the tritiated methane calibrations, whereas the bottom figure shows the nuclear recoil band resulting from the D-D neutron calibrations. These figures were created by Cláuido Silva of the LUX Collaboration but reprinted from [60].

parameter space as can be seen in figure 2.17.

2.3.2 Metastable Krypton-83

Another calibration source used internally to the LUX detector was metastable krypton-83 (^{83m}Kr). ^{83m}Kr decays quickly via internal conversion electrons with a half-life of 1.86 hours into radioactively stable ^{83}Kr. The decay of ^{83m}Kr occurs in two stages, the first at energy 31.1 keV and the second at 9.4 keV, with the emitted electrons producing notable double scatter electron recoils. Both steps can be viewed as a single event because the second energy deposition occurs only 154 ns following the first [73]. Due to the fact that ^{83m}Kr decays so quickly, it would have been foolhardy to attempt to store it en mass for calibration purposes. Instead, the xenon circulation system in LUX had piped into it a source of ^{83}Rb which decays to ^{83m}Kr with an 86.2-day half-life. The calibration system injected ^{83m}Kr into the detector by passing Xe gas through the circulating piping system where ^{83}Rb was stored in order to flush the ^{83m}Kr into the detector, and very quickly,

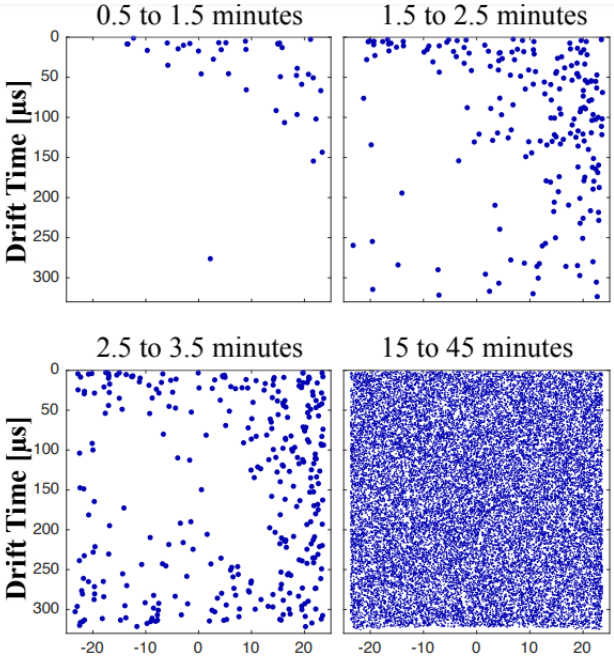

Figure 2.18: This figure shows a time-lapse of detector response following the injection of ^{83m}Kr. Note how the events quickly become dispersed throughout the detector and achieve uniformity. Figure reprinted from [72]

.

within 10 minutes, krypton events registered throughout the xenon bulk (see figure 2.18). The krypton calibrations were important for the calculation of corrections to the pulse area calculation, provided information about top PMT array to bottom PMT array asymmetry, and during the main run of LUX, Run04, where there were variable fields, the krypton calibrations provided much-needed information about properly reconstructing the (x, y, z) positions of events throughout the active region of the detector. Corrections to the (x, y, z) positions and pulse areas within the detector proved essential due to non-uniformity of pulse area reconstruction from different reconstructed positions such as those presented in figure 2.19. The ^{83m}Kr provided higher overall electron recoil energies than the tritium as well as discrete energy peaks for low energies.

2.3.3 Neutron Generator Calibrations

Nuclear recoil detector response remains distinct from electron recoil response due to the larger energy scale-dependent heat loss component of the interaction, and to calibrate for this the Deu-

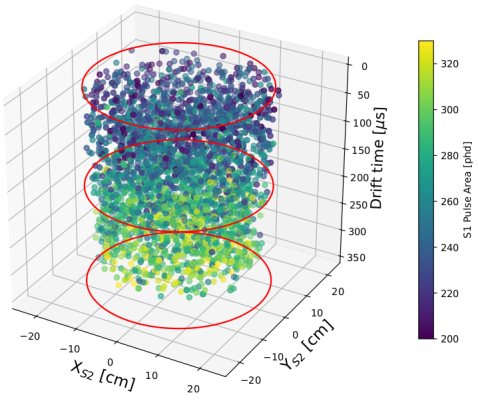

Figure 2.19: This figure shows uncorrected S1 distributed throughout the fiducial volume of the detector for ^{83m}Kr events. Note how the observed uncorrected S1 pulse areas appear to be dependent upon detector depth of their corresponding S2. Energy corrections proved vital for proper energy reconstruction, and such corrections could not have been calculated without proper calibration afforded by the regular use of ^{83m}Kr injections. Figure reprinted from [13].

terium to Deuterium (D-D) generator produced free neutrons directed into the detector. The D-D generator works as a compact particle accelerator such that deuterium ions accelerate towards the deuterium filled target, situated outside of the water tank. The interaction produces a free neutron and a helium-3 (^{3}He) nucleus via D + D $\rightarrow$ n + ^{3}He with the neutron having a known outgoing energy of 2.45 MeV [13]. The flow of outgoing neutrons selected those traveling at 90° to the plane of acceleration and directed them as a highly collimated beam towards the detector using a PolyVinylChloride (PVC) tube filled with air suspended in the water tank (see diagram in figure 2.21). The impact of neutrons scattering in the detector is depicted in figure 2.20. Simulations of neutron scattering within the detector indicated that incident neutrons scatter in the detector having an energy within 6% of the source energy, making this calibration a reliable means of determining detector response [74].

Knowing the kinematics of the nuclear recoil, the deposited energy E_d has the equation

$$E_d = E_{n_i} \cdot \frac{4 m_n m_{\mathrm{Xe}}}{\left(m_n + m_{\mathrm{Xe}}\right)^2} \sin^2\left(\theta_{CM}\right) \tag{2.11}$$

where E_{n_i} is the initial energy of the neutron, m_n and m_{Xe} are each the masses of the neutron and

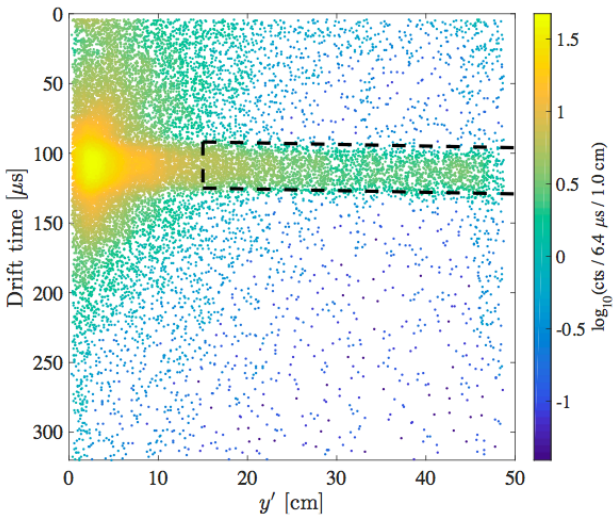

Figure 2.20: Nuclear recoil events during a 2013 D-D neutron calibration run shown in y-z profile with y′ defined in the direction of the neutron beam. Energy depositions spread somewhat with small y′ from scattering off of detector materials, with the black dashed lines indicating events specifically from the neutron beam. Figure reprinted from [75].

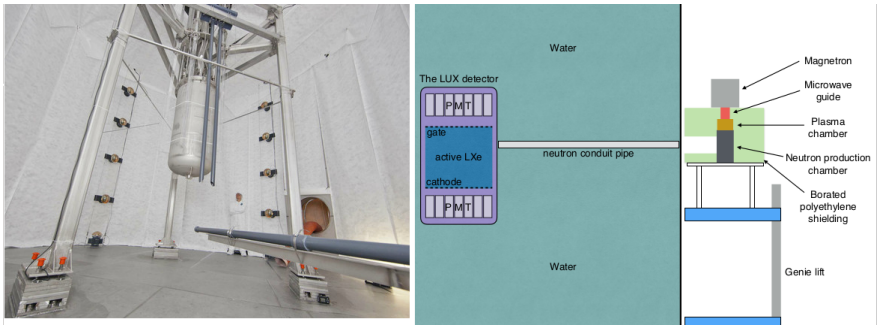

Figure 2.21: The photograph on the left comes from inside the LUX water tank showing the PVC collimator pipe used to focus the neutrons coming from the D-D generator. During a neutron calibration campaign the operator raises this pipe perpendicular to the detector. The right figure is a cartoon showing the D-D generator setup. Images adapted from [59] (left) and [13] (right).

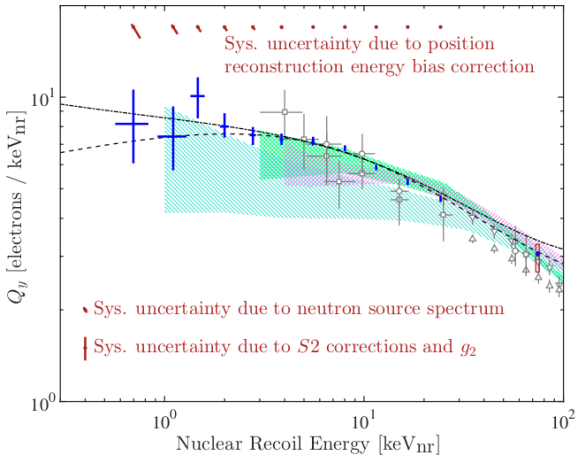

Figure 2.22: Figure shows charge yield (Q_y) as a function of nuclear recoil ionization in liquid xenon. Figure reprinted from [75].

xenon, and θ_{CM} is the scattering angle of the neutron relative to the PVC tube in the center of mass frame. However,

$$\tan(\theta_{lab}) = \frac{\sin(\theta_{CM})}{\frac{m_n}{m_{\text{Xe}}} + \cos(\theta_{CM})} \tag{2.12}$$

implies that the scattering angle in the center of mass frame is nearly that of the lab frame θ_{lab}.

The experiment measured the ionization yield in liquid xenon for single scatters between 1.08 and 12.8 keV$_{nr}$, and for multiple scatters as $E_d = 0.3 - 30$ keV, using the D-D generator [13]. The primary interest of the experiment concentrated on single scatter events having a single S1 with a single S2; thus, the single scatter data from the D-D generator served as the basis for the nuclear recoil band, with a defined nuclear recoil sensitivity of 1.1 keV$_{nr}$, and pushed LUX WIMP sensitivity down to 3.5 GeV/c^2 as shown in figure 2.22 [60]. WIMP searches, concerned with a single S1 and single S2 nuclear recoil signal, can easily exclude events that have multiple S1 or S2 pulses, as well as anything lying in the electron recoil band. Figure 2.17 on page 54 shows the electron and nuclear recoil bands resulting from the tritiated methane and D-D calibrations.

2.3.4 Other Calibration Sources

Prior to the use of the D-D generator, encapsulated ^{241}AmBe and ^{252}Cf provided calibration energies for nuclear recoil energies for the Run03 WIMP search [59]. Additionally, encapsulated ^{137}Cs was used for electron recoil calibrations, performed weekly during Run04. These encapsulated sources were placed in a tungsten collimator and lowered into the water tank at a specific height, with the collimator pointing towards the detector. The height of source placement could be varied, and the azimuthal position of the source also could be varied in six positions around the circumference of the detector. The ability to test different heights and angles proved essential in determining if there existed any errors in position reconstruction.

2.4 Background Reduction

As previously mentioned, LUX strove to reduce backgrounds as much as possible in order to improve its overall sensitivity. Prior to installation, assaying teams at the Soudan Low-Background Counting Facility (SOLO) and Berkeley Oroville Facility, measured the radioactivity of all interior detector components [69] [76], as well as the cryostat [77]. LUX had budgeted the radioactive contribution of these components, simulating the projected Run03 backgrounds to be $2.6 \pm 0.2_{stat} \pm 0.4_{sys}$ mDRU$_{ee}$, where 1 DRU = 1 event/kg/keV/day, with $3.6 \pm 0.3_{stat}$ mDRU$_{ee}$ in the fiducial volume observed in the range 0.9 - 5.3 keV$_{ee}$ [76]. For Run04, the projected backgrounds in the fiducial volume amount to 1.4 $\pm$ 0.2 mDRU$_{ee}$ + 350 nDRU$_{nr}$, and were observed as 1.7 $\pm$ 0.3 mDRU$_{ee}$ in the energy range 0.9 - 5.3 keV$_{ee}$ and 3.4 - 25 keV$_{nr}$ [76]. LUX employed copper gamma shields above and below the detector and also employed a water tank veto and shield. Of course, the self-shielding properties of xenon, as mentioned near the beginning of this chapter, further reduced backgrounds. Also, due to the fact that ^{127}Xe occurs as a result of cosmogenic activation, once underground, with a half-life of only 36.4-days, the isotope becomes quickly eliminated [18]. Thus, as ^{127}Xe reduced in concentration, the overall radio-purity of the entire xenon bulk improved.

Although the getter system removed non-noble contaminants from the xenon in the detector,

it did not remove noble elements such as krypton and argon which exist in commercially available research-grade xenon sources. Trace levels of ^{85}Kr and ^{39}Ar could linger in the detector and become problematic because they are both long-lived β emitters. The collaboration created a chromatographic separation system to separate xenon from remaining krypton and argon contaminants, and through this system reduced ^{85}Kr from 130 ppb to 3.5 ppt and ^{35}Ar to $\sim$1 ppb prior to deployment [78].

Furthermore, the experiment was located approximately a mile underground (4,300 mwe) in order to prevent or screen backgrounds [69]. From the surface run of LUX, Run02, the measured muon flux of 0.019 $\pm$ 0.003 cm^{-2} s^{-1} resulted in an event rate inside the detector of 108.8 $\pm$ 0.3 Hz [67]. In contrast, the muon flux at the 4,850 level in the Homestake Mine measured $(0.044 \pm 0.001) \cdot 10^{-7}$ cm^{-2} s^{-1}. Thus, rock overburden limits muon flux to approximately one muon event per day in the detector [79]. Consequently, the rock overburden should limit LIP flux as well, but a surface-based detector would otherwise have large resulting muon noise, making a WIMP or LIP search impossible. High energy particles such as those produced in the upper atmosphere should have sufficient energy to penetrate the rock and be detected.

2.4.1 Water Tank and Veto System

A water tank shield and veto system surrounded the LUX detector. The tank had a diameter of 8 m, a height of 6 m, and was filled with 270,000 L of ultra-pure water with a mass of 77,000 g (see figure 2.23) [18]. The veto system functioned such that a cosmic ray would produce Cherenkov radiation which would be detected by 20 PMTs within the tank. If the cosmic ray were to strike the nearby rock and produce neutrons, which often have a similar energy pattern to an expected WIMP signal, the timed veto would be used to exclude that event as a candidate. The veto consisted of 20 PMTs which were Hamamatsu R7081 with a diameter of 10 in and a coverage area of approximately 530 cm^2 [80]. The PMTs lined the water tank sides and floor, with five PMTs situated at each of the four cardinal directions. Tyvek covered the walls and floor of the tank in order to increase photon detection efficiency. Unfortunately, however, the veto was not employed throughout Run03 and only became fully operational in Run04. Consequently, this analysis which

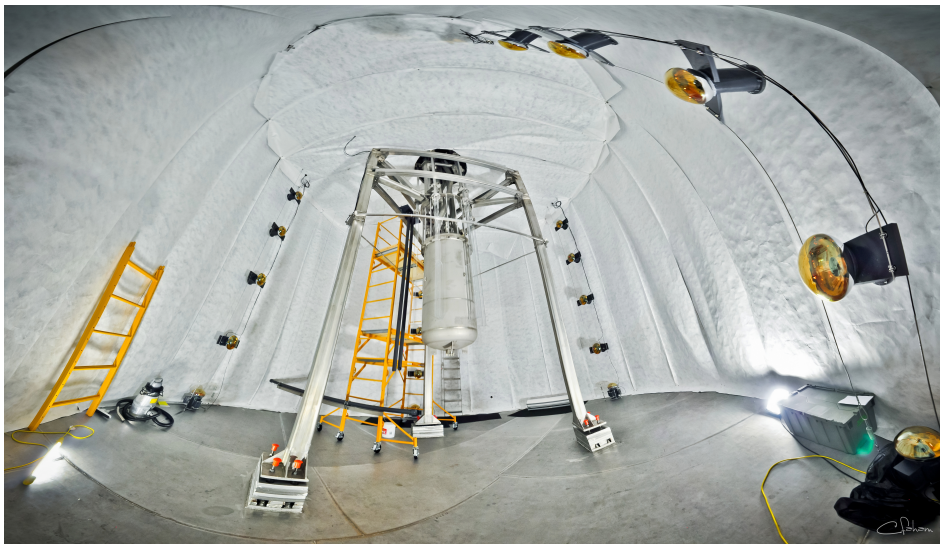

Figure 2.23: This picture came from inside the LUX water tank muon veto system prior to being filled with water. Minimum water shielding was 2.75 m above, 3.5 m along its circumference, and 1.2 m below. It contained 270,000 L of ultra-pure water. Included in the picture are some of the Hamamatsu R7081 10 in PMTs for detection of Cherenkov radiation, which were in operation for Run04. Picture reprinted from [18].

focuses exclusively on Run03 cannot make use of veto data. It stands to reason that LIPs should deposit energy in the water tank and any LIP investigation encompassing Run04 is encouraged to make use of the veto data.

Some interesting history regarding the water PMTs is that they were initially designed to run as a part of Run03. Initially for Run03, a LeCroy 1458 HV crate supplied PMT high voltage with a positive voltage bias used for the xenon PMTs and a negative voltage for the water PMTs. The LeCroy crate failed shortly into the run and a Weiner MPOD power supply replaced it, but the new supply did not have any positive voltage modules to be used with the water PMTs [80]. Additional modules were obtained for Run04 which allowed the water PMTs to be biased by the same power supply as the xenon PMTs. Thus, the water PMTs could not be used for most of Run03 but were in operation for Run04.

2.5 Data Acquisition

The Data AcQuisition (DAQ) system was the means through which waveform readout from the PMTs was converted into files storing the relevant digital information. The PMTs continuously readout any detected signal but would only save the information when signal levels passed threshold conditions. The final output of the DAQ was called the 'dat' form of the files which would later be translated into 'evt' and 'rq' files.

Upon detecting some signal, the PMTs would produce an analog output that propagated along an RG-178 50 Ω coaxial cable to the breakout cart. At the breakout cart, the signal would undergo pre-amplification by a factor of five. Each PMT within the xenon space had unique cable for its channel leading outside of the detector. Then, the cables passed through a feed-through in groups of 32 as they connected to the pre-amplifier. The signal would then be transferred via an RG-136 50 Ω cable to the post-amplification receiver at the main DAQ rack where each channel would have three amplification channels. Of the post-amplification channels, the first provided a 1.5 gain factor for the Struck digitizers, the second output produced a 2.8 gain factor for the DDC108 trigger system, and the third output provided an 18 gain factor for CAEN discriminators.

LUX made use of 17 SIS3301 eight channel ADC Struck boards, 16 of which read out the xenon PMTs and one for the water PMTs [13] [69]. Each xenon PMT read out to its own channel in the boards, but only eight channels had been reserved for the water PMTs. Each channel had 14 bits resolution, digitized using a 100 MHz sampling frequency, and had a 30 MHz cutoff frequency prior to being digitized [18]. The boards functioned in what was called Pulse Only Digitization (POD) mode. POD mode functioned such that when the PMT signal amplitude, also known as the POD rate, went above the previously specified detection threshold then the waveform would be digitized, and digitization would be discontinued when the POD rate dropped below the previously programmed end threshold. Furthermore, the boards would record the 24 samples of data before the threshold start time and 31 samples subsequent to the end time, where 1 sample is equivalent to 10 ns [18]. The Struck boards acquired POD data in pairs of PMT channels (e.g. 1 with 2, 3 with 4, and so on), and acquisition of data could occur when one or both of the channels caused

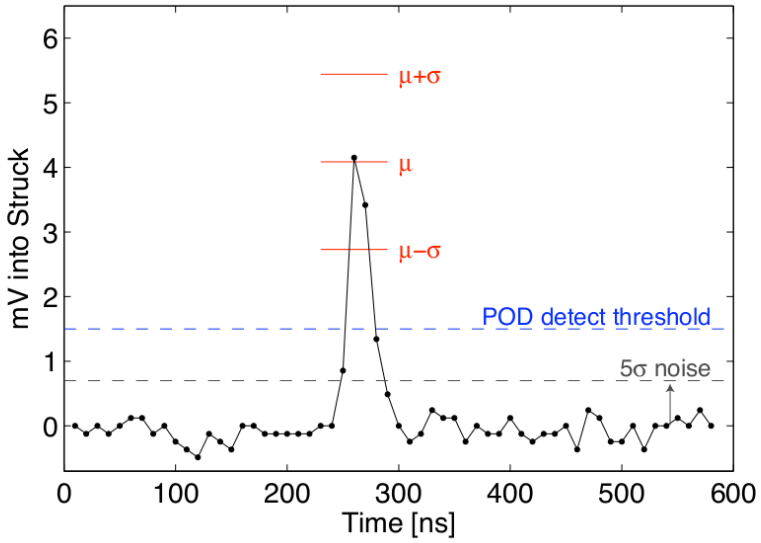

Figure 2.24: This figure shows a typical response from one of the xenon PMTs at a gain of $4 \cdot 10^6$ while detecting a single photoelectron. The figure includes the mean height of the pulse μ, one standard deviation σ fluctuation from the mean, and the 5σ noise baseline. With this POD detection threshold PMTs have >95% detection of single photoelectrons. Figure reprinted from [55].

the POD rate to surpass detection threshold. The POD rate for both channels must have decreased below the end threshold to meet its termination criterion. Typically set to 1.5 mV and 0.5 mV, respectively, the pulse detection threshold and pulse end threshold had been set to a level such that there would be 95% efficiency for single photoelectron detection in each channel [60]. The detection threshold of 1.5 mV assured that the signal would be more than 5σ above the measured baseline noise fluctuations (see figure 2.24).

LUX used a custom on-line hardware trigger system that made use of digital-to-digital converter processing boards [60]. There were two digital-to-digital converter DDC-8 boards, each with eight channels, which made up the DAQ system [60]. The trigger boards identified S1 and S2 pulses within the stream of data by using a double Hogenauer filter and calculated their pulse areas in real-time. Incoming pulses with a narrow width of 125 ns were identified as S1 pulses, and wide width pulses of 1 - 2 μs were designated as S2 pulses [18]. The trigger system could be set to S1 mode, S2 mode, or both, the latter of which would require detection of an S1 and an S2. When the trigger conditions were met, the pulse would be digitized in the dedicated Struck channel and

added to the data stream [18]. There was a threshold of 8 phd for the filtered signal of each trigger group. In order to prevent spurious triggers following a larger S2 pulse, a hold-off period of 1 to 4 ms was observed after each trigger, but despite this hold-off period, the trigger configuration had 99% efficiency for S2 signals of 100 phd [81].

The Event Builder program isolated the PMT signals that had been digitized within the time window and converted the signal to waveform-containing evt files from the dat files. If an error occurred in the topological layout of the recorded event the dat files could be reprocessed with the Event Builder to produce new evt files and avoid livetime loss. Thus, the data acquisition software afforded maximum efficiency in data recording and processing for desired events. The evt files were then processed, and have been reprocessed for the purposes of the LIP search, into rq files. The process of converting evt files to rq files is detailed in section 3 dealing with the Data Processing Framework (DPF).

3. THE LUX DATA PROCESSING FRAMEWORK

The LUX Collaboration created a suite of analysis software in order to process raw data coming from the PMTs into quantities relevant for the WIMP search known as the Data Processing Framework (DPF). First, the Event Builder (see section 2.5) converts the dat files to evt files, and afterward, the DPF is then used to convert the evt files to rq files with relevant Reduced Quantities (RQs) being saved. Such RQs included finding the points where a pulse signal returned to baseline thereby indicating the end of the pulse, calculation of the integrated pulse area, and discerning whether pulse characteristics resemble an S1, S2, or various other pulse types.

Designed in a modular format, the DPF contained modules written in both Matlab [82] and ROOT/C++ [83] with a Python [84] wrapper. The wrapper allowed modules coming from various different members of the collaboration to work together in a more or less language-independent fashion. There have been various instantiations of the DPF, continuously being improved for relevant datasets. This analysis has dealt with basic and modified modules from DPF version 2.0, chosen due to the fact that the Run03 reanalysis paper used version 2.0 for its data processing [85]. Figure 3.1 shows a pictorial overview of the standard DPF modules, the data processing chain, and how the DPF utilizes stored acquisition information.

3.1 Settings

There are two settings files that are required for various modules within the DPF. The first, simply known as the data processing settings xml file, can be generalized for large parts of the science run. The second file, called the LUG IQ xml file, contained information unique to the detector conditions at the time of acquisition which could vary slightly throughout the run. For simulation processing for this analysis, generalized versions of both of these files were used. For the processing of live data, the general Run03 data processing settings xml was used in conjunction with the specific LUG IQ xml of the acquisition.

The data processing settings xml file includes information for the DPF to find various mod-

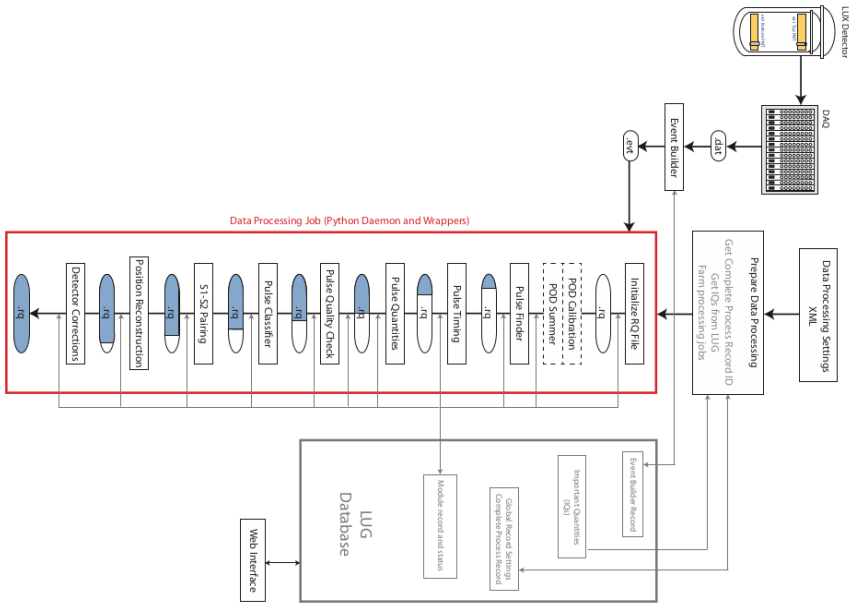

Figure 3.1: This image is a pictorial representation of the DPF. First, PMT signals read out to the DAQ where the DAQ determines if sufficient POD rate has occurred to save the signal, which results in the dat file. Next, the Event Builder program converts dat files into evt files as waveforms. The DPF then queries the LUG logbook and processes the file to the final RQ product. Image reprinted from [18].

ules. It specifies the order in which modules will run and the input parameters for the modules. Additionally, it has settings to indicate which PMTs were off for the run, the parameters for the pulse finding module, and where general PMT setting information existed. Most importantly for the LIP search, this file determines how many pulses could be classified within an event. This part of the standard data processing framework limited the number of discernible pulses within an event to ten which is logical for a WIMP search that expects only a few pulses, but a LIP of sufficient charge could leave dozens of small pulses along the detector length. Therefore, in order to look for many pulses, the data needed to be reprocessed to allow for the pulse finding algorithm to find as many as 100 pulses in an event. The standard LUX DPF would discard pulses in events beyond the standard ten, leaving almost no information about them in the final RQ file, but increasing the maximum pulse limit saved them when reprocessed for the LIP search.

The collaboration made use of a MySQL database known as the LUG electronic logbook. The

database serves as the repository location where detector deployment information, DAQ and trigger settings, etc. are stored. Much of this information is stored as a table of Important Quantities (IQs) which make up the LUG IQ xml file. Such information includes the relevant krypton calibration or other source calibration data, electron lifetime measurements, detector tilt measurements, and position corrections. Regarding the PMTs, the LUG IQ file contains PMT gain calibrations, light response functions, and after-pulsing measurements. In reprocessing the data for the LIP search, the DPF downloaded the corresponding file for the acquisition via a virtual private network. No modifications have been made to the LUG IQ file for the LIP search.

3.2 Modules

The first module in the DPF is called Initialize_RQ_File and it creates the rq file which will eventually become a final product of the framework. The only inputs are the two settings files and the evt file. The rq file initially receives only live-time calculations and settings information. Subsequent modules will read information from the rq file as well as add information to it in the form of RQs.

3.2.1 Initialization Modules

Next, the first module of analytical consequence is called PulseCalibration_BaselineZen which serves as a means for calibrating the POD waveforms. Specifically, it corrects for baselines which have been skewed as reported by the DAQ. There is a rolling buffer of 32 samples (1 sample equates to 10 ns), but skewed baselines could occur when one POD follows another in the same channel within 32 samples of the baseline averaging calculation. The skewed baseline could occur because if there are not 32 samples for the averaging calculation then the software has set the remaining samples to zero. The baseline module identifies these problematic PODs in the event that this issue of 32 samples occurs and sets the POD baseline to that of the previous POD (see figure 3.2).

Furthermore, the PulseCalibration_BaselineZen module utilizes PMT calibration information and single detected photon calibrations in order to convert the mV/sample waveform amplitudes from the evt file to phd/sample. The module also creates a cvt file which stores the phd/sample

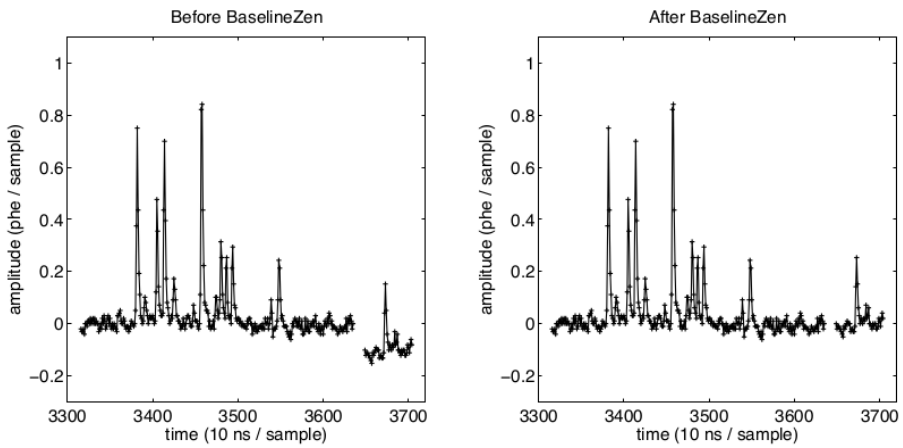

Figure 3.2: These figures show two PODs, one following the other within 32 samples. The left figure shows the second POD having a skewed baseline prior to further processing. The right figure shows the same two pulses after having been corrected by PulseCalibration_BaselineZen where the second POD now has the same average baseline as the POD preceding it. Figures reprinted from [86].

amplitudes. The cvt file becomes an intermediate file that the DPF can modify and from which the DPF reads waveform information throughout most of the remaining DPF modules without the possibility of modifying or harming the evt file.

The PODSummer_LUXSumPOD as its name suggests, sums the PODs in all channels (see figure 3.3 for an example). In the standard evt or cvt file, all energy recorded by the PMTs has an associated sample timing, and when the times for the unique samples overlap, the POD summing module adds the phd/sample amplitudes from the channels to form the unified pulse or event waveform.

3.2.2 Pulse Delineation

Perhaps the most important module in the DPF, the PulseFinder_TransparentRubiksCube module finds the various pulses within the waveform. The pulse-finding module finds, and, if possible, separates various pulses within the event by passing a 400-sample integrating boxcar filter over the summed POD waveform. When the boxcar finds sufficient pulse amplitude, discarding any pulse with less than four samples, it determines the maximum pulse amplitude within the pulse. From

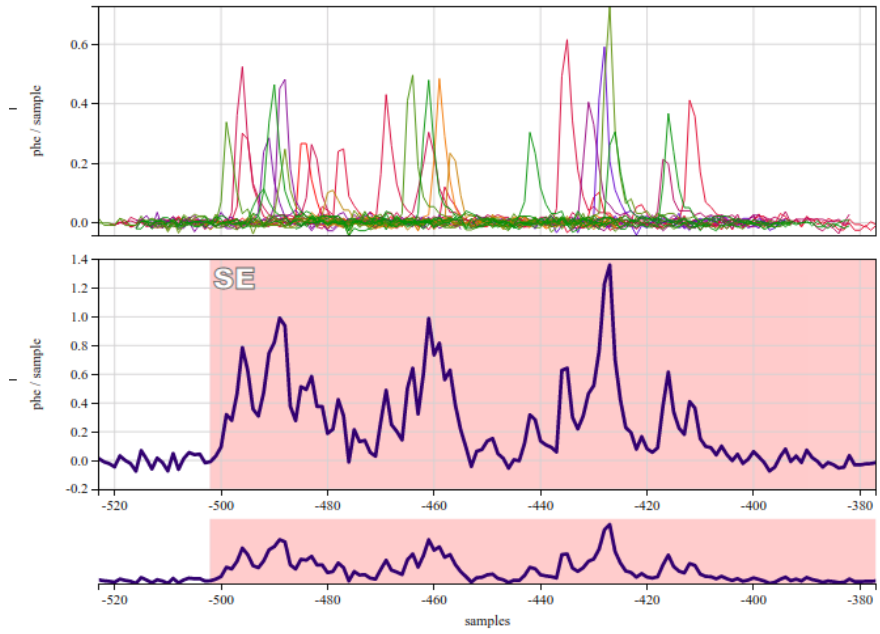

Figure 3.3: These figures show a single electron pulse. The top figure has PODs from each individual PMT overlapping, whereas the bottom has the sum over all PMTs which comprises the summed waveform. PODSummer_LUXSumPOD module creates the summed waveform in the DPF. This particular event, shown using the Visualux viewer has LUXstamp 7731858163181980.

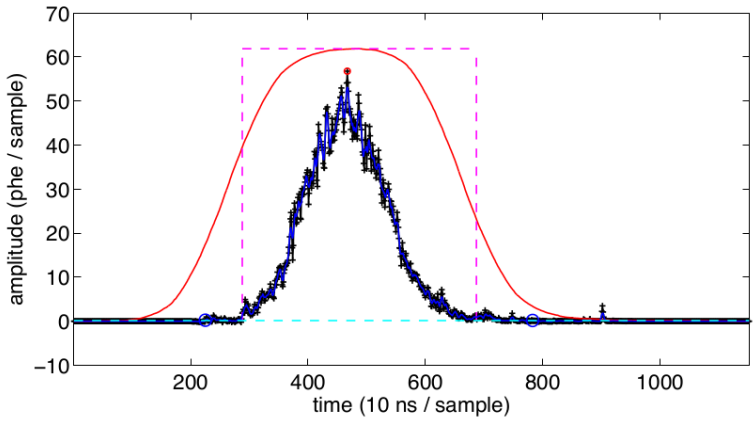

Figure 3.4: The above figure shows how the PulseFinder_TransparentRubiksCube module finds a pulse. A 400-sample integrating boxcar filter, its output represented as the red line, passes over the summed POD waveform. The magenta line bounds the maximum output of the boxcar. The summed POD waveform itself is shown as the black line, whereas the blue is the smoothed waveform. The red circle is the maximum height of the waveform, from which the program steps in either direction until the smoothed signal drops below the cyan line for 50 samples. The point where the signal drops to baseline then becomes the start or end time for the pulse; start and end times are denoted via the blue circles. The pulse shown here will eventually be classified as an S2. Figure reprinted from [86].

the maximum amplitude point, the program steps in either direction to determine the endpoints of the pulse. The stepping is done on a smoothed version of the waveform with a $\pm$ 2 sample moving average, and stepping ceases when the amplitude of the waveform drops below 0.15 phd/sample for 50 samples [86]. See figure 3.4 for a visual example of the boxcar mechanism. The start and end of the pulse are determined by the first sample where the amplitude is below the 0.15 phd/sample threshold. The results from the pulse finding module provide the start and stop times for all found pulses. The pulse finder usually limits itself to ten pulses, but for the LIP search this has been increased to 100 pulses; the DPF reprocessed all Run03 events, merely changing the limit of pulses which it could find, for the LIP search.

The subsequent module, PulseTiming_HeightTiming calculates various timing parameters at the pulse level. Of particular interest are RQs dealing with the timing when various percentage benchmarks of the pulse area have occurred, such as 1%, 99%, etc. The area timing RQs become important when looking for pulses that have a baseline shift before or after the main area of the pulse. The situation where a pulse has a very long time between 99% and the pulse end could indicate such a shift. Also of note, only this module and Initialize_RQ_File are typically run as C++/ROOT programs, whereas the rest are usually run as Matlab programs.

PulseQuantities_MinimumSet calculates various event and pulse quantities primarily dealing with the actual area of the pulses and their timing. Some of the more important RQs include the pulse area of pulses in phd, the event pulse area outside of found pulses, and top-bottom PMT array symmetry. This module also flags whether PMT or DAQ saturation has occurred, which often becomes the case in high energy events. Saturation of PMTs or DAQ can have an important impact upon the total amount of light collected via the PMTs because the quantity of light produced by an event might be inaccurately calculated. Other RQs include calculations of the prompt fraction RQ values, namely, prompt fraction and prompt fraction tlx, which are the fraction of the total pulse area occurring within the first 40 ns of a pulse starting at the time of 1% or 10% pulse area, respectively. The two prompt fraction RQ values become important quantities when determining pulse classification, as seen in the following section. The DPF also uses a mod-

ule called PulseQuantities_PhotonCounting which calculates the number of spikes and the pulse widths. In earlier versions of the DPF, PulseQuantities_PhotonCounting existed as a subprogram within PulseQuantities_MinimumSet; perhaps the PulseQuantities_PhotonCounting module was separated for computational time concerns if those RQs were to be deemed unnecessary in future processing.

3.2.3 Pulse Classification

Pulse classification remains an essential part of any rare event search, making PulseClassifier_MultiDimensional, or simply the pulse classification module, of utmost importance. The DPF uses five different classifications for the various pulse types (see table 3.1): 1 indicates an S1 pulse, 2 indicates an S2 pulse, 3 stands for a Single Detected Photon (SDP) (often referred to in older works as single photoelectron or sphe), 4 represents a Single Electron S2 pulse (abbreviated SE and also called a single liquid electron), and 5 signifies none of the previous classifications, also known as an $else$ pulse. The module assigns the value 0 as a placeholder for instances when the maximum number of pulses have not been found in the event, or for situations arising from pulse $chopping$ where no pulse area has been defined within the start and stop times of a pulse, as discussed in section 3.3. Additional pulse classifications, or perhaps best termed secondary classifications, called S1-like and S2-like Class 5 pulses, were given in addition to the previously mentioned Class 5 or $else$ pulses, for the purposes of the LIP analysis. Section 3.3 on page 84 also contains information on S1-like and S2-like Class 5 pulses.

Pulse Classification	Meaning
0	No pulse or no pulse area found
1	S1
2	S2
3	Single Detected Photon (SDP)
4	Single Electron S2 (SE)
5	$else$; None of the above

Table 3.1: Possible standard classifications from the pulse classification module. These classifications do not include secondary classifications given in section 3.3 on page 84.

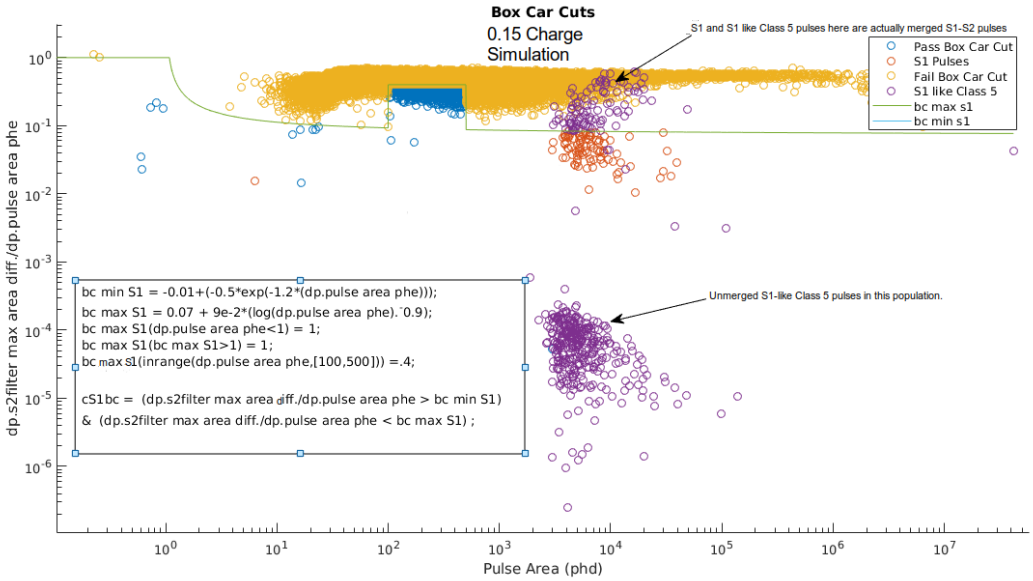

Figure 3.5: The above figure shows the space for the boxcar cut used in S1 pulse classification, here shown with a $0.15e$ charge simulation. The figure is plotted as the boxcar parameter vs the pulse area. The boxcar filter cut looks at the maximum differential of pulse area between a segment of the pulse that has a length of 2 μs and one with 500 ns in length and is defined by the displayed equations. Blue circles indicate a pulse which passes the top-bottom asymmetry cut, the yellow circles indicate those which fail the cut, and the red and purple circles denote S1 and S1-like Class 5 pulses, respectively, regardless of whether or not they fail the cut. The green line indicates the maximum boundary value, and the blue minimum value line has not been depicted in the range of the plot. Two populations of note emerge: an upper grouping of classified S1 and S1-like Class 5 pulses which appear in actuality to be merged S1-S2 pulses; the second grouping lower in the plot shows S1-like Class 5 pulses, which although passing this cut fail other requirements to be classified as S1 pulses, and are all unmerged.

Various requirements for pulses ensure proper classification has been discerned. Priority in pulse-type is as follows if pulses meet the requirements for more than one type: single detected photon, S1, single electron S2, and finally S2. S1 has preference over S2 due to the fact, as stated in the comments of the program itself, that low energy events exist in both populations and tend to be indistinguishable, but are more properly called S1 than S2. S2 and SE pulses are differentiated by energy, but the notion that single electrons could be S2s instead of simply noise has presented itself as relevant to the LIP search, and as mentioned in section 3.3, the LIP search treated all single electrons as S2s for the purposes of correcting energies and positions of pulses.

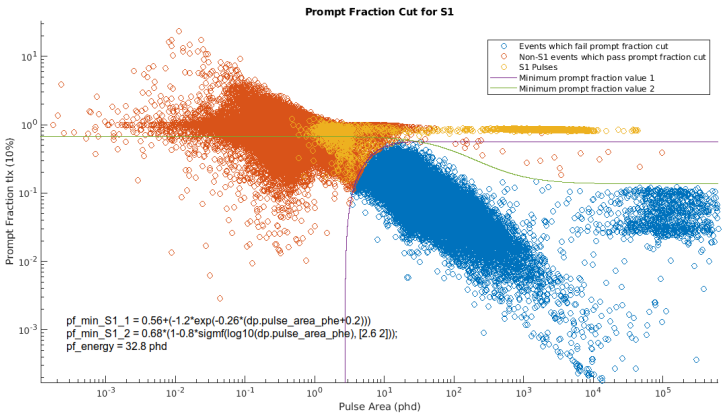

Figure 3.6: The above figure shows the prompt fraction cut space for live data from acquisition rq dataset lux10_20130628T1008_cp27090 as it pertains to S1 classification and displayed as prompt fraction tlx vs pulse area. The prompt fraction tlx RQ is the fraction of the total pulse area occurring within the first 40 ns of a pulse starting at the time of 10% pulse area. Blue circles indicate a pulse which fail the prompt fraction cut, the orange circles indicate non-S1 pulses which pass the cut, and the yellow circles show S1 pulses. The prompt fraction values are defined by the equations displayed and must pass either of two criteria: the value must surpass the first minimum line, shown in purple, and its pulse area should remain $below$ 32.8 phd (known as pf energy); alternatively, the pulse must have a prompt fraction value greater than the second minimum line, shown in green, and have a pulse area $above$ 32.8 phd.

In order to be classified as an S1, a pulse needs to pass four parameter cuts: boxcar filter, prompt fraction, top-bottom asymmetry, and pulse timing width. Additionally, the pulse needed to have a pulse area greater than 0.25 phd as well as a pulse height greater than 0.09 phd/sample in at least two PMTs channels, known as two-fold coincidence. Lastly, the potential S1 pulse needed to not have received a flag indicating that it occurred within the gas region of the detector.

The boxcar filter cut looks at the RQ called s2filter_max_area_diff which indicates the difference between the maximum pulse area within any 200-sample (2 μs) segment in the pulse and the maximum area of any 50-sample (500 ns) segment within the largest 200-sample segment (figure 3.5). The prompt fraction tlx has the same definition as the prompt fraction value described in section 3.2.2, that being that it looks at the fraction of the pulse found in the first 40 ns, with the exception that it uses the time at which it achieved 10% pulse area as its start point (figure 3.6). Prompt fraction tlx has been shown to have greater power discriminating a SE pulse from an S1

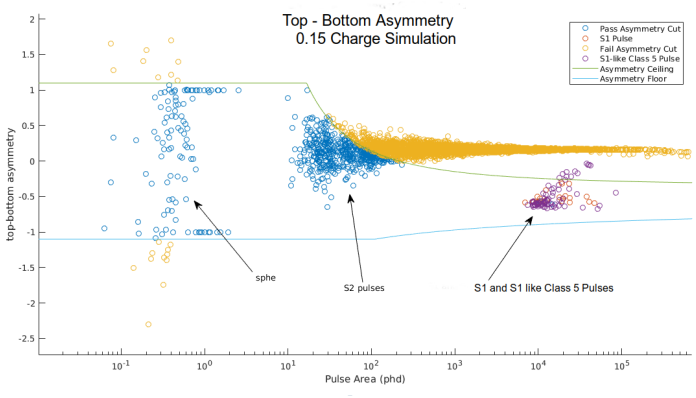

Figure 3.7: The above figure shows the top-bottom asymmetry metric vs the total pulse area for a simulation set of 0.15e charge LIPs. The top-bottom asymmetry metric is defined by $(top - bottom)/(top + bottom)$. The green and blue lines indicate the upper and lower bounds of the cut space, where anything between them passes the cut. The associated equations are displayed showing the limits of the cuts. The figure indicates various populations: single phe (phd) or SDP, S2 pulses, a mixed population of S1 and S1-like Class 5 pulses (see section 3.3 on page 84 for more on S1-like Class 5 pulses). Blue circles indicate a pulse which passes the top-bottom asymmetry cut, the yellow circles indicate those which fail the cut, and the red and purple circles denote S1 and S1-like Class 5 pulses, respectively, regardless of whether or not they fail the cut.

pulse or SDP than the standard prompt fraction RQ [86].

The top-bottom asymmetry cut looks at the difference between the total pulse area of the top PMT array and the total pulse area of the bottom PMT array, and is then normalized by dividing by the sum of the two PMT arrays (figure 3.7). The pulse timing width cut in question is the difference between the time which the pulse has achieved 50% of its pulse area, called $t1$, minus the time at which it achieved 1% area, called $t0$, divided by the difference between the time of achieving 99% pulse area, called $t2$, and the aforementioned 1% timing, i.e. $(t1 - t0)/(t2 - t0)$ (figure 3.8). Note that any cutouts or block-like discontinuities in the lines demarcating the boundaries of cuts in the example plots became incorporated into the code for the S1 filter in order to allow for krypton calibration events which are often a combination of both a 31.1 keV$_{ee}$ S1 and a 9.4 keV$_{ee}$ S1. The associated figures for the four primary cuts associated with S1 classification contain the equations specifying their requirements (i.e. in figures 3.5, 3.6, 3.7, and 3.8).

Interestingly, it appears that there is a clear separation in populations between merely an un-

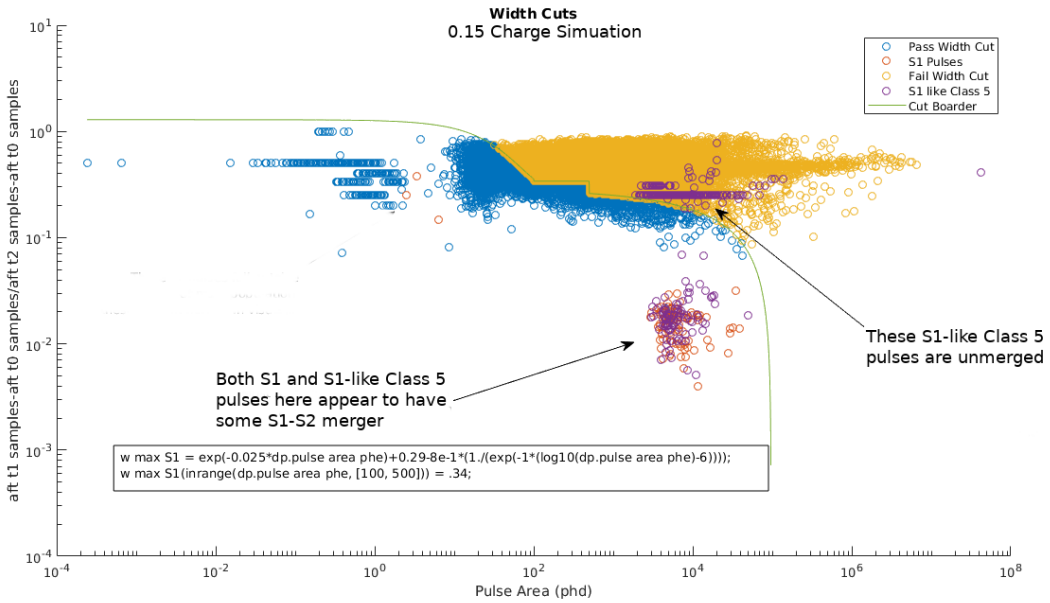

Figure 3.8: The above figure shows the width cut parameter vs pulse area, where the width cut has been applied to the S1 pulse classification, here seen in regard to $0.15e$ charge simulation. Specifically, pulse timing width cut is the difference between the time at which the pulse has achieved 50% of its pulse area, called $t1$, minus the time at which it achieved 1% pulse area, called $t0$, divided by the difference between the time of achieving 99% pulse area, called $t2$, and the aforementioned 1% timing, i.e. $(t1 - t0)/(t2 - t0)$. Blue circles indicate a pulse which passes the width cut, the yellow circles indicate those which fail the cut, and the red and purple circles denote S1 and S1-like Class 5 pulses, respectively, regardless of whether or not they fail the cut. The green line shows the border of the cut, defined by the displayed equations. Interestingly, as indicated on the figure are two populations: one in the upper portion where S1-like Class 5 pulses fail this cut, where the pulses are unmerged; the second population in the lower portion with classified S1 and S1-like Class 5 pulses show pulses which actually have an S1-S2 merger.

merged S1 pulse and what is actually a merged S1-S2 pulse in both the pulse timing width cut space and the boxcar cut space. The different populations could receive either S1 or S1-like Class 5 designations. For instance, in figure 3.5 on page 72, showing the boxcar cut, the upper grouping of classified S1 and S1-like pulses appear in actuality to be merged S1-S2 pulses. In contrast, the second grouping lower in the boxcar plot shows S1-like Class 5 pulses, which although passing that cut fail other requirements to be classified as S1 pulses, and are all unmerged. Furthermore, in figure 3.8 on the preceding page, which shows the pulse area width cut, in the upper portion where S1-like Class 5 pulses fail this cut, pulses are unmerged. In contrast, the second population in the lower portion of the width cut figure shows classified S1 and S1-like Class 5 pulses which actually have an S1-S2 merger. Completely classifying an S1-S2 merger as strictly an S1 or S1-like Class 5 pulse has the consequence of overstating the total reconstructed energy of the pulse because the gain factor for an S1 is larger than that of an S2. However, although causing some efficiency loss, the issue of merged S1-S2 pulses does not severely impact the LIP search. The study of merged S1-S2 classification has been a subject that has interested the LUX Collaboration and hopefully the information in the figures for the boxcar and width cuts will prove useful to the entire collaboration as well as for LZ.

For a pulse to be classified as an S2 pulse, it needs to meet boxcar, top-bottom asymmetry, and prompt fraction requirements which are not conceptually very different than those detailed regarding S1 pulses. They differ only in that the cut boundaries remain slightly different, and that the prompt fraction cut for S2 uses the prompt fraction RQ which starts at the 1% pulse area time point instead of the prompt fraction tlx RQ which starts at the 10% pulse area time point. For the exact equations, one should refer to the programming code itself. Furthermore, for an S2 pulse to be classified as such, it needs to have a pulse area of greater than 33 phd as well as have a maximum amplitude greater than 1 phd/sample.

Single detected photon pulses and single electron S2 pulses meet all requirements for S1 and S2 pulses, respectively, but fail in one specified requirement. Single detected photons meet the various requirements for S1 with the exception of the two-fold coincidence. If the pulse has merely

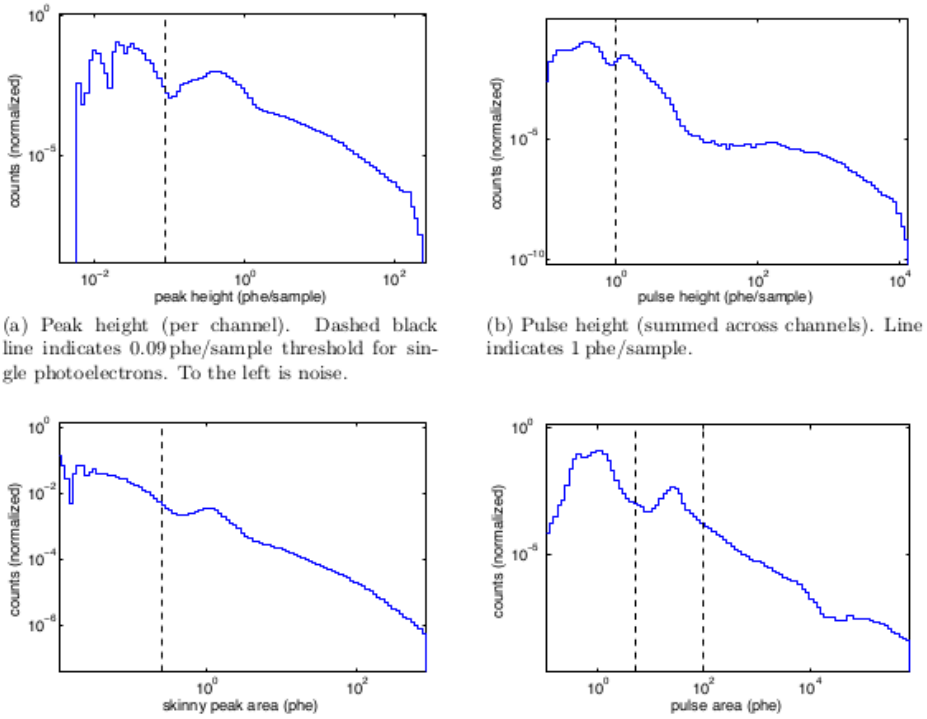

(a) Peak height (per channel). Dashed black line indicates 0.09 phe/sample threshold for single photoelectrons. To the left is noise.

(b) Pulse height (summed across channels). Line indicates 1 phe/sample.

(c) Skinny peak area is the sum of the peak (by channel) within a 50 ns window. Dashed black line indicates 0.25 phe.

(d) Pulse area (summed across channels). Dashed black lines bound the single e^- S2.

Figure 3.9: In addition to following the previously mentioned multi-parameter space requirements for S1 pulses detailed in plots 3.5, 3.6, 3.7, and 3.8, an S1 pulse needs to have two-fold coincidence of PMT channels with peak area greater than 0.25 phd, as seen in plot (a), and peak height surpassing 0.09 phd/sample, as seen in (c). A pulse having only 1 PMT channel meeting the aforementioned requirements on S1 pulses, receives single detected photon classification (Class 3). For an S2 pulse to be classified as such, it must meet the criteria mentioned in the previous section and have maximum pulse height of a least 1 phd/sample, as seen in plot (b), and pulse area of greater than 33 phd, as seen in plot (d). Note that the plot in (d) indicates a cutoff of 100 phd, but this was reduced to 33 phd in the Run03 reanalysis. A pulse meeting all criteria of being an S2 but having a pulse area between 5 and 33 phd with two-fold PMT coincidence would receive single electron S2 classification (Class 4). The plots above come from the lux10_20130820T0753_cp03854 dataset rq file and reprinted from [86].

a one-fold coincidence, such that it has a pulse area greater than 0.25 phd as well as a pulse height greater than 0.09 phd/sample but does so in only in a single PMT channel, then it receives SDP classification (Class 3). In parallel to the single detected photon, the single electron S2 pulse meets all qualifications for S2 pulses except the pulse area requirement. A single electron must instead have a pulse area between 5 and 33 phd. The threshold of 33 phd might appear odd given that this has been set to equal 1.5 times the area of a single electron extracted from the liquid under WIMP search conditions. However, the 33 phd requirement separating S2 pulses from single electrons assures that an event does not receive a multi-scatter characterization, which would eliminate it from the WIMP search filter parameters, due to the presence of noise from a single electron S2 with upward energy fluctuation [86].

Note that the requirement that the pulse must have a maximum amplitude of greater than 1 phd/sample remains for single electron pulses, and it also must have a two-fold PMT coincidence. Thus, a pulse meeting S2 requirements but having an area between 5 and 33 phd receives the classification of single electron S2 (Class 4). Figure 3.9 details the secondary requirements of S1 and S2 pulses regarding channel height, pulse height, channel pulse area, and summed pulse area. Finally, if there remains a pulse that has pulse area but does not fulfill any of the other requirements placed upon pulses, then it would receive an $else$ classification (Class 5). Thus, any pulse with an area would receive some form of classification.

3.2.4 Event Delineation

Most of the remaining modules in the DPF have a wider scope encompassing the event, not simply the individual pulses within the event. The module called S1S2Pairing_Naive determines if S2 pulses in the event pair to an S1. Specifically, the S1-S2 pairing module finds all of the S2 pulses, then finds the S1 pulses in the event, and pairs all of the S2s to an S1. In the event of multiple S1s in the event, the first S1 becomes the one used for pairing. The module calculates drift time for the S2s, taking the timing of the S1 as the start of the drift period for the electrons which will generate the S2 pulse. All S2 pulses within the event occur quickly enough that their start timing could be assumed as simultaneous. The drift time has been assumed to maintain a constant

pace throughout the detector and has an established rate previously determined via calibrations. See section 2.3 for more information regarding calibrations which have determined an electron drift of 1.51 $\pm$ 0.01 mm/μs. The linear mapping of electron drift to distance remains only an approximation because the electric field varies throughout the drift region, often as the result of charge build-up on the PTFE walls of the detector. One of the benefits of using the dual-phase xenon TPC is the ability to determine the three-dimensional position of the S2 pulses within the detector, and the S1-S2 pairing module calculates the z position of pulses within an event.

The Event_Classification module follows S1-S2 pairing, when the entire event receives classification as a 'golden' event based upon the WIMP golden event requirements, or if the event contains multiple scatters. A 'golden' event for the WIMP search contains a single S1 and a single S2. The event classification module did not serve a particular purpose in the LIP search, but nonetheless, the module remained in the modified DPF used in the search.

3.2.5 Position Reconstruction

PositionReconstruction_MercuryI, simply known as Mercury, uses the top PMT array information in order to determine the x and y position of the pulses within the event. The Mercury program, initially developed for use in the ZEPLIN-III detector [87], overcomes significant obstacles to position reconstruction near the detector walls. A center of mass type calculation would improperly reconstruct wall events closer to the center, and light reflected from the PTFE walls towards the center of the detector can also skew the reconstruction of wall events. Reconstructing wall events has critical importance in determining the fiducial volume for xenon self-shielding calculations.

The Mercury program operates by calculating Light Response Functions (LRFs) for each PMT. The LRF is a function based upon the distance between the true pulse location and the PMT that has detected light. The LRF method has an advantage in that it requires only live data to determine the interaction position, rather than also requiring proper simulations [55]. LRFs were calculated through an iteratively improving process using data from ^{83m}Kr calibrations, with each new ^{83m}Kr injection being used to improve the calculation [55]. The most likely position is determined for

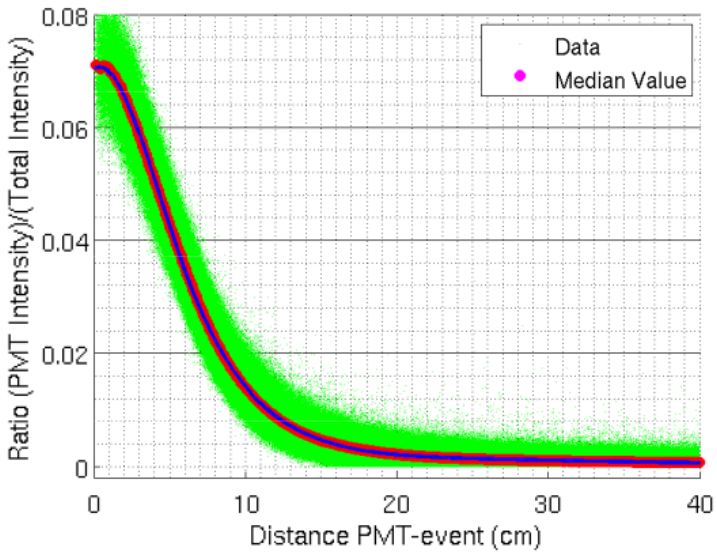

Figure 3.10: This figure shows an example of a Light Response Function (LRF) for a single PMT in the LUX detector. Iterative calculations determine the LRF response by comparing its calculation to krypton calibrations. The DPF uses the LRF to calculate the positions of events in the detector with the Mercury program. Figure reprinted from [86].

pulses greater than 1,000 phd via χ^2 minimization and for pulses less than 1,000 phd via a maximum likelihood approach, with their difference being negligible at such size [86]. The LRF used in LUX $\mathcal{H}_i$ is given by [55]

$$\mathcal{H}_i = \mathcal{A}_T \mathcal{C}_i \left[\eta\left(\rho\right) + \varepsilon_i\left(r, \rho\right)\right] \tag{3.1}$$

where $\mathcal{A}_T$ is the total event pulse area, and $\mathcal{C}_i$ is a coefficient which normalizes the response of each PMT. The above equation for $\mathcal{H}_i$ consists of a radially symmetric function η and a polar component ε_i with dependencies upon position of the light emission ρ, as well as the distance between the event and the center of the PMT r. Figure 3.10 shows an example of an LRF for a single PMT in the LUX detector.

3.2.6 Corrections Modules

The original results for positions from Mercury still require corrections in order to determine the final position of the pulse. Usually, corrections become necessary as a result of non-uniformity in the drift field which could come from charge buildup on the PTFE. Charge buildup resulted in a

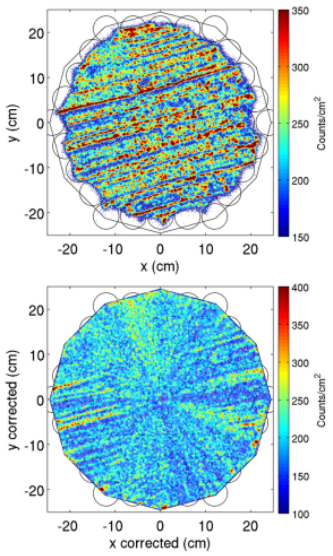

Figure 3.11: The top figure shows the uncorrected x-y position reconstructions of an acquisition of ^{83m}Kr events with a z-drift time between 200 and 300 μs. The bottom figure shows the same events with corrected x-y positions. Note that the uncorrected positions have greater reconstruction near the grid wires, that the position correction module has rectified. Figure reprinted from [55].

radial component correction, which in Run03 had a relatively small contribution compared to the prodigious effect it had on Run04. The Corrections_PositionCorrection module calculates those corrections for S2 pulses only, but see section 3.3 on page 84 on how the modified DPF expanded the ability of this module to also calculate corrected positions for SE and S2-like Class 5 pulses.

When ^{83m}Kr was used in calibrations (see section 2.3.2 on page 54), the injected krypton filled the entire detector with a uniform distribution of events, which allowed it to create a map of reconstructed x-y positions observed versus real or expected positions within the distribution. In creating the correction matrix applied to the data, the detector was cut into 30 μs slices in drift time and 60 segments in polar angle. The result is 600 uniform radial bins with an average radius within the bin used to calculate the radial corrections [55].

The position correction module itself applies a z position correction initially in 5 μs bins and thereby adjusts the resulting drift time. After correcting the drift time, an S2 correction map is applied within 2 cm^2 bins [86]. The module then interpolates the drift time correction between the krypton injections performed both before and after the data acquisition of the event in order

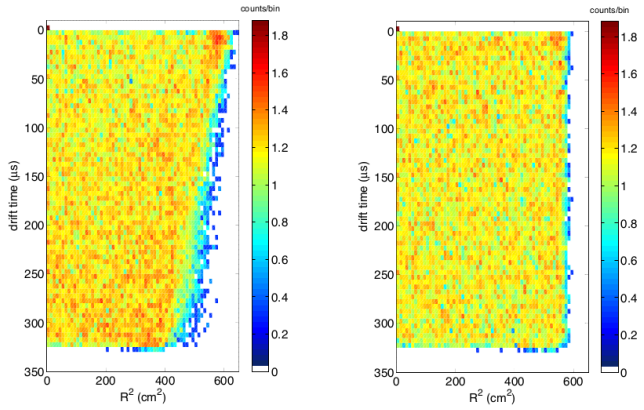

Figure 3.12: These figures show the R^2 vs z-drift time for events within a ^{83m}Kr injection acquisition during Run03. The left figure indicates the uncorrected positions, and the right figure shows the results following correction for the radial electric field. Radial field effects remained small in Run03, but became more pronounced in Run04. Figure reprinted from [86].

to normalize each bin. See figure 3.11 for an example of an event distribution of a z-slice before and after applying the position correction module. As is apparent in the aforementioned figure, the uncorrected positions have a greater tendency to resolve near the grid wires, which the position correction module has rectified. Figure 3.12 shows the effects of the position correction module which corrected for the radial electric field. Although the effect of non-uniformity within the electric field on position reconstruction remained small in Run03, the effect became more pronounced in Run04 when the PTFE walls accumulated greater charge. Run03 had a radial component driven by the electrical transparency of the cathode grid and lateral field rings [55]. If a corrected position could be calculated, it was saved in the corresponding RQ, however, there were a number of different error codes if the module failed to reconstruct a corrected position (see table 3.2).

Error Code	Meaning
-100	No uncorrected position calculated
-200	Reconstructed outside of detector
-300	Pulse is either before the S1 or beyond 32,000 samples after the S1
-400	Pulse has no associated S1
-500	Not classified as S2 (nor SE, S2-like Class5 in modified DPF)

Table 3.2: Possible error codes resulting after position correction in the DPF.

Field non-uniformity also slightly affects pulse area corrections, and is accounted for by the pulse area correction module, known as Corrections_ApplyCorrections. The need for pulse area corrections comes from field effects on positions which, in turn, affect the pulse area corrections having a position-dependent component. The energies are corrected by application of a position-dependent matrix, calculated from a comparison between known energies of ^{83m}Kr decays with observations from ^{83m}Kr injections. If light and charge yields retained the same dependence on the electric field as would WIMPs and other particles, such corrections would have been unnecessary, however, light and charge yields at low energies have a diminished dependence on electric field [55]. While the systematic uncertainty of S1 signals remained less than 2% anywhere in the detector, S2 signals had a 4% systematic uncertainty in the center of the detector [55].

3.2.7 Final Modules

Following the corrections modules, the DPF included an additional timing module called PulseQuantities_TimeSince which simply determined the time, in samples, since there had been an event with a total event area greater than various thresholds. Knowing the frequency of various large area events could provide clues to the formation of electron trains and other electron backgrounds that follow larger events (see section 4.4.1 on page 115 for more information).

Lastly, PulseQuantities_WaterPmtRQs calculated information for the water PMTs in the veto tank. Although some files in Run03 did have water PMT information, generally water PMT information did not exist in Run03. Water PMT information remained excluded from the LIP analysis, although the veto might be of interest to a Run04 based LIP analysis in the future.

Following the various analysis modules, the DPF then generated versions of the final RQ files in formats other than the binary RQ form. The three forms that had been generated from Run03 were HDF5, ROOT, and Matlab. Matlab was the primary version of the converter used for the LIP analysis, with the associated module called AdditionalFileFormat_SaveMatFile.

3.3 Modifications to the Data Processing Framework

The LIP search required various modifications to the Data Processing Framework, most of which were implemented in an $ex\ post\ facto$ post-processing fashion. LIPs of higher charge could be expected to have so numerous a quantity of interactions with the xenon that the PMTs would be unable to resolve them as individual pulses. Instead, the DPF would observe the interaction as a single long pulse or a handful of long pulses throughout the length of the detector, a notion confirmed from simulated LIP waveforms (see section 4.3 on page 109) and observed in muon events. The DPF would normally treat these long pulses as single interactions and record only a single position for the interaction as opposed to a track. Additionally, these long pulses would often include a merged S1-S2 signal. Figure 3.13 has a through-going muon in the xenon space of the detector and illustrates a merged S1-S2 as well as an instance where all S2s within the pulse have merged together. A merged S1-S2 has further implications because the required multiplicative factors, g_1 and g_2, of detected S1 and S2 signals to convert detected photon quantities into energy units differ greatly. Therefore, a merged S1-S2 pulse would elude proper energy reconstruction of the event. To compensate for the possibility of there being a single or several long pulses indicating continuous ionization within the event, modification of the analysis software allows the DPF to $chop$ the event into segments.

3.3.1 Select Reprocessing

The LIP search implemented the $chop$ mechanism for real data given that the search already had the 100 pulse rq files and evt files for all events. This process selectively targets events with long pulses and reprocesses specific modules following $chopping$ of the event, and has been termed Select ReProcessing (SRP). First, after having determined results from the Transparent Rubiks Cube Pulse Finder module, an event with a pulse longer than 4,000 became an initial candidate for $chopping$. A secondary criterion was implemented to exclude many of the long baseline shifts that often appear in the LUX data as a very long pulse. A candidate for SRP thus was required to have some structure to it, specifically, that the pulse amplitude surpassed 4 phd/sample average within

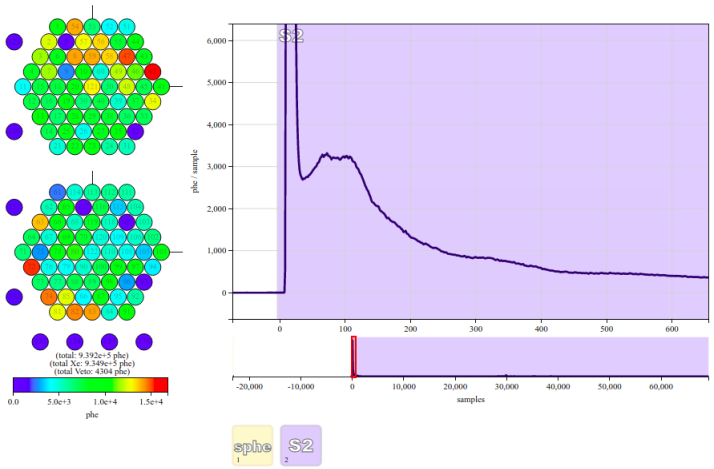

Figure 3.13: The above is a waveform of a through-going muon in the xenon space of the LUX detector. Viewed in Visualux, the top figure shows a zoomed version of the front of the waveform. As the figure shows, the S1 became merged with the S2 of the muon and did not return to baseline in order to allow the pulse finding program within the DPF to separate these pulses. The smaller bottom figure shows the full extent of the length of the muon event where no discrete pulses occur and only one pulse discerned from the waveform. The entire event receives classification as a single S2 pulse. Pulse *chopping* would remove the S1 and separate the merged S2 into S2 segments such that the DPF could calculate corrected positions and energies. This event has LUXstamp 14813847842755081 and was initially found by Douglas Tiedt during Run04.

a 50-sample box near two out of three of the following: the middle of the pulse, two-thirds the length of the pulse, or 500 samples from the end of the pulse. These three aforementioned points are taken from the pulse length timing in the instance that the targeted long pulse has a length of fewer than 32,000 samples; the 32,000 mark is the maximum drift time in the detector under Run03 conditions, which is the physical extent of the detector beyond which residual ionization could be coming from various sources but not from the direct path of the incident particle. In the event that the pulse length measures beyond the 32,000-sample limit, SRP imposes the pulse limit as 32,000 samples from the start of the pulse. The 50-sample box used for the average can exist in any continuous block within ± 100 samples of the aforementioned three points. SRP thus can remove many of the background baseline shifts, although certainly not all, while retaining previously found through-going muon events.

Once a candidate event had been determined, the *chopping* code finds what it considers to

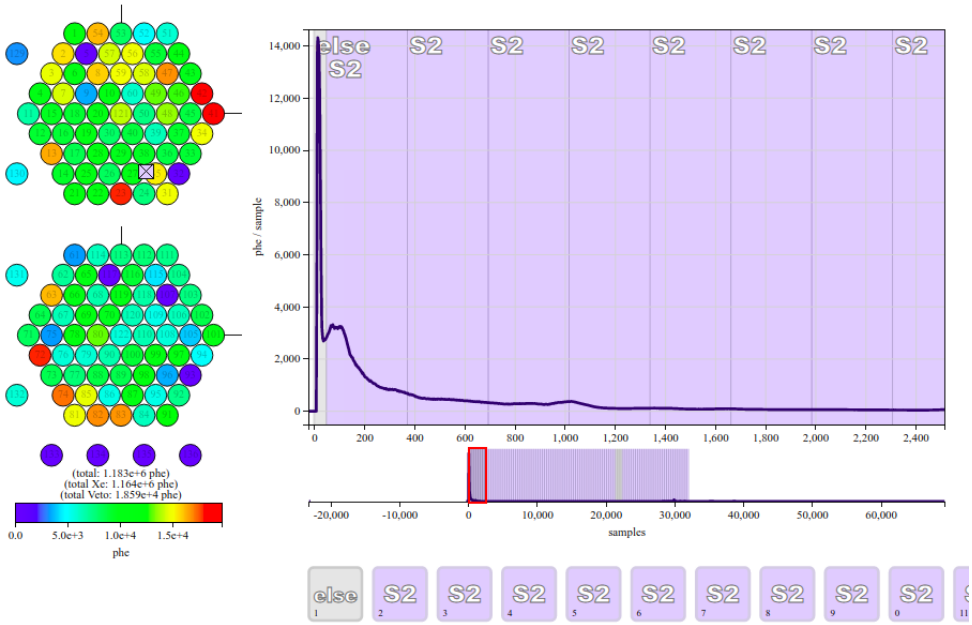

Figure 3.14: Long tracks with closely spaced impacts appear as a single waveform filling the entire detector or of several long waveforms. The above figure shows the first several thousand samples of the waveform of the same event depicted in figure 3.13 on the preceding page. The waveform, which subtends the detector and has residual noise signal following past 32,000 samples, has been *chopped* into segments within the physical extent of the detector. When an event contains a pulse of at least 4,000 samples, if that waveform has a height of 4 phd/sample in two of either the middle of the long pulse, its two-thirds point, or 500 samples from the end, then the event undergoes the *chopping* program. When *chopping*, the first large pulse of the event is located, 50 samples of timing following its start become the S1, and the 31,950 samples remaining from the imposed length of the event are divided into 99 equal segments. Also, note that this example includes an S1 (first pulse here) which had been classified as an *else* pulse which would have caused the original data processing framework to ignore this event, but with the new modifications, corrected energies and positions for pulses have been calculated.

be the beginning of the track. It should be mentioned that the beginning of the track does not necessarily mean that the track begins with the beginning of the long pulse. An S1, or a shorter-length merged S1-S2 pulse may in fact precede the long pulse, as a distinct entity. At this point, the SRP code finds the first pulse with a large pulse area, having 1,000 phd minimum, as calculated in the original rq file. The 1,000 phd minimum requirement might sound excessive, but recall that the SRP looks for pulses coming from higher charge LIPs, whereas low-charge LIPs should not be merged and their S1s would be amongst the standard 100 pulse rq files.

Once the first large pulse has been determined, it becomes designated as the start of the track. At that time, the old pulse start and end times become replaced with the newly-imposed start and end times. The first 50 samples of the first large pulse define the first pulse in the event. SRP then extends out to 32,000 samples from the beginning of the track and equally divides the remaining 31,950 samples into 99 equal parts. The separation of the first 50 samples creates what will become the S1, empirically determined based upon usual S1 timing, then the equal divisions of the remaining pulse timing along the length of the TPC create a track of S2 pulses. Thus, the entire physical extent of the detector has been $chopped$ and the start and end times have been replaced. See figure 3.14 for an example of a $chopped$ muon, which is the same event as the merged example figure 3.13 on page 85. Figure 4.10 on page 111 in section 4.3 shows an example of a simulated LIP at $0.15e$ that has been $chopped$. Note that in some instances, where a break in the contiguous pulse area occurs, no pulse area occurs within the imposed start and stop times of the 99 pulse divisions. Such a pulse with zero pulse area does not affect the other pulses in the event; the DPF assigns it a pulse classification of 0, and the rest of the DPF carries zeros for the other RQ values of that particular pulse.

After SRP has finished $chopping$ the pulse via its start and end times, it creates new evt (as .evt.mat file), cvt, and rq files which contain only information about the pulses which have been $chopped$. The new files receive the same name as their predecessors with a '_chop' designation appended before the file type designation (i.e. lux10_20130423T2231_f000001_cp26962_chop.rq). Thus, the original acquisition, file number, and cp number remain the same. The rq file receives an additional RQ called 'chopped_flag' that exists as a simple Boolean flag and serves to indicate if $chopping$ has been done to the event. The analysis software then uses the resulting timing along the TPC length from the $chopped$ pulses to generate uncorrected and corrected pulse areas with their corresponding reconstructed positions.

3.3.2 Corrected Energies and Positions

S1 signals from LIP simulations often had qualities that fail several of the established norms for an S1, as mentioned in section 3.2.3 on page 71, and become classified as an unknown classifi-

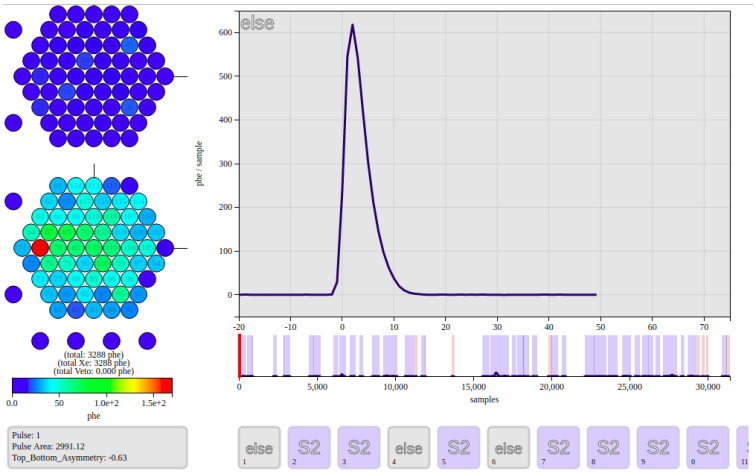

Figure 3.15: The main figure shown here presents an S1 pulse that the pulse classification module had incorrectly classified as Class 5, also known as $else$ type pulse. It did not receive S1 classification because it failed both the top-bottom asymmetry and timing-width requirements (see section 3.2.3 on page 71). Extensions to the DPF give this pulse the additional classification of S1-like Class 5 that the modified DPF can treat as an S1 for the purposes of S1-S2 pairing, as well as correcting positions and pulse areas. A pulse receives the S1-like Class 5 designation when there are no other S1 pulses present in the event. The example pulse comes from a $0.1e$ charge LIP simulation directed through the center of the detector. Also of note, the classification of the first 10 pulses within the corresponding event, seen at the bottom of this figure, show S2 pulses also misclassified as $else$ pulses. See figure 3.16 for an additional example and details on S2-like Class 5 pulses.

cation, denoted as Class 5 and referred to as an $else$ pulse (see section 4.3 on page 109). Therefore, further modification to the data processing framework treated a leading $else$ pulse as equivalent to a true S1 in the instance that the DPF did not detect any other S1 for the purposes of drift time calculation and correction of final positions and energies of subsequent pulses. The $else$ pulse in question would not need to be the first pulse in the event, but the $else$ pulse could not have been preceded by an S2 pulse. Similarly, LIP signals could often result in very small pulses along the track, thus, single electrons and $else$ pulses after the start of the pulse were treated as S2 pulses and given a corrected position and energy. Note that the observation of these types of S1 and S2 pulses originally given $else$ classification occurred regardless of whether or not the event containing those pulses had undergone $chopping$.

In order to give the $else$ pulses their needed treatment as S1 and S2 pulses, the definitions of

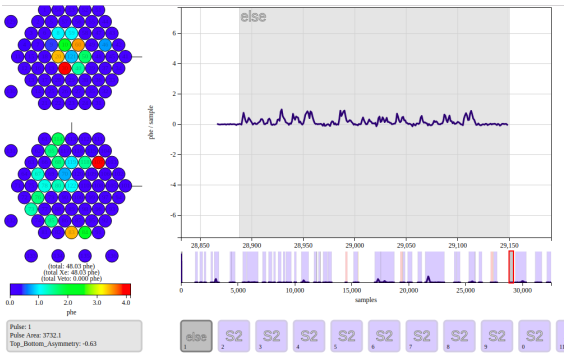

Figure 3.16: The main figure shown here presents an S2 pulse that the pulse classification module had incorrectly classified as Class 5, also known as $else$ type pulse. As noted in simulations like this example of a 0.1e charge LIP directed through the center of the detector, there are times that the software noted little interaction with the xenon such that the detected photons were more spread out than a typical single electron but smaller than a typical S2, and the pulse classification module classified it as a Class 5 / $else$ pulse. As seen in the smaller, bottom graph which shows the entire length of the pulse, this particular pulse appears to be part of the ionization trail of the LIP. To counteract the problem of valid ionization receiving $else$ type classification, the modified DPF gives the additional classification of S2-like Class 5 to any $else$ pulse where at least one Class 2 / S2 pulse has preceded it in the event. The modified DPF incorporates S2-like Class 5 pulses into the corrections for energies and positions, and also calculates the aforementioned corrections for those pulses.

S1 and S2 pulses were not modified, but instead, the modified DPF created two new RQs called 's1_like_class5' and 's2_like_class5' for relevant $else$ pulses. The two new RQs exist as Boolean arrays, having an entry for each possible pulse in the event, which was 100 in the LIP analysis. An S1-like Class 5 pulse is an $else$ pulse within an event when (a) there is not a true S1 and (b) at least one true S2, as determined by the pulse classification module, follows the $else$ pulse. An example of an S1 which had been misclassified as a Class 5 / $else$ pulse, and then given the additional new classification of S1-like Class 5 appears in figure 3.15. In the instance that two or more pulses within an event meet these criteria, the largest among them gets the s1_like_class5 flag and the rest remain simple $else$ pulses. An S2-like Class 5 is defined as an $else$ pulse which follows a true S2 pulse, as determined by the pulse classification module, and the raw pulse area has summed to greater than 10 phd. Many pulses within an event may receive an s2_like_class5 flag. An example of an S2-like Class 5 pulse can be seen in figure 3.16.

Once all pulses or pulse segments from $chopping$, as the case may be, within events have received pulse classification and the $else$ pulses given their additional classification, if needed, the SRP code calculated the new S1-S2 timing. For the S1-S2 timing in SRP, the code has been modified to include pairing the S1 or S1-like Class 5 pulse to S2, S2-like Class 5, or single electron pulses. Corrected positions and corrected energies of pulses, that the DPF would only create for pulses designated as having S1-S2 pairing, were then calculated for the aforementioned pulse types. All S2s within an event become part of the calculation for corrected positions and energies, therefore including S1-like Class 5, S2-like Class 5, or single electron pulses in the correction calculations proved critical. In this fashion, the software could calculate the corrected energies and positions of LIP-like events.

Furthermore, the notion of creation of s1_like_class5 and s2_like_class5, and the inclusion of single electrons was also applied to all live $non-chopped$ data with 100 pulses. Similar code was created to handle the new RQs, S1-S2 pairing, and corrections for all events, working in the same manner described above. However, for the $non-chopped$ data these corrections were applied as the data was being loaded for the LIP filter analysis (see section 4.4.2 on page 121).

In order to allow the Matlab binary file-loading program to properly load a file with a single event, a final fix was required. Specifically, instances with a single event, for unknown reasons, become transposed in their matrix orientations when compared to files with multiple events. Of course, properly loading files and events remains very important in trying to carry out mathematical operations on those events. The fix for the transpose loading problem simply re-transposes matrices of events when the file had only a single event. The file 'LUXLoadRQ1s_framework.m' was the particular file modified. One might consider files having a single event to be a rarity, however, selection of events for $chopping$ via the SRP code often resulted in the DPF processing a single event from evt to rq. Although usually SRP selected multiple events within the acquisition for $chopping$, a given acquisition consisted of several hundred evt files, which in their un-selected or unmodified state often have hundreds of events each. The re-transposition of events occurs at the event loading-level and not whilst running the individual modules. Some of the programmers who

created individual modules within the DPF had been aware of an issue where Matlab transposes single events, and $some$, but unfortunately not all, modules had fixes for the problem. However, when the global fix to the event loading program alleviated the transposition problem everywhere, it became necessary to individually remove the local fixes from various modules. Nonetheless, the modified DPF could handle $chopping$ a single event and process it from evt to rq.

4. SIMULATION AND DATA ANALYSIS

Although a LIP search came as a secondary focus of the LUX experiment, data from the experiment can be used to discern a LIP signal. Unlike the WIMP signal, an anticipated LIP signal will not have a single energy deposition throughout the detector, but would instead appear somewhat similar to a muon. The LIP would have an effective fractional charge $e \cdot f$ where e is the electron charge and $f < 1$. Such a signal from a LIP would leave a track of energy depositions throughout the volume of the liquid xenon. In general, the track signal should appear generally muon-like with energy loss in xenon proportional to f^2, just like other charged particles [32].

Recent LIP searches such as the Cryogenic Dark Matter Search (CDMS) II take advantage of the track-like nature of the energy depositions by requiring depositions in various layers of the stacked puck detectors that make up the experiment [40]. LUX does not include stacked detectors but instead constitutes a single detector volume. However, LUX records data beyond the duration of a single S2 pulse within an event, thereby allowing the detection of multiple energy depositions in succession along the depth of the TPC. In looking for tracks, a LIP search would not need to exclude data in the perimeter of the detector because simultaneous background generation in both the perimeter of the detector and in the fiducial volume of the WIMP search region remains unlikely to form a pattern mistakenly attributed as from a track. Therefore, a LIP search could take advantage of the full liquid xenon volume, where there exists a sufficiently strong electric field to facilitate electron extraction. Direct searches remain particularly important when looking at models involving LIPs because some theories suggest that energetic cosmic rays may produce such particles with masses greater than those accessible to collider experiments, with an energy-loss profile not heavily influenced by particle mass [39] [88].

The 90-day LUX dark matter run, Run03, amassed sufficient data to perform a LIP search. The longer Run04 LUX dark matter run lasted 332 days and had varying electric fields due to charge accumulation on the detector walls, making the process of track reconstruction much more complicated; such a search shall be left for future endeavors.

4.1 LIP Search Assumptions

When searching for a LIP signal in the LUX detector, several assumptions on LIP characteristics must be taken into account; these assumptions form the basis to determine if the LIP would be visible to the detector. These assumptions include those related to LIP generation, momentum, and angular distribution.

LIPs have been assumed to be cosmogenically produced. Regarding relic LIPs with a long lifetime, as opposed to cosmogenically produced LIPs in the upper atmosphere, the particles would have been carried outside of the galactic disk by the galactic magnetic field lines or supernova shock waves [89]. Therefore, the search cannot depend upon the existence of relic LIPs because of the infinitesimal likelihood of terrestrial observation. Furthermore, assuming cosmogenic production also leads to the presumption that a terrestrial detector will have superior detection capability when compared to collider-based searches. Detector searches gain superiority because if LIPs become produced during high energy collisions in the upper atmosphere, these collisions could create LIPs with greater masses or energies than the those accessible to current collider technology [90].

Muons have been observed within the LUX TPC, despite traveling through heavy rock overburden, having lost significant energy to the rock, and possibly having been deflected by the rock. So too, must it be assumed that LIPs will have characteristics consistent with muons such that the they can survive traversing the large rock overburden of the mine. Thus, in order to survive the trip to the cavern it remains possible to conceive of LIPs having mass equal to or greater than the muon, or that its initial energy had been relativistic [40]. Nonetheless, as the LIP search has been carried out, LIPs have been assumed to strike the detector with minimum ionizing momentum, that is the LIPs strike the detector with the least energy loss possible as they traverse the detector. The minimum ionizing approach remains a conservative one, because a particle traveling slower or faster than minimum ionizing would lose more energy per track length of the detector. Figure 4.1 shows the stopping power, or energy loss, calculation for a positive muon in copper, which shows how faster or slower particles would lose greater energy. The Bethe equation describes the mean rate of energy loss of a charged particle through matter, also known as the mass stopping power,

given in MeV g^{-1} cm^2 by [32]

$$\left\langle -\frac{dE}{dx} \right\rangle = Kz^2 \frac{Z}{A} \frac{1}{\beta^2} \left[\frac{1}{2} \ln \frac{2m_e c^2 \beta^2 \gamma^2 W_{max}}{I^2} - \beta^2 - \frac{\delta(\beta\gamma)}{2} \right] \tag{4.1}$$

with K referring to the constant with value $4\pi N_A r_e^2 m_e c^2 = 0.307$ MeV mol^{-1} cm^2. Note that equation 4.1 remains valid for the range indicated in figure 4.1 where $0.1 < \beta\gamma < 1000$. The value W_{max}, the maximum energy delivered in a single collision, has the value

$$W_{max} = \frac{2m_e c^2 \beta^2 \gamma^2}{1 + 2\gamma m_e/M + (m_e/M)^2} \tag{4.2}$$

In the above equations m_e refers to the electron mass, c the speed of light in a vacuum ($m_e c^2$ = 0.5110 MeV), M the incident particle mass in MeV/c^2, N_A Avogadro's number, z the charge number of incident particle, Z the atomic number of the absorber, A the atomic mass of the absorber, I the mean excitation energy in eV, r_e the electron radius 2.817 fm, and β and γ having their relativistic values. The term $\delta(\beta\gamma)$ indicates the density effect correction to ionization energy loss. Minimum ionizing has been assumed to be defined as $\beta\gamma \approx 3$ [32] [40] [91]. Note that the linear stopping power would have the mean of $\langle -dE/dx \rangle$ ρ in MeV/cm, with ρ being the density in g/cm [32]. It stands to reason that a particle which loses more energy in the detector than minimum ionizing would therefore have an increased probability of detection and the result of the LIP search would have greater efficiencies than those calculated considering only minimum ionizing energy loss.

Furthermore, regarding the notion that LIPs may deflect during travel through the rock overburden, it shall be presumed that the deflection does not occur or has been insignificant enough to avoid deviation from an isotropic from above distribution [40] [91]. Additionally, given that a potential source of LIPs could come from the collision of cosmic rays with the atmosphere, the analysis should assume that LIP production does not occur inside the Earth, and therefore no tracks from LIPs should move up toward the atmosphere. Indeed, as mentioned in section 4.4 on page 114, the track identification program remained agnostic as to whether the projected LIP track

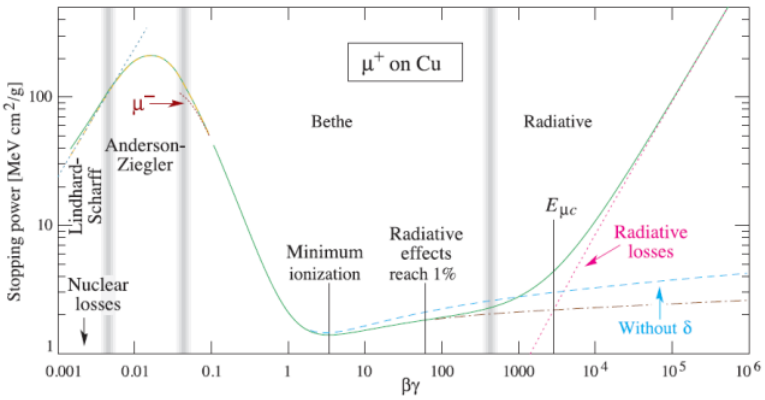

Figure 4.1: This figure shows the stopping power $\langle -\frac{dE}{dx} \rangle$ of μ^+ muon particles in copper as a function of momentum $\beta\gamma = p/Mc$. Note that where the stopping power finds its absolute minimum $\beta\gamma \approx 3$ [40]. Particles with greater or less momentum than the minimum ionizing momentum would lose more energy per track length. The same principles hold true for the case of stopping power in xenon. Figure reprinted from [32].

entered the detector from the top or the bottom. Also, the analysis assumes a downward moving LIP because the mechanics of the TPC cannot distinguish between an upward and downward moving LIP. Other studies have made the downward moving LIP assumption as well, either out of convention or, like LUX, because of detector mechanics [40] [91]. The distribution of incident LIPs has therefore been assumed as isotropic in the upper 2π with no events below it.

Finally, LIP flux should remain low enough that LUX could observe only a single LIP at a time. If the LIP flux had a rate high enough for coincident LIPs to hit the detector, the resulting model would become more complicated. Furthermore, if such a large LIP flux existed, previous explorations studying LIPs would have likely seen them [40].

4.2 Previous Work

Several previous studies into a range of LIP charges have been undertaken. Typically in particle physics there exist three main avenues to experimentation: production, where a particle accelerator attempts to create a theoretical particle, indirect direction, which looks for the effects or decay by-products of a theoretical particle; or direct detection, where a theoretical particle may scatter or interact with a detector medium. This section will briefly overview studies looking specif-

ically for LIPs using production and indirect detection, giving more emphasis on direct detection experiments. The production and indirect studies have focused mainly on theoretical models with a charge-mass dependence, often referring to the theoretical charged particles as Fractionally Charged Particles (FCPs) or Fractionally CHarged MAssive Particles (FCHAMPs). Note that by contrast, the LIP direct detection experiments, such as the LUX LIP study, remain mass independent. Many of the experiments under discussion are summarized in figure 4.2 on page 99. Many details regarding these searches are summarized elsewhere [40] [45].

4.2.1 Accelerator Searches

Particle accelerators provide a means for detecting particles by accelerating known and generally stable particles to a very high velocity, which then collide into a target or other particles. Particles with a mass less than that of the energy of the system may then be generated as a result of this collision. Then any particle generated would be detected either directly or via its decay products, or the particle would be noted as the loss of momentum from the system without other cause. The last of these methods would notice the creation of a relatively long-lived but non-interacting particle, which could occur in the WIMP case, for instance. The sensitivity of such experiments rests with the limited probability of generating the particles. Detection probability for LIPs decreases quadratically with the particle charge from the reduction of the resulting electromagnetic interaction cross-section [40].

A number of accelerator searches have taken place with the aim of producing unbound quark states. They include the PEP experiment which had a limit of mass $\mu > 14$ GeV for electron charge range $\epsilon \cdot e$ of $0.2 \leq \epsilon \leq 0.8$, and also KEK TRISTAN having produced a limit of $\mu > 26$ GeV with charge $\epsilon = 2/3$ [92]. The Anomalous Single Photon (ASP) experiment carried out at Stanford Linear Accelerator Complex (SLAC) looked for unexplained single photons indicating new weakly interacting particles, specifically using an electron-positron annihilation into a photon and the new particle. In the case of a massive charged paraphoton from an additional $U(1)$, the ASP experiment excluded charges in the range $0.08e$ - $0.20e$ with corresponding masses of 1 - 13 GeV [92]. A search for new charged particles occurred using the 1991-93 OPAL data from the

Large Electron-Positron collider, which excluded such particles of with $\epsilon \geq 2/3$ with mass $m < 84$ GeV [40] [93]. Recent work has been done to extend the OPAL result to $\epsilon < 0.24$ and $m > 45$ GeV [94].

New charged particles have been sought using data from the Large Hadron Collider (LHC) looking at proton-proton collisions. Such particles should leave a faint track in the muon chamber of the LHC. The Compact Muon Solenoid detector had sought particles with $\pm 2/3$ and $\pm 1/3$ of the electron charge, and excluded candidates with masses less than 310 GeV and 140 GeV for the respective charges [95]. It remains likely that the increased collision strength which shall be analyzed from the High Luminosity LHC could provide even stricter constraints.

Collider-based beam-dump experiments provide an additional experimental avenue where particles accelerate in order to make an impact upon a fixed target. When the particles impact the target, they produce secondary particles which then travel towards the detector, which has shielding to exclude unwanted secondary particles from the search. One such experiment dedicated to the search for millicharged particles, aptly named the Millicharge Collaboration, occurred at SLAC. This SLAC-based experiment used a scintillation counter to detect the possible ionization occurring from new charged particles resulting from a 29.5 GeV electron beam incident upon a tungsten target. The result from the Millicharge Collaboration search excluded particles of mass 10^{-7} to 10^{2} MeV with charges $10^{-2}e$ to $10^{-5}e$ [45]. Furthermore, the Millicharge Collaboration also published a 95% confidence upper limit on particles having charge $4.1 \cdot 10^{-5}e$ with a mass of 1 MeV as well as charge $5.8 \cdot 10^{-4}e$ particles with a mass of 100 MeV [96]. A different beam dump experiment housed at SLAC, this one with the intention of detecting neutrino-like particles has been reanalyzed looking for trident production where an electron and neutrino interaction could give rise to an additional new charged particle with its anti-matter partner. The results of the trident analysis exclude particles of charges $3 \cdot 10^{-4}e$ and $3 \cdot 10^{-2}e$ for masses less than 200 keV and less than 1 GeV, respectively [45] [92]. Unlike the previously mentioned beam-dump searches, the next experiment for discussion, called E613 at Fermilab, was a proton-based experiment. The E613 experiment excluded charges between $0.1e$ and $0.01e$ for masses less than 200 MeV. It remains

important to note that although these collider-based experiments constrain the mass-charge range, they do not restrict massless charged particles.

4.2.2 Indirect Detection Searches

Indirect searches such as observations of stellar phenomena or searches indicating the presence of new charged particles can serve to help further constrain the theoretical possibilities for charged particles. Although such indirect effects do not have the same gravitas as constraints from laboratory-based experiments, the indirect measurements can provide a glimpse into the world of new charged particle physics.

Processes inside of stars could lead to the creation of new particles, and if new particle mass remains low they could escape the star, carrying with them some of the star mass. Assuming the case without a hidden-sector photon, a fractionally charged particle could decay into an electron-positron pair in the case with mass greater than 1 MeV, the rest mass of an electron-positron pair. In such a case, from solar observations it has been previously shown that the rate of fractionally charged particle creation would not surpass their annihilation within a star if particle charge remained less than $10^{-3}e$ [97]. Similarly, if new charged particles do not become trapped within the sun, then the estimated production rate of such particles has been considered negligible for the charge range $10^{-10}e$ to $10^{-3}e$ with masses less than 1 keV [97]. In the case where the new particle has a mass less than an electron, the new charged particle and its anti-partner would annihilate into photons, however, the corresponding limit on the charge would be only less than $2 \cdot 10^{-9}e$ [92]. Observations of plasmon decay in white dwarf stars, supernova SN 1987A, and constraints from BBN all also place limits on new particles with very small charge [45].

In the case of widely distributed mini-charged neutrinos as a relic of the expansion of the universe, CMB photons would have acquired a thermal electric mass, which would manifest as a long-range violation of Gauss's Law. Experimental tests of Gauss's Law limit the thermal electric mass to less than 10^{-25} GeV, imposing a bound of less than $10^{-12}e$ with a neutrino mass less than 10 keV [98]. Similarly, neutrino electric millicharge bounds have been placed as less than $1.5 \cdot 10^{-12}e$ using the limit placed on the neutrino anomalous magnetic moment by the Germanium

Experiment for measurement of Magnetic Moment of Antineutrino (GEMMA) experiment [99]. The GEMMA experiment sought to determine the neutrino anomalous magnetic moment from measurements of antineutrino-electron scattering in their reactor. The extraordinary breadth which LIP searches explore is evident from the wide range of theoretical possibilities that could give rise to LIPs of some form.

Limits on new charged particle physics can come from ortho-positronium decay studies. Positronium refers to the bound state of a positron and an electron, and ortho-positronium refers to positronium in the triplet state $^3S_1$ with parallel spins. Ortho-positronium has the longest decay time of positronium states making it preferred for study and a new physics search would focus on positronium to invisible decays where the branching ratio exceeds that accounted for by the decay from positronium to a neutrino-antineutrino pair. An experiment testing for new physics beyond the Standard Model has ruled out particles less massive than the electron with charge $\leq 3.4 \cdot 10^{-5}$ of the electron charge [100].

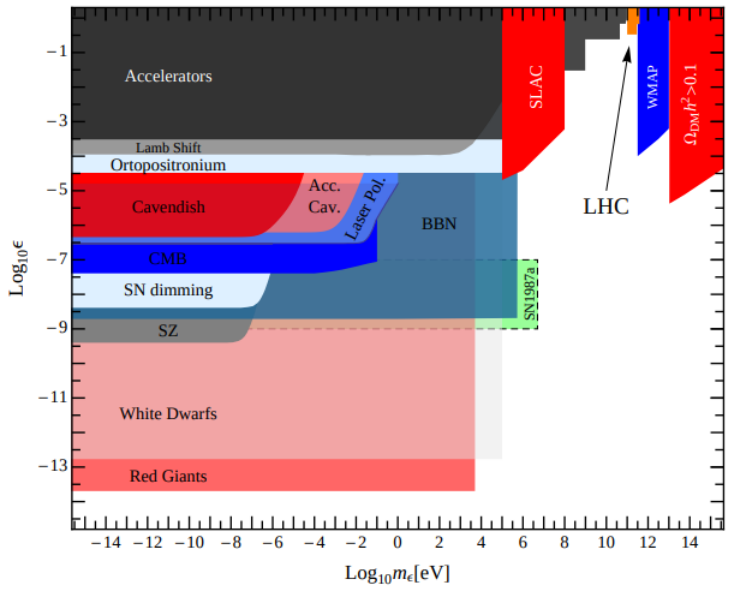

Figure 4.2: The combined results of various experiments and observations of physical phenomena which place limits on the mass m_ϵ and charge $\epsilon \cdot e$ space for various theories of LIPs or fractionally charged particles. Although many of the searches are summarized in this section, there remain more details and additional searches listed in other works [40] [45]. Figure reprinted from [101].

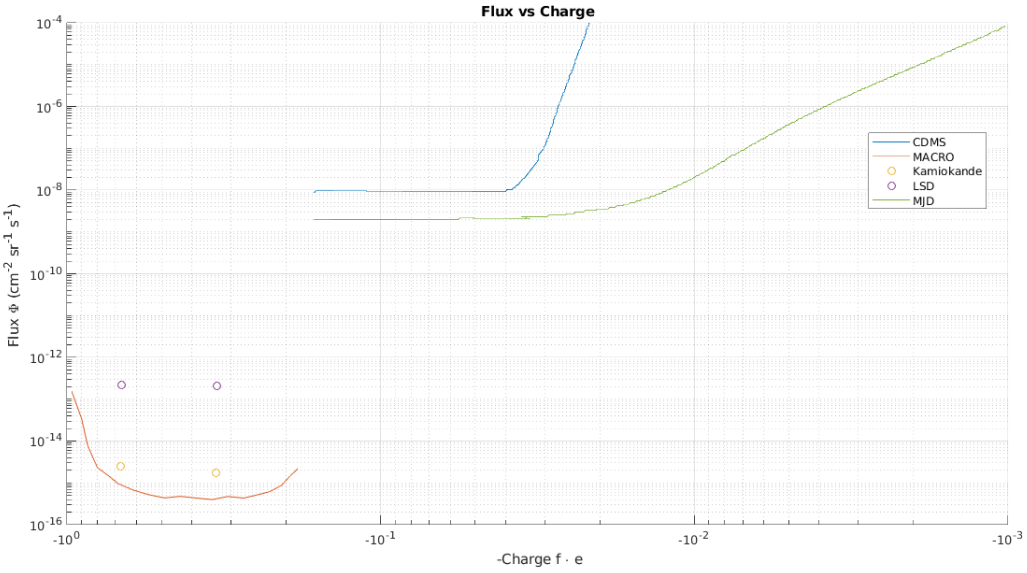

Figure 4.3: Flux Φ vs -Charge $f \cdot e$, where $f < 1$ and e is the electron charge. The figure summarizes previous LIP mass-independent flux limit from data adapted from [39] [88] [90] [91] [102].

Indeed, there remain several studies looking at the notions of new charged particles. These studies include Milken-type and Cavendish-like experiments, vacuum dichroism and birefringence, and optical experiments [40] [45] [101]. Although of interest from the standpoint of new physics in general and non-massless charged particles specifically, their form and nature become increasingly distant from the study presented in the LUX LIP search detailed in this work which focuses on mass-independent particles with a charge greater than or equal to $0.01e$. Many of the indirect searches have summarized results in the mass-charge space shown in figure 4.2 on the preceding page. The following section shall relate to previous work similar in form and function to the results from the LUX LIP search.

4.2.3 Direct Detection Searches

Five different experiments before LUX have explored the LIP parameter space in a mass-independent fashion. The experiments Kamiokande II and Liquid Scintillation Detector (LSD) both specifically looked at the charges $e/3$ and $2e/3$, whereas the Cryogenic Dark Matter Search

(CDMS) II, MaJorana Demonstrator (MJD), and the Monopole, Astrophysics, and Cosmic Ray Observatory (MACRO) have produced a continuous distribution of charge exclusion. These five experiments set their limits looking at the LIP flux Φ as a function of charge factor f, where the particle has charge $f \cdot e$ and e is the electron charge (see figure 4.3). LIP flux, denoted Φ, has the following calculation [91]:

$$\Phi = \frac{N}{\epsilon \Omega A t} \tag{4.3}$$

where N is the theoretical number of observed LIPs at a given charge, ϵ is the simulation efficiency at the same charge, Ω represents the solid angle of the detector, A the cross-sectional area of the detector, and t indicates the livetime. Flux calculated in this manner has units cm^{-2} s^{-1} sr^{-1}. The nature of the LUX LIP study is comparable to these previous studies which also focused on using terrestrial detectors that seek to detect LIPs produced cosmogenically, usually assuming that the LIP came from cosmic ray interaction with the atmosphere [90].

The LSD experiment occurred at the Mont Blanc Laboratory in Europe at a slant depth of 5,000 hg/cm^2 of standard rock. The primary science run of the detector focused on the observation of neutrinos, however, its scientific team has applied its data to various other searches such as a LIP search and a monopole search. The LSD FCP/LIP search focused on searching for particles with $\pm 2e/3$ and $\pm e/3$, with these charges being known to exist as SM particles in the form quarks. The detector itself consisted of a modular array of 72 independent volumes measuring $1 \times 1 \times 1.5$ m^3 arranged in three layers, having a total mass of 90 tons of C_nH_{2n+2} liquid scintillator ($\langle n \rangle \sim 10$) (see figure 4.4) [88]. The energy resolution appears to have been much less sensitive than LUX, with an energy deposition in a scintillator volume of 1 MeV that would result in light output of only 15 phd. Although each event required three-fold coincidence, each volume within the detector had only three PMTs. Iron, lead, and borax paraffin[1] shielded the entire detector from local background γ particles and neutrons [103].

For the LIP result, LSD reanalyzed all recorded muon events from December 1985 to Febru-

[1]LSD papers appear to refer to this substance under various similar names; reference [88] spells this as borex parafine, reference [103] as Boro parafine or parafine with Boron, and reference [104] as borex paraffin.

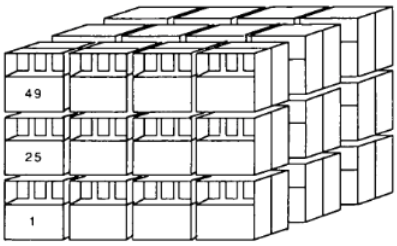

Figure 4.4: The LSD experiment consisted of 72 tanks of scintillator divided into 24 vertical columns. Their LIP search required coincident signal in all three layers of a single column. Drawing reprinted from [88].

ary 1993, and in order to simplify the geometry, limited its search to only those events contained within a single one of the 24 vertical columns of the detector. Due to the fact that the readout of the three tanks comprising one vertical column each had a separate energy readout, it allowed LSD to obtain three independent measurements of the energy loss for a candidate particle. LSD studied muon energy losses and tracks from each column with observed events employing a Monte Carlo calculator. They then determined the maximum and minimum observable energy losses of the muon having either the longest or shortest track length in the detector. Energies below the calculated thresholds would then be considered as tracks possibly coming from a particle with a charge less than a muon. Out of 5,674 events, four satisfied their criteria for a fractionally charged particle. Further consideration and simulation of muon events passing through two of the three layers with a coincident γ occurring in the third have been proposed as an explanation for the signals observed. Their final flux limits were found to be $\Phi(Q = \pm 1/3) \leq 2.3 \cdot 10^{-13}$ cm^{-2} s^{-1} sr^{-1} and $\Phi(Q = \pm 2/3) \leq 2.7 \cdot 10^{-13}$ cm^{-2} s^{-1} sr^{-1} [88]. Applying the same analysis to the entire detector found 40 candidates surviving cuts, with 5 and 19 of them being consistent with $\pm 1/3$ and $\pm 2/3$ respectively. The associated flux limits have values of $\Phi(Q = \pm 1/3) \leq 1.5 \cdot 10^{-13}$ cm^{-2} s^{-1} sr^{-1} and $\Phi(Q = \pm 2/3) \leq 3.8 \cdot 10^{-13}$ cm^{-2} s^{-1} sr^{-1} [88]. The results from LSD have interesting candidate particles, however, the candidates might be the result more well-known backgrounds. The competitive limit on flux largely comes from the large size of the detectors and the long data collection period.

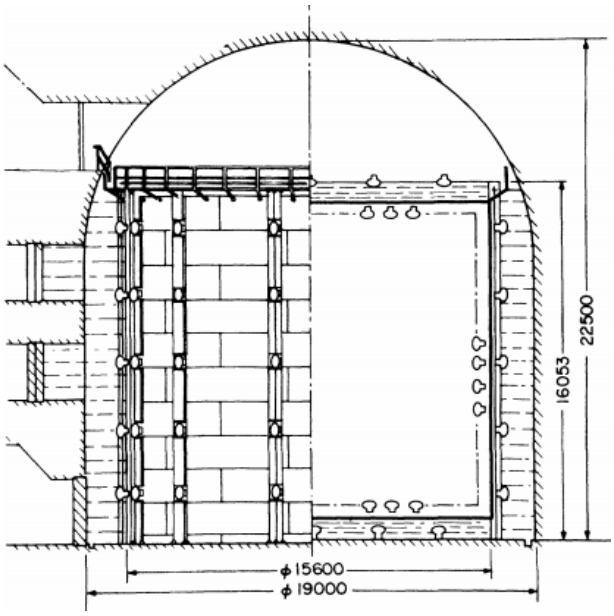

Figure 4.5: Schematic drawing of the Kamiokande II detector. The water anti-counter indicated by the dashed area surrounded the cylindrical inner detector. Overall dimensions listed in mm. Drawing reprinted from [105].

The Kamiokande II experiment consisted of a water Cherenkov detector designed for neutrino observation and located 2,700 mwe underground in the Kamioka mine in Japan [105]. The detector contained 2,140 tons of water in a cylindrical steel tank measuring 14.4 m diameter by 13.1 m height and using 948 20-in PMTs to form the inner detector. A water anti-counter 1.2 m thick viewed by 123 20-in PMTs surrounded the inner detector. Figure 4.5 has a schematic drawing of Kamiokande II.

For its LIP search, Kamiokande II analyzed $7.1 \cdot 10^7$ events during its data taking period of December 1986 to April 1990 and accumulated 1009 live days of data [102]. The search focused on $\pm e/3$ and $\pm 2e/3$ particles by exploiting the square proportional relationship to energy deposition in a given path length, having already established $E \approx 1000 \cdot L$ phd, L being the path length. The analysis placed cuts on total energy detected, and then removed all events with short (< 10 m) path length or those events which had PMT energy signatures indicative of a particle which stopped within the detector. LIPs were simulated by multiplying muon-simulation waveforms by the cor-

responding inverse square charge[2]. Following the simulations, they made cuts by comparing the candidate pulse height with the calculated reduced pulse height. Any remaining events were then visually scanned individually whereby they determined that no candidates remained. Selection efficiencies were determined to be 76% and 71% for the $\pm e/3$ and $\pm 2e/3$ particles respectively. The search determined the nominal detection area of 130 m^2, and assumed a 4π angular acceptance. The resulting flux values were found to be $2.1 \cdot 10^{-15}$ cm^{-2} s^{-1} sr^{-1} for $\pm e/3$ particles and $2.3 \cdot 10^{-15}$ cm^{-2} s^{-1} sr^{-1} for $\pm 2e/3$ [102]. At the $e/3$ and $2e/3$ charges the Kamiokande II LIP limit remains impressive and occurs as a result the large size of the detector.

The MACRO experiment was a very large underground scintillator originally designed to detect magnetic monopoles located in the Laboratori Nazionali del Gran Sasso in Italy [106]. The structure consisted of a modular form divided into six $12.6 \times 12 \times 9.3$ m^3 super-module sections with an overall length of 76.5 m. The detector had an overall mass of $\sim$5,300 tonnes with a spacial view space covering an isotropic area of $\sim$10,000 m^2 sr, making it an extremely large detector compared to LUX. Each super-module consisted of 77 scintillation counters divided into three vertical planes and two horizontal planes. Its lower section had 10 horizontal streamer tube planes, and its vertical sides contained six planes of streamer tubes in groups of three. The upper portion had four horizontal planes of streamer tubes in two groups separated by scintillation counter planes, and two side walls with streamer tubes and scintillation planes. The detector made use of a layer of crushed rock to screen and absorb incoming muons. See figure 4.6 for pictures of the overall structure of MACRO as well as a cross-sectional drawing of the various systems in the detector.

The data from MACRO has since been reanalyzed for a number of searches including a WIMP search, an atmospheric neutrino search, and twice for LIP searches [39] [107]. The LIP trigger consisted of a combination of the streamer tube trigger coincident to the lowest energy threshold

[2]The method of multiplying the gain factors in order to get corresponding pulse heights had been considered during the early simulation stages of the LUX LIP search presented in this work. The method became discounted upon the realization that it would result in S2 pulses with less than the pulse area corresponding to a liberated single liquid electron. This method also appeared unable to properly indicate the diminished number and frequency of LIP interactions with the target media, as it theoretically remains the case that LIP interactions should occur less frequently than muons. The Kamiokande II LIP search must have devised a means to address the emergent problems of quantized pulse size and frequency of interaction, but perhaps these problems can be less relevant for higher-charge LIPs within such a large detector.

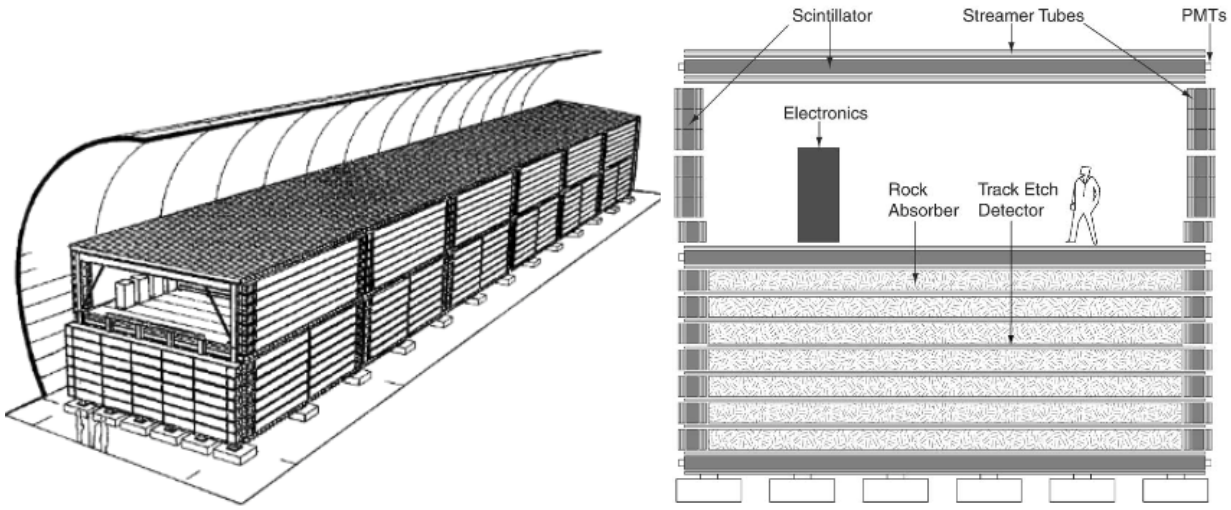

Figure 4.6: MACRO experiment structure consisted of a modular form divided into six 12.6 $\times$ 12 $\times$ 9.3 m^3 super-module sections with an overall length of 76.5 m. Each super-module consisted of sections of scintillation counters and streamer tubes. The left picture shows the overall structure of MACRO, whereas the right image shows the cross-sectional view of a super-module. Drawings adapted from [106].

scintillator trigger at 1.2 MeV. The search allowed for LIP velocities in the range β = 0.25 to 1.0. The trigger found $18.3 \cdot 10^6$ LIP triggers over the course of 1,320 live days within the time period between fall 1989 and December 2000. The streamer tube system in the MACRO super-modules allowed for three-dimensional reconstruction of the candidate particle path. Hits could not be in more than four scintillator faces and within six scintillator counters of the same face in order to exclude cosmic ray muons which had also made an electromagnetic shower. Track length had a required measurement between 13 and 70 cm, and tracks within 10 cm of the scintillator counter were also rejected. The geometrical cuts allowed for a 3,300 m^2 sr isotropic flux of particles. The final requirement placed restrictions on particle energy loss as a function of length traveled. A single event did pass the cut requirements, however, due to the relative timing of parts of the detector, the event was discounted as consistent with a downward traveling relativistic particle in the upper detector section coincident with two hits from a slowly moving upward traveling particle in the lower detector section. In the end, the final search had an integrated exposure of $3.8 \cdot 10^{15}$ cm^2 s sr yielding a 90% confidence level upper limit for minimum flux of $6.1 \cdot 10^{-16}$ cm $^{-2}$ s^{-1} sr^{-1} with

results in the range of e to $e/6$, but see note[3]. See figure 4.3 on page 100 for a detailed continuum of results MACRO results [39]. The impressive flux limit established by MACRO comes as a result of its high efficiency, very large detector size, and its livetime encompassing a six year period.

The CDMS II experiment, designed for a WIMP search, was located in the Soudan Underground Laboratory in Minnesota at a depth of 2,090 mwe [108]. The detector consisted of five towers stacked with various vertical configurations of six Ge and Si detector disks. Differing from other previously mentioned direct searches that used some form of liquid scintillator for ionization and light measurement, CDMS II made use of solid detector media which measured ionization and phonons. The entire array consisted of 19 Ge disks of approximately 240 g each and 11 Si disks of approximately 110 g each. The disks had a cylindrical form, 7.6 cm in diameter and approximately 1 cm in height. A cartoon diagram in figure 4.7 shows the CDMS II layout indicating the different Ge and Si configurations. The experiment made use of a liquid scintillator veto for tagging muons.

The CDMS II experiment reanalyzed its WIMP search data for the period from July 2007 to September 2008, using only the fully-functioning Towers 2 and 4 (see figure 4.7) to search for LIP tracks [40] [90]. Candidate events were required to have an energy deposition in each of the six disks within a single tower and no depositions simultaneously occurring in any other tower. CDMS placed requirements on energy deposition consistency[4] as the particle traversed the detector, and required a straight reconstructed track constrained by Degrees Of Freedom (DOF) such that $\chi^2/DOF < 2$. The Photo-Absorption Ionization (PAI) model served as the basis for the interaction cross-section and dictated particle straggling. The analysis disregarded particles that struck the veto panels with a muon-comparable energy deposition. Due to the fact that CDMS was a solid crystal-based detector, it made use of phonon vibrations and ionization which serve as the analog of the S1 (photon) and S2 (ionization) signals in LUX. An event having a phonon to

[3]The results published by MACRO have a slight contradiction. Their discussion in both their first [107] and last [39] papers state the lower charge limit as $e/5$ because the 1.2 MeV detector threshold would impose a limit of $e/5$. However, despite the stated limit of $e/5$, both MACRO LIP papers have graphs indicating a flux bound with a continuous charge range ending at $e/6$. Indeed, other searches have interpreted the MACRO result as including down to $e/6$ [40] [91].

[4]The CDMS II LIP search did mention a slight difficulty in the application of the energy consistency criterion because the towers were constructed of differing ratios of Si and Ge material. The search made sure to include the effect of the material features before completing the energy consistency check [40].

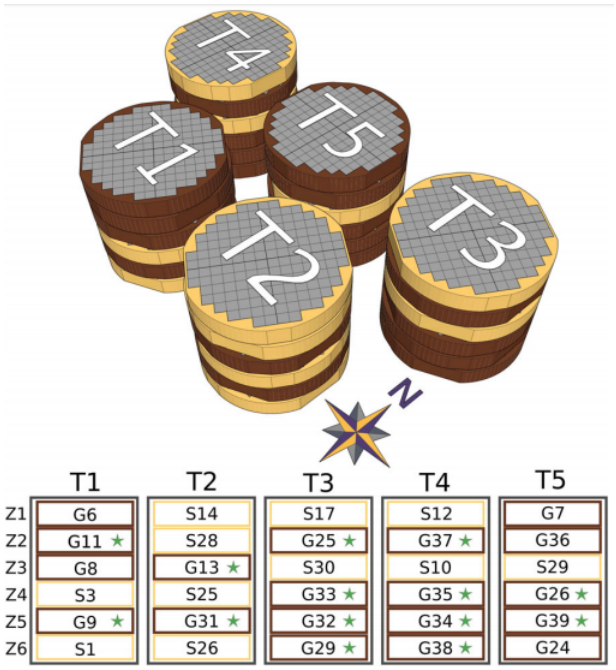

Figure 4.7: The CDMS II experiment consisted of five vertical towers stacked with Ge and Si disks. The detector had readouts for ionization as well as phonons. The distribution of Ge (brown) and Si (yellow) disks were as shown in the figure. Figure reprinted from [108].

ionization ratio which differed from the expected unity caused by electron recoils by 5σ was also disregarded. Two events passed the constrained six disk requirement, however, neither passed both the track linearity and energy consistency requirements. Additionally, they found three other events with an energy deposition that near the analysis threshold of one disk in the detector but otherwise satisfied all criteria for LIP events before the application of track linearity and energy consistency criteria. The final continuous limit was established with zero candidate events in the range $e/6$ to $e/200$ with a flux above $7 \cdot 10^{-9}$ cm^{-2} s^{-1} sr^{-1} (see figure 4.3 on page 100 for details) [90]. The CDMS search became the first LIP search focused on charges below $e/6$. It appears that the CDMS group has future prospects of a LIP search from their newer projects SuperCDMS and CDMSlite, but have decided to implement Geant4-based energy simulations rather than the previously used PAI model because the PAI model had under-represented the LIP total energy loss [109].

Lastly, the most recent LIP result to be discussed comes from the Majorana Demonstrator. MJD was originally built as a prototype detector meant to demonstrate the scientific concept for

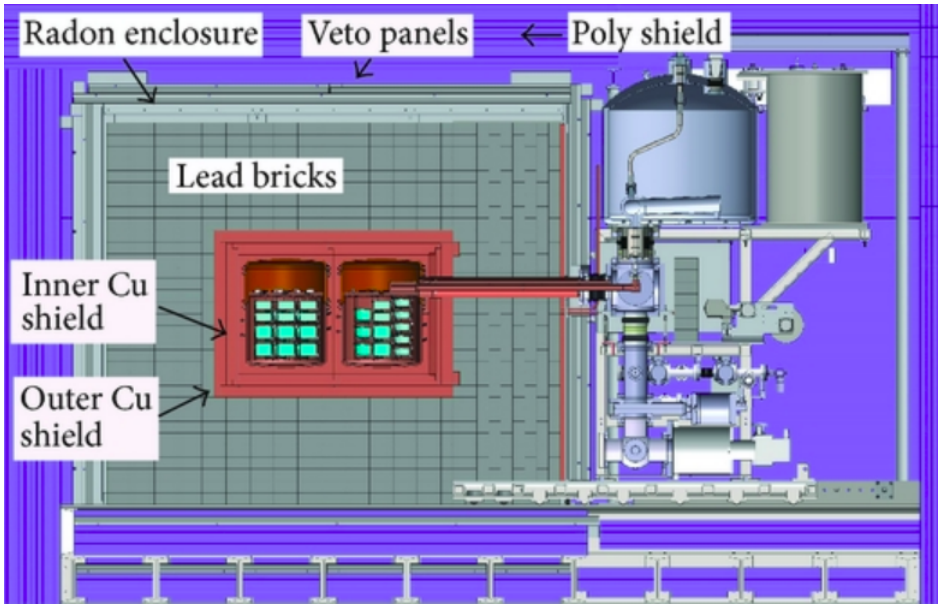

Figure 4.8: MJD experiment consisted of 44.1 kg solid Ge divided into 58 detector units installed in strings of three, four, or five units per string. The muon veto used in the experiment consisted of 32 panels of 2.54 cm plastic scintillator with PMT readout. Cartoon reprinted from [110].

a larger detector searching for evidence of neutrinoless double beta decay ($0\nu\beta\beta$). Observation of neutrinoless double beta decay would indicate that the neutrino acts as its own antiparticle, meaning that the neutrino is a Majorana fermion. The experiment also resides in the Homestake Mine at SURF, just down the hallway from LUX on the 4,850 level. The experiment itself consists of 44.1 kg Ge divided into 58 detector units installed in strings of three, four, or five units per string [91]. The detector units range in mass from 0.5 to 1 kg, have diameters in the range 6 to 8 cm, and have heights between 3 and 4 cm. It should be noted that the detectors in MJD have thicknesses three to five times those in the CDMS II experiment. The muon veto used in the experiment consisted of 32 panels of 1 inch plastic scintillator with PMT readout [110]. The setup of MJD had many similarities to that of CDMS II. See figure 4.8 for a cartoon of the basic detector setup.

The MJD LIP search included data from the period June 2015 to March 2017, with 285 live days of which 121 days used both modules, resulting in an exposure of 4993 kg days [91]. The end cap area of the smallest detector unit set the surface area equal to 30 - 37 $\pm$ 1 cm^2. MJD used the MaGe framework based upon Geant4 for particle simulation and made use of the same

PAI straggling calculation function as CDMS. The MJD search required between four and six detector strikes as a tracking requirement in order to eliminate various backgrounds. For each number of strikes, MJD calculated the solid angle for an isotropic from above (and as $\cos^2\theta$) distribution with the following values: 2.4 (1.5) sr, 1 (0.6) sr, and 0.06 (0.02) sr for the four, five, and six detector strikes, respectively. Furthermore, MJD required the muon veto to have a one second anti-coincidence time with the event in order to exclude cosmogenic backgrounds[5]. The experiment made use of track linearity requirements but lacked the ability to discern where within the detector unit the strike occurred and instead used the center of a detector unit as the position for a corresponding interaction. The search placed cuts on $\Delta\theta$ and $\Delta\phi$, informed from LIP simulations, and determined the final flux from the upper limit of the Feldman-Cousins 90% confidence level. The result had zero observed candidate events with a corresponding flux limit in the range $e/6$ to $e/30$ of $2 \cdot 10^{-9}$ cm^{-2} s^{-1} sr^{-1} with additional limit results detailed in figure 4.3 on page 100 going down to charges of $e/1000$ [91]. MJD produced the first flux limit in a charge range as low as $e/1000$.

4.3 Simulations

The LUX collaboration created a simulation suite called LUXSim [111] in order to predict detector response under particle interaction, based upon Geant4 particle simulation software [112]. Although LUXSim had been designed for use with Geant4.9.4.p04 or Geant4.9.5.p02, the latter was the edition of used for the LIP simulations. So as to give more accurate results for dual-phase detectors, instead of using Geant4 for light propagation models, LUXSim incorporates previously published measurements of liquid xenon responses at known electric fields called the Noble Element Simulation Technique (NEST) [113]. NEST gives the predicted light and charge released upon interaction with an incident particle, which LUXSim then calculates as the predicted detected photons within the detector PMTs. The ingenious notion behind NEST is that it does not require

[5]Normally, a detector energy deposition with coincident energy deposition in the veto would become an enhancement to the LIP search, however, due to the lower charged LIPs which the MJD search sought (less than $e/6$) and the high required energy threshold in the scintillator panels (1 MeV), a deposition in the panels had a reduced likelihood of originating from a LIP [91].

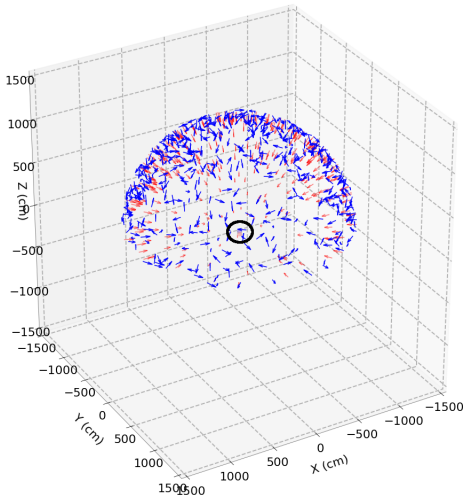

Figure 4.9: The figure shows the isotropic distribution surrounding the simulated LUX detector created by the modified MUSUN generator with the blue arrows indicating the initial positions and momenta, and the red arrows indicating the events which entered LUX. The black circle in the center highlights the position of the simulated detector. Figure generated from code made by K. Kamdin.

the computationally intensive tracking of individual photons but can still produce waveform output. The program LUXSim2evt[6] coverts the binary file output of the simulation into evt file format; the standard LUX collaboration data processing framework can treat the resulting evt file in the same fashion as live data. LIPs do not exist as a standard particle within the Geant4 framework. Nonetheless, extensions to Geant4 include a monopole class that allows for decimal electric and magnetic charge input. Muons can be simulated using a package called MUon Simulated UNderground (MUSUN) which takes information on muon straggling from a package called MUon SImulation Code (MUSIC) and deposits it in the detector using an isotropic from above distribution [114]. Both the MUSUN generator and the Geant4 monopole class required modification in order to use them for LIP simulation. Simulations were made in the charge range $0.01e$ to $0.1e$ in $0.01e$ steps, whereas higher charges up to $0.3e$ were carried out in $0.05e$ steps.

The Geant4 monopole was modified to allow incorporation into LUXSim, with the magnetic

[6]LUXSim2evt can be found in the tools folder of any LUXSim git repository.

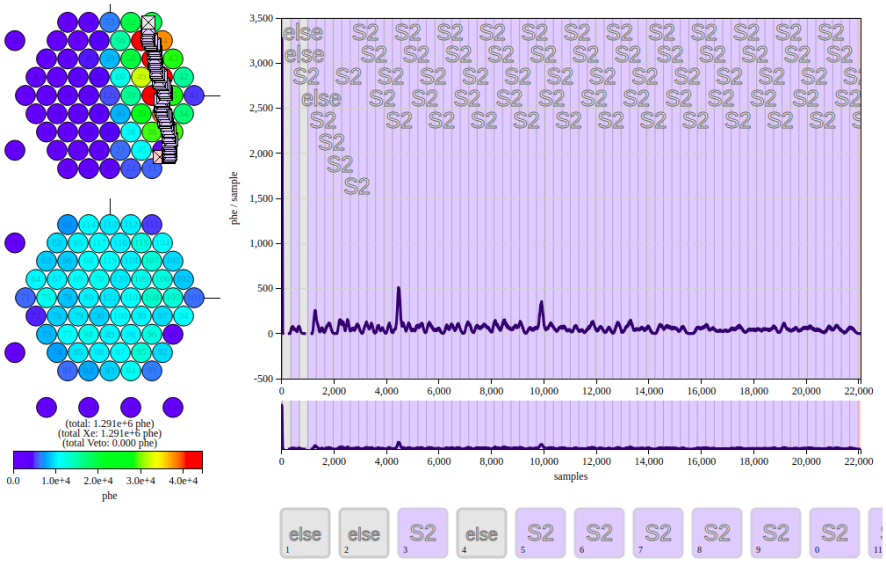

Figure 4.10: The above figure shows the waveform of a simulated LIP event at 0.15e charge. Normally, the entirety or majority of such an event would be merged and otherwise unusable, but the waveform has been *chopped* into segments to produce an easily recognized track which subtends the detector. Also note that the segregated portion which comprises the S1 received an *else* classification, thus in order for the event to be accepted, it necessitated the changes in section 3.3 on page 84.

charge set to zero and the electric charge set as the charge of the simulated LIP. LIPs are simulated in LUXSim via a two-step process. First, LUXSim generates the particle interaction as an energy-only simulation moving straight through the center of the detector, which would be detector path length limited, recording only positions and energies within the detector. Second, LUXSim is run again; this time, a modified version of the MUSUN generator uses the energy-only files as straggling inputs, which are used to generate light and charge along an isotropically generated track (see figure 4.9)[7]. Events with pulses more than 4,000 samples were *chopped* and processed then according to the methods mentioned in 3.3 on page 84. Both simulations of contiguous ionization tracks (see figure 4.10 for an example at $0.15e$) and tracks with discrete hits (see figure 4.11 for a 0.06e simulation) could be generated using the modified MUSUN generator in LUXSim.

A future endeavor could bypass the energy-only step within LUXSim, and instead, run the

[7]Those interested in reproducing any of these simulations could use the LUX git branches LUXSim_LIP and LUXSim_LIP-kk for the two runs of LUXSim, although creating a unified one should be possible.

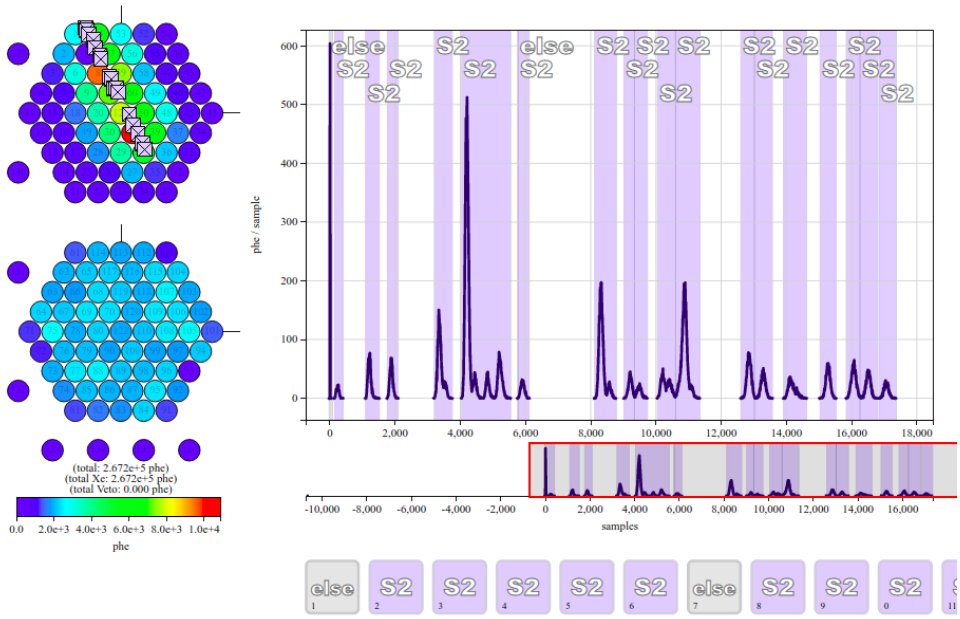

Figure 4.11: This figure shows a simulated LIP of charge $0.06e$; in this case, the event consists of many discrete pulses which have cut across the detector. Also, note that the S1 of the event received an $else$ classification. Normally an S1 misclassified as $else$ would be lost, however, use of the new s1_like_class5 RQ allowed for this event to receive corrected positions and energies (see section 3.3 on page 84). Also, note that the simulation includes a δ-ray at approximately 4,000 samples.

monopole through a Geant4-based simulation software of a block of liquid xenon to generate the energy-only tables for the modified MUSUN generator. Using a liquid xenon block of a length greater than the possible track length of a LIP traveling through LUX would prevent any issues with path length limitations, and this method would likely have a shorter computational run time than a method that activates and runs LUXSim the additional time.

Monopole simulation of electric charge within Geant4 has been confirmed to be consistent with the Bethe equation (see equation 4.1 on page 94) [115]. The monopole package in Geant4 also includes secondary electrons called δ-rays which appear as radial bursts from the main ionization path (see the simulated event in figure 4.11). Furthermore, it has been found that Geant4 calculation of total energy loss for fractionally charged particles remains consistent with the anticipated results published by the Particle Data Group (PDG) [32] [116], in contradistinction to results from other methods, such as PAI, which underestimate the loss [109]. Using the density of liquid xenon in

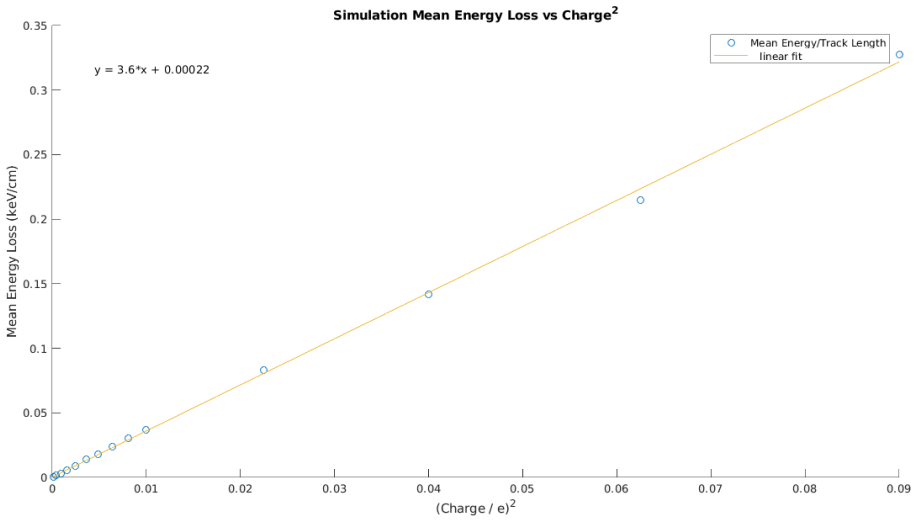

Figure 4.12: Average simulation energy per track length versus the square of the charge, whose slope of approximately 3.6 MeV/cm agrees with the expected proportionality to muon energy loss of 3.624 MeV/cm. The average simulation energy per track length has been calculated using the general g_1 along with the $g_{2,\ bottom}$ (see section 2.1.1) from the bottom PMT array, following quality and data analysis cuts.

LUXSim[8] of $\rho = 2.888$ g/cm^3 and the muon mean stopping power in liquid xenon $\langle -dE/dx \rangle_{min} = 1.255$ MeV cm^2/g [116], the mean energy loss being $\rho \cdot \langle -dE/dx \rangle_{min}$ results in an average muon energy at minimum ionizing $\langle E_{loss} \rangle = 3.624$ MeV per centimeter of track length. Given that the average loss of a charged particle has a proportionality to the square of the charge, simulations should have a linear slope of 3.624 in the average energy vs the squared charge parameter space. Figure 4.12 shows the average energy vs charge^2 for the simulated LIP events after analysis and quality cuts, having a slope of approximately 3.6, as expected.

The LUX collaboration does not have a means of properly simulating electron trains or electron bursts (see section 4.4.1 on page 115 for descriptions). A speculative approach to generating electron trains could be done in a similar fashion to LIP simulation methods discussed in this section. For instance, LUXSim-based code could receive modifications to reference a secondary file with various pre-calculated energy and z position spacing for the electron train. Then, modifying the MUSUN generator in a similar method as was used to generate the LIP tracks can place the

[8]See the file G4S1Light.cc in the LUXSim git repository for the density of liquid xenon used in LUXSim.

calculated energies alongside a simulated event following an S2 of requisite size. Simulating a second event consisting of merely an electron train following the initial electron train progenitor S2 in the previous event could remain more problematic. Simulation of an electron burst could also be possible in a fashion similar to the electron train; however, electron bursts tend to be events independent of a large S2 in the same event window and would, therefore, have challenges similar to simulating events with an electron train and no S2. Another, similar method would be to identify real electron trains and electron bursts, and add those waveforms to normal simulation events in a manner comparable to the method used for $salting$ in the Run04 WIMP search[9]. The musings and speculations included here are left as a future endeavor for LUX and LZ. Due to the fact that there was not a method of modeling the backgrounds for the LIP search, differences between the simulated data, as a substitute for a calibration source, and the real-time data have been used to develop an analysis method that would be able to identify a LIP signature.

4.4 Data Analysis

Traditionally, in an analysis such as the LIP search, the data has several values for RQs which are considered emblematic or characteristic of a theoretical phenomenon. The analysis makes cuts to the live dataset with the intention of separating signal from background. It is often the case that the characteristic RQs are well known and have calibration sources that could mimic the anticipated signal and backgrounds; however, this was not the case with much of the LIP search. The search did not have $e/3$ particle sources or other charges available to determine detector response, and many of the backgrounds deal with peculiarities of the detector and detector physics (see section 4.4.1 on the next page for information on backgrounds). Traditional cuts have been developed using LIP RQs by drawing cut lines which appear to separate background from simulation, with simulations used as a substitute for a known signal or calibration source (see section 4.4.2 on page 121). Furthermore, the LUX LIP search applies new machine learning based techniques as a means of separating signal from background (see section 4.4.3 on page 130), with a discussion regarding

[9] $Salting$ is the process by which events are added to the live datasets which have energies and positions consistent with expected WIMP-like events. $Salt$ events were created by joining S1 and S2 pulses from different calibration events. $Salting$ data prevents analysis bias, similar to the goal of a blind data analysis.

the outcomes from both the traditional cuts and the machine learning results (see section 4.4.4 on page 135).

The LIP analysis has been carried out on data from the 90-day Run03 dataset of the LUX detector and occurred in two stages. First, a test set of data was selected comprised of 14.6869 live days of data, taken between the dates 15 May 2013 and 31 May 2013 and consisting of 64 data acquisitions, where it was assumed that they contain only backgrounds. As mentioned, the LIP search considered the LIP simulation datasets as substitute for signal of actual LIP events occurring in LUX. The various cuts to both simulation and data were developed to screen out the background data from the test set whilst attempting to preserve as much of the simulation datasets as possible. The second step consisted of applying the cuts developed from the test set to the remainder of the reprocessed Run03 data, the last of which dated 1 September 2013, in order to determine if potential LIP candidates existed. Unfortunately, for unknown reasons, 62 WIMP search datasets (and less importantly an additional 10 CH_3T datasets) were never processed with 100 pulses. These most likely had an error in processing but were missed when those acquisitions which failed processing had their processing reinitialized. As a result, without the 100 pulse RQ files, there would not be a $chopping$ analysis done with SRP. The search did not use high-rate calibration data, such as several datasets following a large CH_3T injection, regardless of processing status, but did make use of those low-rate calibration acquisitions deemed usable for the WIMP analysis. A detailed list of which datasets had 100 pulse processing and SRP, and whether or not the acquisition was used as part of the LIP search can be found in appendix A on page 156.

4.4.1 Backgrounds

Several backgrounds potentially occur in the LUX data that could mimic a LIP signal, which must be excluded in order to reduce the probability of a false-positive result. These common backgrounds include muons, electron trains, other electron residual ionization, and baseline shifts. Later, aspects of background mitigation, which are found in the data analysis cuts in section 4.4.2 on page 121, have been designed so as to exclude many of these backgrounds. A LIP search in LUX must be able to address and screen all of these backgrounds.

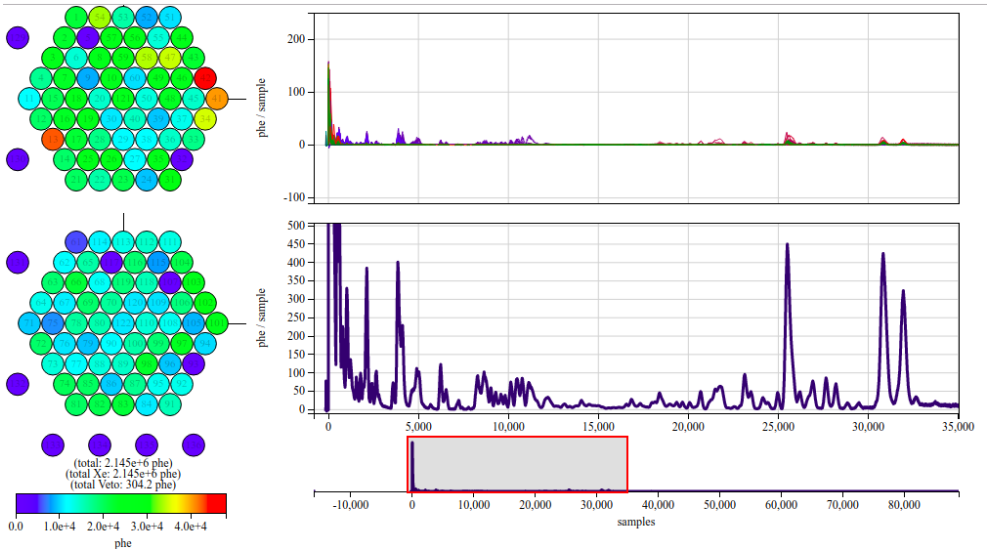

Figure 4.13: The above shows the Visualux plot of a through-going muon in the xenon space of the detector. Note the many peaks along the length of the muon track, some of which come from secondary electrons called δ-rays. δ-rays can project far from the track of the muon; the rays and large amounts of ionization make track reconstruction difficult in the DPF. This particular muon has LUXstamp 14904100486519380, originally found by Doug Tiedt in Run04.

Muons are one of the better understood and physically substantive backgrounds that occur within LUX. Although easily avoidable in the WIMP search, they become of great concern for the LIP search. Indeed, much of the software for pulse *chopping* had been tested upon known muons within the detector. However, even as a *chopped* pulse the segments that make up a muon have too greatly saturated the PMTs and the total light collected remains so great as to prevent proper position reconstruction. PMT saturation remains low enough in LIP simulations so as not to greatly affect position reconstruction. Figure 3.14 on page 86 and figure 4.13 show examples of through-going muons in the detector.

A common scenario occurs where a high energy particle strikes the detector and leaves residual ionization which the detector releases relatively slowly following the initial pulse. The trail of ionization could be in the same event window of the event, or the ionization could continue into several events following the initial high energy collision. The trail of ionization coming from the delayed release of individual electrons is commonly referred to as an electron train or $e - train$;

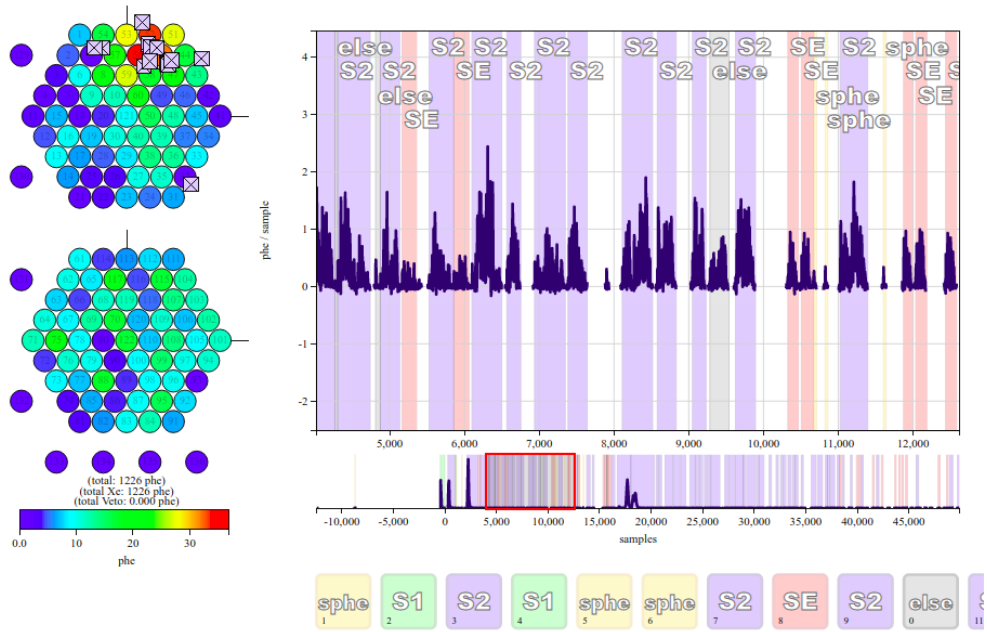

Figure 4.14: The above shows the Visualux plot of an $e-train$ in the middle of the detector, caused by photo-ionization on bulk impurities, which often occurs following high energy recoils. Many of the reconstructed positions occur in the same x-y area. This particular event has LUXstamp 7503581972765394.

usually, $e-trains$ have many pulses with similar x and y positions that could mimic a track in the detector. The majority of pulses in the $e-train$ do not have a phd/sample average above one, which helps to justify the exclusion of pulses below that threshold in section 4.4.2 on page 121. For an example of an $e-train$ in the middle of the detector, see figure 4.14.

The $e-train$ is possibly a form of photo-ionization electron background and has dependencies related to xenon impurity. Such a source could come from a delayed release of electrons from specifically electro-negative impurities in the xenon bulk. $E-trains$ tend to occur within one second of the S2 which caused them, and typically the location of an $e-train$ resolves close to the position of the S2 from which it originated (see figure 4.15) [117]. Thus, electron trains would not specifically be associated with charge built up on the sides of the detector. Although there have been observations of fluorescence of PTFE, which a fiducial radius cut could otherwise alleviate, the presence of electron trains away from the walls supports the notion that they are

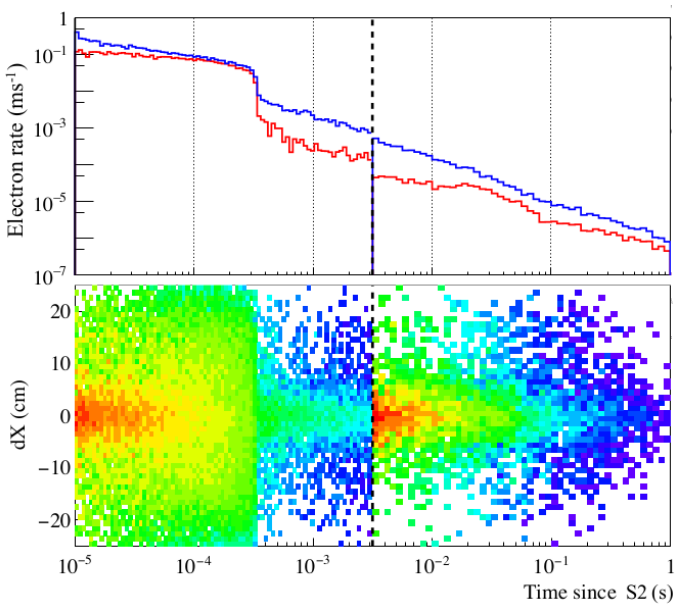

Figure 4.15: This figure explores $e-trains$ in two groupings: 0 - 3 ms and 3 - 1,000 ms following the antecedent S2, using Kr data for the former and background data for the latter in the top (red) and bottom (blue) 5 cm sections of the active Xe region. The top figure shows the $e-train$ rate vs the time since the generating S2 pulse. The bottom shows the x position distance of the $e-train$ vs the time since the S2, showing a strong correlation between the two. Figure reprinted from [117].

impurity related [118].

Another background similar to $e-trains$ occurs when accumulated electrons release from the side of the detector or from the top of the liquid surface in a large burst of ionization, commonly referred to as an electron burst or $e-burst$. Other literature may refer to this electron burst phenomenon as clustered electron emission, and another common name is electron burp or $e-burp$. Such an emission tends to occur within 50 ms of a large S2, which would result in the associated S2 being in a different event window than the corresponding $e-burst$, bracketed by relative calm in the detector [117]. Figure 4.17 (top) shows the $e-burst$ rate compared to the time since the associated S2, indicating that the delay time of the $e-burst$ follows an exponential fit with a characteristic delay time less than 10 ms, which could suggest that some type of electron reservoir fills from the antecedent S2 which then drains at a constant rate over time [117]. The duration of such $e-bursts$ lasts $\sim$10 - 100 μs, with the most probable peak widths, between a

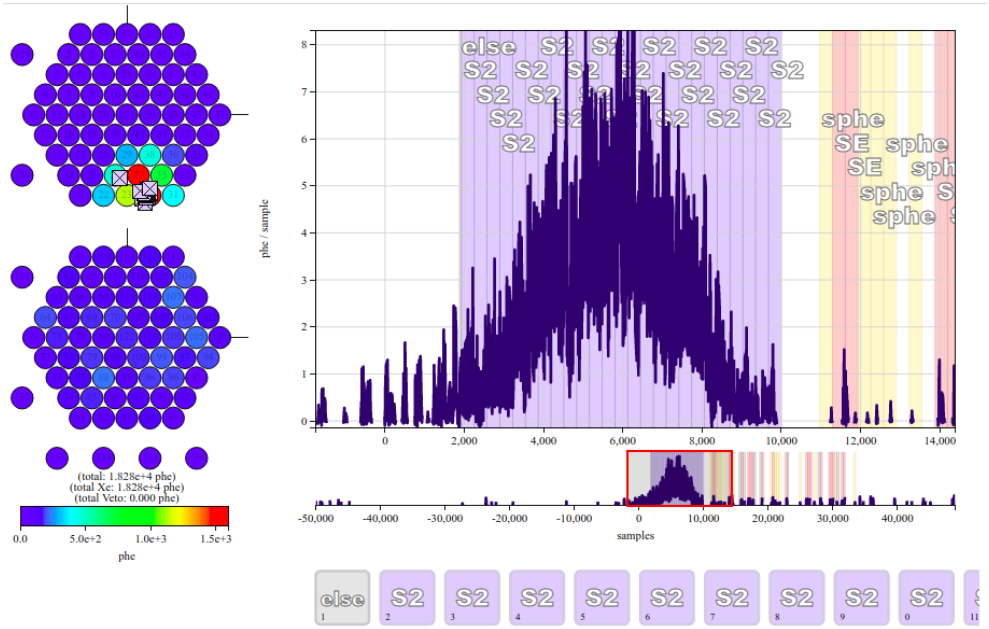

Figure 4.16: The above figure shows an $e - burst$ waveform in the Visualux viewer. A large amount of a nearly continuous level of ionization occurs in $e - bursts$ that could mimic a LIP event. Note the very straight track of the S2 pulses in the hit-map. This event has LUXstamp 7296779096987793.

quarter and three-quarters of the integrated pulse area, occurring ∼30 - 50 μs [117].

The $e - burst$ may contain as little as a few dozen or as many as tens of thousands of electrons, either tagged by the DPF as one long pulse or many short pulses, with pulse height structure gradually increasing at the beginning and slowly decreasing at the end. The $e - burst$ could become particularly problematic because the resulting pulse or pulses often have a higher phd/sample height than $e - trains$ over a large section of the event; having a consistent or continuous energy deposition remains a key factor in the identification of LIPs. Figure 4.16 shows an $e - burst$ with high pulse height in its latter half, qualifying for pulse $chopping$ on the event. At times, the elevated pulse height meets the qualifications for pulse $chopping$ (see section 3.3 on page 84) by SRP. $E - bursts$ do not typically have an associated S1, as determined by the pulse classifier, however, they could contain a pulse misclassified as an S1 or the modified DPF could mistakenly ascribe an $else$ classified pulse within the $e - burst$ as an S1-like Class 5 pulse which would cause the DPF to calculate corrected positions for associated S2 pulses which tend to have similar x and y

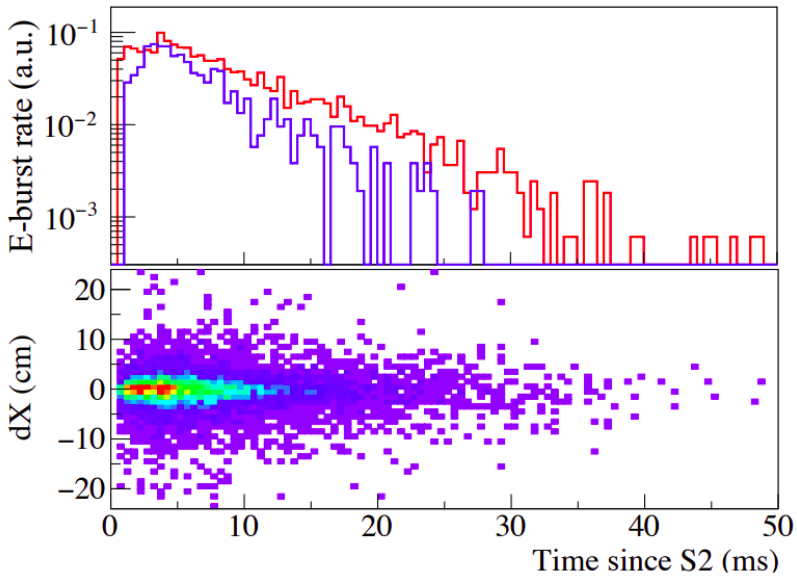

Figure 4.17: The top figure shows the rate of $e-bursts$ as a function of the time since their associated progenerating S2, the red and blue lines indicating the top and bottom 5 cm of the active Xe region, respectively. The bottom figure shows the difference in the x position of the $e-burst$ and its progenerating S2 as a function of the time since the S2, showing they generally have similar positions. Figures reprinted from [117].

positions. $E-bursts$ tend to have x and y positions close to their associated S2, a similarity which strengthens as the delay between the $e-burst$ and associated S2 increases as shown in figure 4.17 (bottom). The data filter and cuts used for the analysis must have the ability to remove these as candidate events because they otherwise contain LIP-like signatures.

The last background occurs when one or several PMTs fail to return to baseline. Commonly referred to as $zombie-pods$, these baseline shifts occur often following a high energy event. The baseline shift can mimic a long single pulse of ionization with the same x and y positions, thus appearing as a very long and straight track. Baseline shifts can occur within 32,000 samples of the originating impact during the event, or they may continue past the physical extent of the detector. Usually, the baseline shifts remain contiguous or have very few breaks despite having a very long pulse length. Thus, such baseline shifts would normally not have an impact when looking for multiple scatters. However, if multiple PMTs experience baseline shifts with a summed POD rate equating to several phd/sample, then the event would be be processed and $chopped$ by

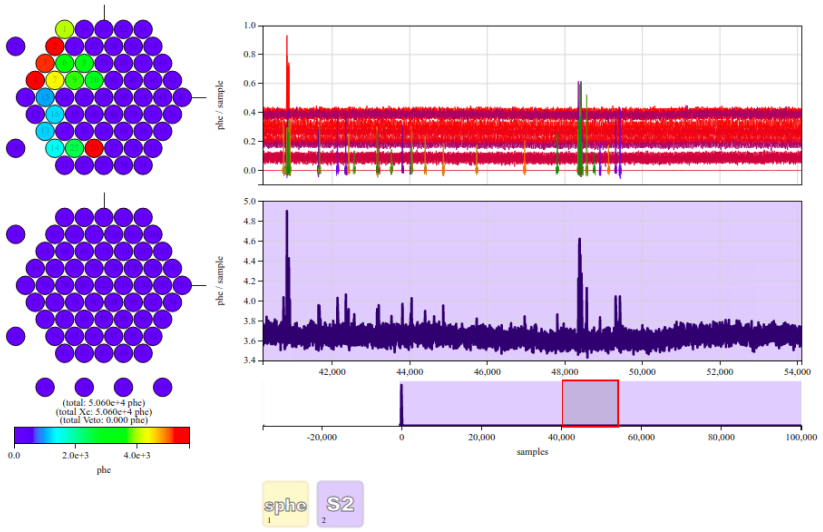

Figure 4.18: The above shows the Visualux plot of an elevated baseline shift without any pulse *chopping*. This particular example happens to be most apparent past the physical extent of the detector, but elevated baselines can occur within 32,000 samples. The top graph shows the output of each individual PMT; whereas the graph below it shows the summed waveform. As indicated by the top graph, several PMTs have failed to return to baseline but are otherwise flat. If the event had been *chopped*, the reconstructed positions would occur in the same x-y area. This particular event has LUXstamp 7603284302508470.

SRP. A *chopped* baseline shift would have similar x and y positions, and therefore the baseline shift could present many of the same problems as $e - bursts$ or $e - trains$. Frequently, but not always, a baseline shift will be below 4 phd/sample when the coincident time window does not have associated ionization as well. If a baseline shift occurs such that it has more than 4 phd/sample, it remains likely that multiple PMTs have contributed to the baseline shift or it has associated ionization. Figure 4.18 shows an example of an elevated baseline shift among several PMTs extending beyond 32,000 samples following a high energy recoil.

4.4.2 Data Analysis Cuts

Several constraints on candidate events helped the LUX Run03 LIP search to discern between background and signal. The event constraints, of course, also had their effect on LIP simulation efficiency. A decrease in efficiency would mean that if a LIP occurred through or near the detector, it would have an increased probability of escaping proper identification. Like many of the direct

detection experiments mentioned in section 4.2.3 on page 100, the LUX LIP search made cuts on event or pulse quality and quantity, incident angle, and some energy metric. A LIP filter code consisting of over a gross of different track and event related RQs was developed in order to search the simulations and live data for tracks, and when it identified a track, it recorded the relevant track RQs in a similar vein to DPF RQ identification. For the sake of brevity, this section shall discuss only those track RQs that had an impact upon the final analysis cuts.

Due to the fact that LUX cannot simulate electron trains (see section 4.3 on page 109), the search did not use cuts that would overly target or aggressively exclude events with an electron train or other electron background. Targeting events with an electron train for removal might otherwise remove LIP signals that could understandably precede an electron train. However, at the same time, the search did not want to have an electron train overly influence the characterization of the event. Therefore, the calculation of pulse track quantities did not include any pulse which had a pulse height below 1 phd/sample. The primary cut required that an event have five distinct S2 pulses of requisite height in order to calculate a track for that event. The five-pulse requirement was chosen in order to have a greater number of S2 pulses than the degrees of freedom for the position of a three-dimensional line, which is four. The $DOF = 4$ notion comes from having two DOF for direction on the unit sphere, a third for the point, and the fourth because one can translate the point. Furthermore, a previous study of simulated γ backgrounds in the Run03 LUX detector, based upon the material assay of detector components prior to installation, indicated γ backgrounds having a maximum of three scatters [119]. Requiring five scatters places one additional scatter beyond that which would otherwise eliminate γ-induced backgrounds from that study.

Although the LIP filter code looked at all pulses of the expanded S2 pulse definition in section 3.3 on page 84, and calculated tracks both for the expanded set as well as S2 classified pulses only, in the end, the analysis used only pulses classified strictly as S2 pulses in the calculation of pulse track quantities. The decision to limit pulses strictly to those classified as S2s helped to limit noise influence, and it did not prove particularly detrimental to simulation efficiency. This means that LIP candidates were processed both with and without an expanded S2 definition including not

only proper S2s, but also SE pulses, and S2 like Class 5 pulses. The restricted version removed the latter two candidate classes and also removed any S2-classified pulse below 1 phd/sample. The RQs mentioned in this section deal in regard to the restricted S2-only calculation unless otherwise noted. Graphs following in this section will contrast the test data set, in red, and the simulation set, in blue, shown for ease of discussion, instead of the entire live data set, unless otherwise noted.

Before placing further cuts on data and simulation, a pulse-length limit removed any event, not simply the pulse, with a length longer than 4,000 samples. The 4,000-sample limit paralleled the pulse $chopping$ requirement described in section 3.3 on page 84 and the limit was used because the filter code looked at both $chopped$ and $non-chopped$ versions of events. An event with a pulse greater than 4,000 samples would either have been $chopped$, in which case the code should focus on the $chopped$ version, or it did not have other characteristics for the SRP to $chop$ it and thus should remain excluded from the analysis. In essence, an event did not have a 'double jeopardy'[10] opportunity, such that once the SRP looked at an event and determined it not a LIP candidate, the filter code should not revisit that event.

A χ^2 parameter can often serve as a determinant for the goodness of fit of a reconstructed line to data, because of the expectation that deviations fall within a χ^2 distribution. The χ^2 of an event is given by

$$\chi^2 = \sum_{i=1}^{n} \left(\frac{e_i - q_i}{\sigma_i} \right)^2 \tag{4.4}$$

where e_i refers to the position of the fit line at point i, q_i refers to the observed value of the position of point i, n refers to the total number of fit points, and σ_i is the error of the reconstructed point, which comes from the Mercury program. Thus, the numerator of the χ^2 gives the perpendicular distance from the observed position to the fit line. The fit line was calculated so as to reduce the χ^2 of the event, having calculated all possible fit lines given the observed positions.

In order to require a well-defined track, a cut was used to require a reduced χ^2 or χ^2/DOF value be less than one for the event where DOF indicates the degrees of freedom defined by

[10]The term 'double jeopardy' refers to a concept in United States law, stemming from the fifth amendment to the Constitution, such that one cannot be prosecuted again for the same crime once one has been found not guilty of the crime at trial.

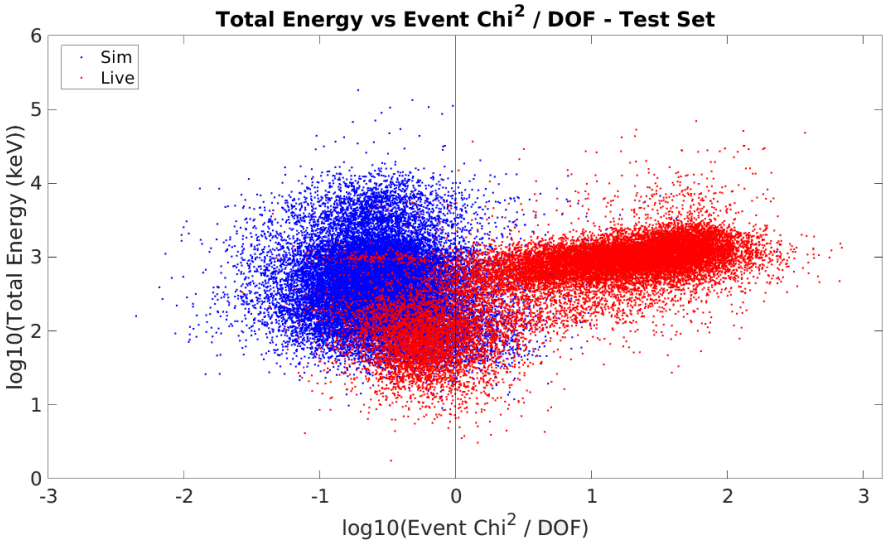

Figure 4.19: This figure represents the $\log_{10}\chi^2/DOF$ for live test data set (red) and simulation (blue); the black line shows the cut line of $\log_{10}\chi^2/DOF = 0$. The live (simulation) events reduced from 21,646 to 4,114 (25,723 to 23,902) under this cut.

$DOF = n - 4$ with n again indicating the number of S2 pulse positions used to create the fit line. Drawing a cut line at $\chi^2/DOF = 1$ ensured that the reconstructed lines fit well to their corresponding data. Any calculated line with a reduced $\log_{10}\chi^2 < 0$ was excluded *ab initio*. See figure 4.19 for the test data and simulation sets in the total energy vs $\log_{10}\chi^2$ parameter space. The graph shows two populations for the live events, one which has low χ^2 and low energy and the second which is of higher χ^2 and with somewhat higher energy. $E - bursts$ are more likely to make up much of the former population. The test set live (simulation) events reduced from 21,646 to 4,114 (25,723 to 23,902) under this cut, representing very large cut to the live events remaining in the test set; similarly, the full live set saw a reduction from 116,062 to 24,818 events.

The incident angle from vertical of the reconstructed track θ served as the second parameter from the filter code upon which a cut had been placed. As noted in section 4.4.1 on page 115, among the more problematic backgrounds in LUX were *chopped* baseline shifts, $e - trains$, and $e - bursts$, which often have similar x and y positions, thus appearing as a very straight track with vertical angle θ closer to zero. Furthermore, as expected from simulation due to the isotropic from above generation of the simulations, the angle of simulated tracks consisted of a wide range

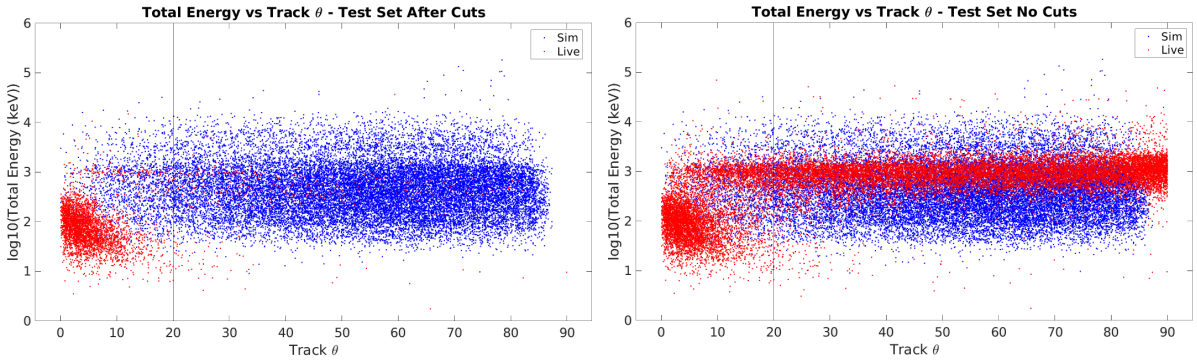

Figure 4.20: These figures represent the total energy vs track θ for live test data set (red) and simulation (blue) events for the reconstructed track line angle θ; the black line shows the $\theta = 20°$ cut line. The left figure shows these data with the previously applied χ^2 cut, and the right shows the space without the cut. The live test (simulation) events reduced to 355 (22,297) under this cut.

in θ within its allowed extrema of 0° to 90°. In an effort to limit the impact of those backgrounds while minimizing loss of simulation efficiency, a lower-bound requirement removed all tracks with $\theta < 20°$. See figure 4.20 for the simulation and test set data, both before and after the previously mentioned χ^2 cut, for the space of total energy vs track θ. As shown in the graph with the uncut live test set, there are two populations, similar to the χ^2 graph, one with low energy and low θ and one with higher energy and a broad range of θ. Contrasting the cut and uncut set, it can be seen that the broad range θ distribution has been largely removed due to the previous cut in χ^2, with the low energy population being now cut by the $\theta = 20°$ cut line. The live (simulation) events reduced to 355 (22,297) under this cut, and the full live set saw a reduction to 2,091 events. The over 90% decrease in live events compared to less than 5% loss in simulation events underscores the strength of the θ cut.

The third cut dealt with ensuring that the data points represented the subtended track which they purportedly represent. For each track, the track length TL was calculated using a generated convex hull dodecagon shape onto which the χ^2 minimized track was projected, and then the program determined the distance between the entrance and exit of the particle track from the detector. The analysis excluded any track which returned an error or incalculable track length. Another metric, here referred to as L_{data} represents the distance between the first and last S2 pulse of the

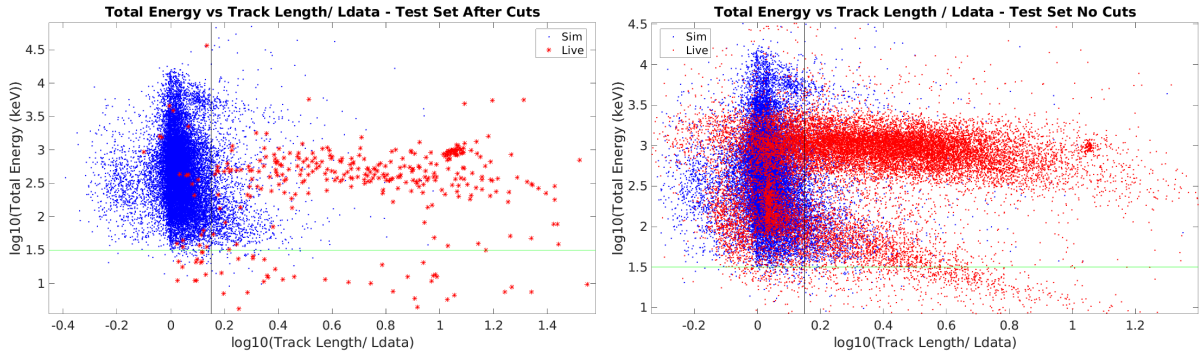

Figure 4.21: These figures represent the total energy vs the ratio of track length (TL) to L_{data}, with L_{data} being the distance from the first to last S2 of the event, for live test data set (red) and simulation (blue) events. The left figure shows these data with the previously applied cuts, and the right shows the space without the cuts. The vertical black line shows a cut at $TL/L_{data} = 1.44$; the horizontal green line indicates a cut in total energy at $10^{1.5}$ keV. The live test (simulation) events reduced to 18 (21,071) under these cuts.

track. Thus, the more that the actual data points subtended their associated track, and hence the detector itself, the better the resulting ratio TL/L_{data} would remain closer to unity. The L_{data} metric helps ensure that the candidate traverses much of the detector. Noting the possibility of truncated simulation S2 distance, an upper bound of $TL/L_{data} < 1.44$ remained generous, yet allowed for powerfully correlated discrimination of simulation from background. In addition, there remained several live events in the test set of lower total energy, mostly being $e - bursts$; a cut on total energy $E = 10^{1.5}$, which is approximately 31.6 keV. The total energy cut at this level does negatively impact the $0.01e$ charge simulations, however, simulation efficiency remained poor at that charge before applying the TL/L_{data} and total energy cuts, and the cuts were adjusted to ensure non-zero efficiency at $0.01e$. The live test set (simulation) events reduced to 18 (21,071) under these cuts (see figure 4.21), and the full live set reduced to 117 events.

For the final cuts, made in the space of standard deviation (std) of the S2 pair θ vs the Energy Per Track Length (EPTL), the simulations and live data were divided and treated as two sets, $chopped$ and $non - chopped$. The pair θ, distinct from the track θ, looks at the angle between each subsequent pair of S2 pulses of the event. A smaller standard deviation in pair θ would

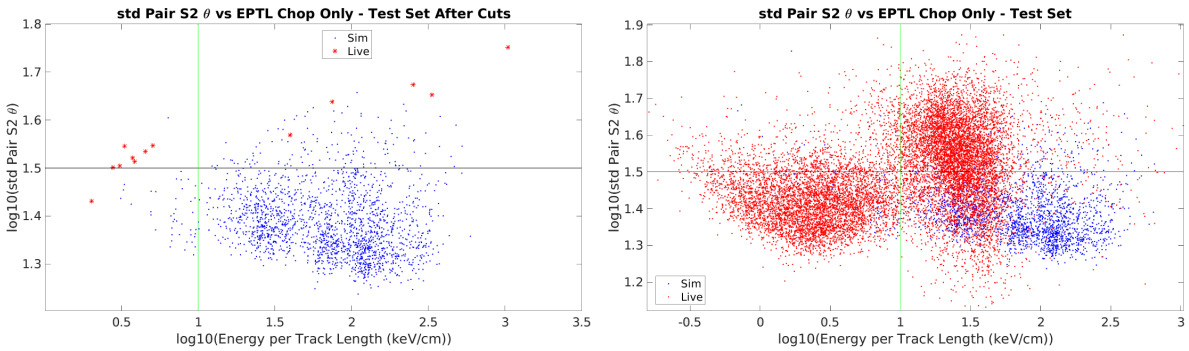

Figure 4.22: These figures represent the std pair θ vs EPTL of the *chopped* events, for live test data set (red) and simulation (blue). The black line represents a cut requiring std pair $\theta < 10^{1.5} \approx 31.62°$, and the green line EPTL > 10 keV/cm. The left figure shows these data with the previously applied cuts, and the right shows the space without the cuts. The cuts were drawn such that there was minimal overlap of simulation and live test events in the removed area of the right figure. All remaining *chopped* events in the live test set were removed, and 1819 of 1999 *chopped* simulated events survived.

indicate that the event overall remained straight throughout its length. Due to the fact that several backgrounds have small pair θ, care would still be needed in its implementation, requiring much of such backgrounds to have been removed by previous cuts. Additionally, the parameter EPTL remained useful as a measure of overall energy consistency. The EPTL also would serve as the primary means of identifying the charge of any detected signal.

Of the 18 remaining live test set events, 13 had been *chopped*. A cut requiring EPTL > 10 keV/cm and a cut requiring std pair $\theta < 10^{1.5}$, which is approximately 31.62°, removed all remaining events within the live test set, a requirement of this method. Now, viewing the left portion of figure 4.22, where previous cuts have been applied, the cuts may appear as overly conservative at the stated levels, however, investigation of the right side of the figure, which has no cuts, shows live events near and even overlapping the simulation set. The chosen cut levels were drawn in order to exclude regions where few simulation events exist. The choice to require the events to have high energy and low pair θ variability means that higher charge and straight tracks will survive. There is no problem of cutting away low energy or low charge events occurs because lower energy events are usually not *chopped*. Lower energy events often have more spread out S2 pulses, which

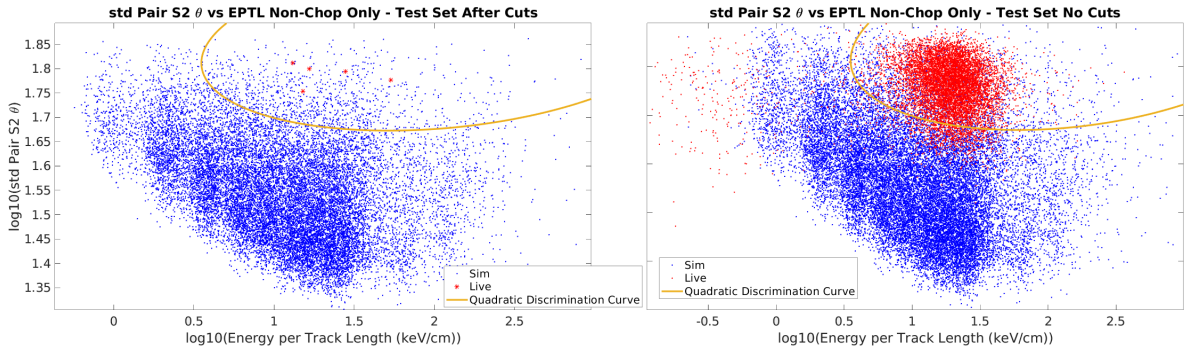

Figure 4.23: These figures represent the std pair θ vs EPTL of the $non-chopped$ events, for live test data set (red) and simulation (blue). The orange line represents the quadratic discrimination curve best separating the simulation and live populations. The left figure shows these data with the previously applied cuts, and the right shows the space without the cuts. The discrimination curve has been pulled further to the left by the influence of a population of low EPTL live events with high std θ, as shown in the right figure. All five of the live test set events are removed under this cut, as required, and 17,986 of 19,072 simulation $non-chopped$ events survive.

justifies the treatment of $chopped$ and $non-chopped$ events separately. Application of the EPTL and std θ cuts reduces the surviving $chopped$ simulation events from 1999 to 1819.

Application of cuts to the EPTL and std θ parameter space for $non-chopped$ events had more nuance than the $chopped$ space. Instead of using straight cut lines, all live test set and simulation events, prior to application of the χ^2 cut, were plotted in the parameter space. Then, a quadratic discriminant analysis determined the best curve line to separate the populations. Discriminant analysis, in essence a very basic machine learning technique, seeks to find the minimization of

$$\sum_i \sum_{j \neq 1} P\left(D_j|\pi_i\right) p_i C_{ji} \tag{4.5}$$

where p_i is the previous probability that the observation from π_i falls into the ith group. $P\left(D_j|\pi_i\right)$ is the probability that π_i falls into the region D_j, where the assignment is made to the population of j; C_{ji} is the cost of assigning an observation to the jth group when it actually comes from i [120]. Essentially, this entails arriving at a classification with the highest probability of being correct with the lowest cost associated with misclassification. Using the native Matlab program $fitcdiscr$ with

the quadratic option allows for generation of an equation of a curve given in $x,\ y$ space by [82]

$$-K = L_1 x + L_2 y + Q_{1,1} x^2 + (Q_{1,2} + Q_{2,1})\, xy + Q_{2,2} y^2 \tag{4.6}$$

where coefficients $L,\ Q$, and constant K are generated by the $fitcdiscr$ program. The resulting quadratic discrimination curve had the following values for coefficients:

$$\begin{aligned} K &= -416.14 \\ L &= \begin{bmatrix} -5.44 \\ 459.43 \end{bmatrix} \\ Q &= \begin{bmatrix} -1.80 & 3.48 \\ 3.47 & -127.83 \end{bmatrix} \end{aligned} \tag{4.7}$$

Following previous cuts, five $non-chopped$ events remained within the live test set, whereas the simulation set consisted of 19,072 $non-chopped$ events. Figure 4.23 on the preceding page shows this parameter space; the right figure shows insight into how the discriminant curve came about, with most live events in the upper right corner. The discrimination curve has been pulled further to the left as a result of the influence of a population of low EPTL live events with high std pair θ. All five of the live test set events are removed under this cut, as required, and 17,986 simulated $non-chopped$ events survive.

The summary and effect of all track requirements and cuts on the simulated events appears in figure 4.24. Of 25,723 simulated events that received a track, of which 19,888 survived all cuts, meaning that 77.23% of events that received a track survived. As indicated in the figure, the largest loss to efficiency occurred from an event not receiving a track for various reasons. See section 4.4.4 on page 135 for a discussion of efficiencies overall and in relation to the outcomes of machine learning.

The results which illustrate the application of all cuts mentioned in this section on the entire live dataset can be found in section 5 on page 138.

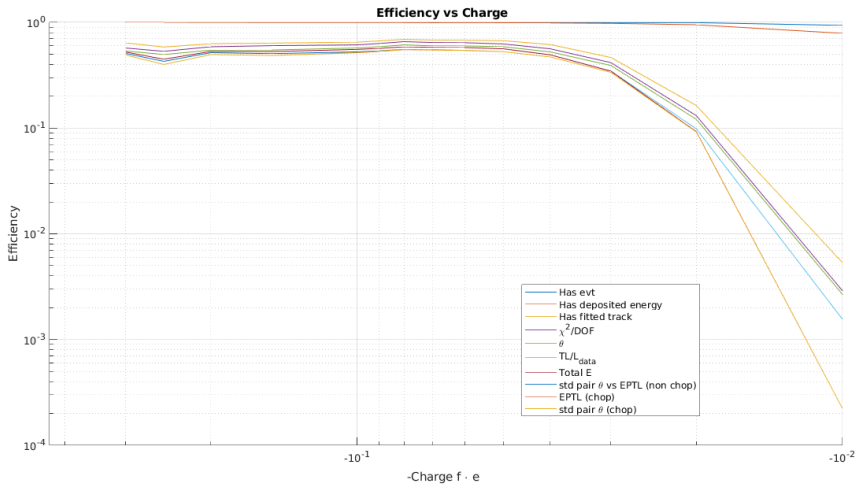

Figure 4.24: Figure of efficiency vs charge, showing the effect of each individual cut made using the traditional cut method. Of 25,723 simulated events which received a track, 19,888 events survived all cuts.

4.4.3 Machine Learning

One of the more innovative notions of late in data science and data analysis in multiple fields is the application of machine learning for classification purposes. In general, machine learning programs take multivariate data input, note relationships based upon the type of machine learning program, and create a binary or multi-class classification of events.

A second, parallel, LIP analysis used machine learning as an additional avenue for data analysis, applied in parallel to the traditional method of cuts described in the previous section. The outputs of the machine learning analysis applied here thus also sought a binary classification corresponding to signal or background. The machine learning techniques used for the LIP analysis, like many other machine learning analyses in particle physics [121], created a variable with a continuum between 0 and 1. Outputs closer to 0 indicate a more background-like event, whereas outputs closer to 1 indicate a more signal-like event. Varied machine learning programs such as those using neural nets or various types of decision tree based methods allow for outputs of 0 to 1 in order to indicate a binary preference.

As part of the background research done for the LIP analysis, many of the same variables used

in the traditional cuts section were analyzed using various different machine learning methods and programs. Upon investigation of neural nets and various types of decision trees, it appeared that Boosted Decision Trees (BDTs) provided the most powerful separation between background and simulation. The scikit-learn package, or sklearn, in Python generated the BDT, taking a normal Decision Tree Classifier and applying the $AdaBoostClassifier$ program to it [122]. For completeness, the settings were as follows: it had a maximum depth of 3, a minimum weight fraction of the leaf of 0.05, the number of estimators was 200, and the algorithm was "SAMME". It remains beyond the scope of this work to detail the rationale and choice behind the various settings, but the ones used are typical with variations tested resulting in equal or worse performance.

The BDT was initially trained on the previously mentioned 14-day live test dataset and the simulation set, both $chopped$ and $non-chopped$. In both the simulation and live datasets, similar restrictions to the traditional cut method were employed, those being that an event needed to have received a calculated track from the LIP filter code, excluded any event with its longest pulse greater than 4,000 samples as having been treated by the SRP, having been either $chopped$ or discarded, and any event with a χ^2 less than zero was discarded as invalid. The resulting sets had 25,723 simulated events and 21,646 remaining live events. Of these simulated and live events with a calculated track, 70% were taken to train the BDT, and the remainder used for validation. Cross-validation over several iterations indicated very high overall accuracy, greater than 99%, but with some fraction of the live test set leaking into signal.

However, the LIP search placed greater requirements on the BDT than having high overall accuracy; instead, the search made use of the $predict\_proba$ function native to the BDT software, which indicates how background-like or signal-like an event appears, and generates a decimal between 0 and 1, respectively. Figure 4.26 on page 133 shows examples of the spectrum of values with a bimodal distribution representing background-like and signal-like events. Running several thousand BDTs on the parameters mentioned in section 4.4.2 on page 121 along with the longest pulse, which served as a $chopped$ flag, then averaging the surviving simulation rates as well as the leakage magnitude and quantity, informed where to make the cut in the $predict\_proba$ spectrum.

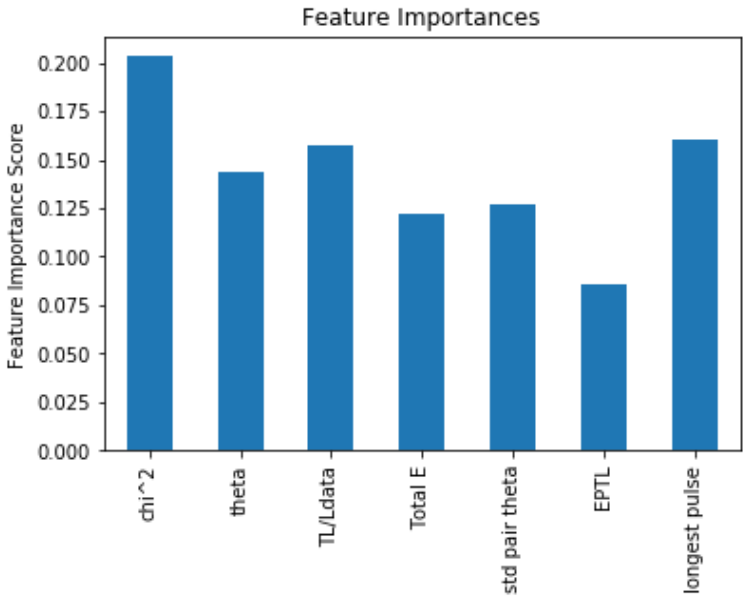

Figure 4.25: The histogram shows the feature importances, calculated with cross validation, of the seven-parameter BDT. The histogram indicated that the χ^2/DOF value played the greatest role at $\sim$20%, whereas the EPTL played a lesser role at $\sim$8%, and the others ranged around 12 - 15%.

The averages of the BDTs, which have statistical fluctuation, indicated that at $predict\_proba$ = 0.54 there would be an average anticipated simulation survival rate of approximately 74% of those events given a track, and the anticipated leakage, extrapolating from the survivors of the test set to the entire live data set, would result in approximately 0.1 leakage events.

Out of an abundance of caution, the final BDT selected was the one out of two thousand generated BDTs which had 0 leakage events in the live test set at the lowest $predict\_proba$ level (here, 0.51); its spectrum is shown in figure 4.26 on the next page (left), and its feature importances are shown in figure 4.25. The $predict\_proba$ spectrum for this BDT did indicate a notable mingling of signal and background in the middle of the histogram. Interestingly, the feature importances, calculated with cross-validation, indicated that the χ^2/DOF value played the greatest role at $\sim$20%, whereas the EPTL played a lesser role at $\sim$8%, and the others ranged around 12 - 15%. Unfortunately, this BDT had an overall simulation efficiency of approximately 69% at the 0.54 level, with charge-specific efficiencies indicated in figure 4.27 on page 136.

Being less restrictive regarding the parameters and taking advantage of more parameters cal-

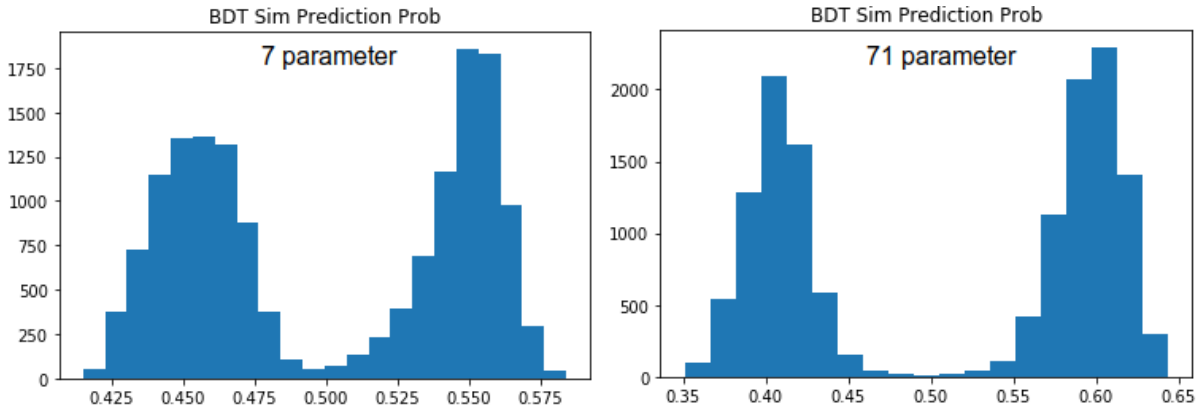

Figure 4.26: The $predict\_proba$ function native to the BDT software, which indicates how background-like or signal-like an event appears, and generates a decimal between 0 and 1, respectively. The left figure shows $predict\_proba$ for the seven-parameter BDT, whereas the right shows it for the 71-parameter BDT, applied to the 14 days of live data and simulation events. Note the greater spread between the bimodal peaks of the 71-parameter BDT versus that of the seven-parameter BDT. These spectra helped inform where to draw the $predict\_proba$ cut line for the their BDTs at 0.54 and 0.56, respectively.

culated by the LIP filter has the potential to increase overall simulation efficiency while similarly screening the live data. Now, the BDT expanded the parameters to 71 of the S2-only parameters calculated with the LIP filter, with special consideration given to exclude any parameter, such as the number of pulses prior to application of the 1 phd/sample pulse requirement, which would otherwise be biased against events with $e - trains$ or similar backgrounds. The LIP filter parameters used did include informed parameters, such as the ratio of the first two S2 pulse areas to the last two S2 pulse areas, but did not bother with the need to take the $\log_{10}$ of some parameters; $\log_{10}$ of parameters were used for the 7-parameter BDT because it was based on the $\log_{10}$ quantities used in the traditional cut method.

Using the same BDT settings as with the seven-parameter BDTs, with the $70:30$ train to test ratio, running several hundred BDTs indicated a projected leakage of less than 0.1 live events for the entire dataset at the 0.56 $predict\_proba$ cut line. It might appear that such a BDT has less powerful discrimination needing to draw the cut at 0.56 using the expanded parameter set because the seven-parameter BDT drew its cut at 0.54; however, the separation of the bimodal

spectrum in the 71-parameter BDT has greater peak separation and consequentially a longer tail to be considered (see the right portion of figure 4.26). Additionally, the expected simulation efficiency of those events with calculated tracks was determined to be approximately 90% at the 0.56 level, far superior to the seven-parameter BDT. Having determined where to make the $predict\_proba$ cut line, a new BDT was generated using all of the 14-day live test set and all simulation events. The final BDT did not have additional requirements placed upon it, other than that the 14-day set could not have leakage at 0.56, as with the seven-parameter BDT. Applying the final BDT to the simulation set preserved 89.6% simulation efficiency of those events with given tracks.

A short description of the 71 parameters used in the BDT, along with their importance rank and percentage weighting can be found in appendix B on page 175. It is interesting to note that the two highest-ranked features in the 71-parameter BDT were the longest S2 pulse and the χ^2/DOF with 6.43% and 5.08% respective weight in the BDT. The other parameters used in the 7 parameter BDT and cuts had the following ranks (weights) in the 71-parameter BDT: TL/L_{data} rank 6 (3.95%), track angle θ rank 9 (3.45%), std pair θ rank 17 (1.96%), EPTL using $g_{2,\ bottom}$ rank 40 (0.75%), and total corrected energy using $g_{2,\ bottom}$ rank 60 (0.33%). Somewhat surprisingly, the EPTL and total energy using the standard g_2 ranked higher than their counterparts at rank 14 and 40. Another way of making use of BDTs in future analyses could be to take the top several ranked features in a broad parameter BDT, and use those to inform either traditional cut parameter spaces or in smaller BDTs using fewer parameters. The final efficiencies for different charges can be found in figure 4.27 on page 136, shown along with the efficiency of generating a track from the simulations for reference. The results from the application of the BDTs to the remainder of the live dataset can be seen in section 5 on page 138.

It should be stated that machine learning techniques should not be treated as a mere 'magic box' where one simply gives the programs everything possible and it will produce the classification from thin air. Instead, machine learning techniques require careful section of the type of machine learning programs to use, proper input settings, and unbiased parameters to ensure proper classification of events. Even here, in the case of an expanded set of BDT input parameters, each

parameter had previously been graphed vs all of the other parameters and viewed by a person; RQ selections were made to avoid bias against systemic backgrounds, and the outcomes of hundreds of machine learning program analyses were furthermore investigated. Also, an informed selection of machine learning variables and settings produces a more understandable outcome which one can accept more reliably.

4.4.4 Efficiency Discussion

With regard to the efficiency of simulations for events with a calculated track, the three methods presented above performed well. The traditional cut method using six parameters with $chopping$ considerations had a simulation retention rate of approximately 77%. The BDT using the same parameters with the longest pulse as a $chopping$ flag largely validated the results from the cuts-based method, with slightly poorer results, having an average retention of approximately 69%. The 71-parameter BDT had the best average performance with approximately 90% retention of simulations with tracks. When parsed by charge, as shown in figure 4.27, the 71-parameter BDT had the best performance with the exception of $0.3e$, where the cuts-based method had slightly better performance. It remains possible that the BDT would be less likely to classify a $0.3e$ charge LIP as such because fewer $0.3e$ charge LIPs had been simulated than any other charge[11]. Thus, the BDT might be biased against higher charges which provided fewer relative training events than some of the lower charges.

As indicated in the figure, although most simulated events did successfully process to evt and rq files with some energy recorded as deposited in the detector, the largest overall reduction in simulation efficiency comes from not having been able to receive a track fit. Indeed, most f values gave tracks to only $\sim$60 - 70% of simulated events, with f = 0.01, 0.02, and 0.03 having given tracks to 5%, 16%, and 47%, respectively. There exist a number of possible causes why an event would not receive a track, the most prominent being that the event did not have the required five S2 pulses. Many simulated events had little energy deposited, at times having only an S1

[11]The taxing computational constraints for creating high-charge LIPs became a limiting factor in their further simulation and the overall range of the LIP search; simulation sets of $0.3e$ charge created .bin files of over 100 GB.

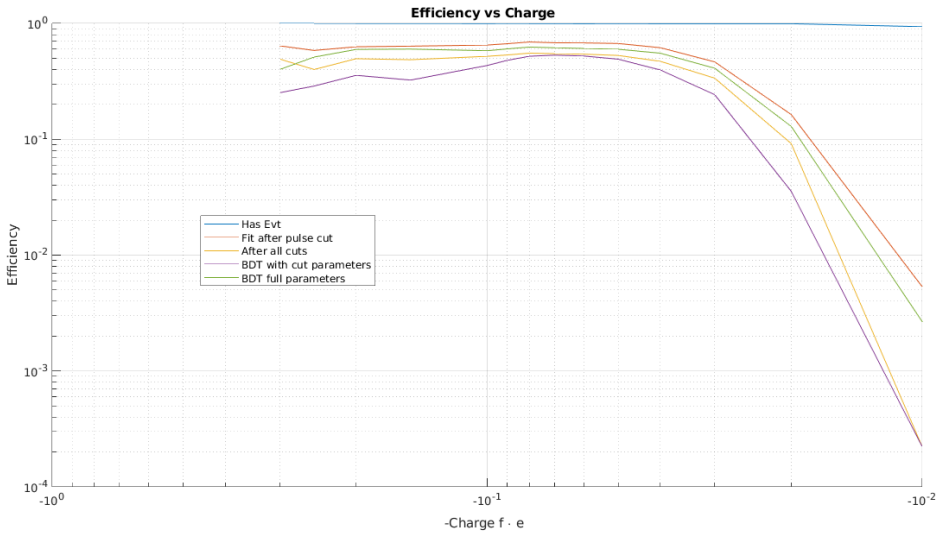

Figure 4.27: The overall simulation efficiency for each of the methods presented: the traditional cuts (orange), the seven-parameter BDT (purple), and the 71-parameter BDT (green). Also shown for reference is the efficiency of simulations to receive a calculated track (red), which caused the greatest overall loss in efficiency. Almost no loss occurred due to events not surviving the evt creation process (blue).

recorded, which obviously cannot receive a track fit. There were also a number of events that did have S2 pulses but were located in the detector corners and did not see more than four of such pulses. The case with many $f = 0.01$ simulations and the primary cause for efficiency loss at that charge was that the simulated LIP did not interact with the detector sufficiently; the limited interactions at $f = 0.01$ resulted in part from limitations on detector energy resolution and in part due to the 1 phd/sample requirement on pulses used to eliminate electron trains. Less commonly, other simulated events with insufficient pulse count resulted from restrictions in the pulse *chopping* mechanism; at times four or fewer S2 pulses resolved because the majority of the event had merged S2 pulses, but none of them had the required 4,000 sample length to trigger the pulse *chopping* mechanism and thus remained unprocessed by SRP. A similar difficulty could occur when an event, even one having five S2 pulses, has a merged S1-S2 pulse which receives an S2 classification but did not have a 4,000 sample pulse within the event to cause it to be *chopped*; an event without an S1 or S1-like Class 5 pulse would be lost. Thus, several improvements in *chopping* or pulse

classification could increase efficiency.

5. CONCLUSION

The standard deviation of the S2 pair θ and EPTL cuts were applied to the full dataset of $chopped$ and $non-chopped$ events, as mentioned at the end of section 4.4.2, and the results are displayed in figure 5.1. Interestingly, no live events survived in the $chopped$ space, but one $non-chopped$ event does survive as a potential LIP signal event, occurring just below the quadratic discrimination line. However, upon closer inspection, the potential candidate event having LUXstamp 8077402193022930 does not have five true S2 pulses. The fifth pulse used in the calculation of the regression line of this event and its track information is in fact merely a noise pulse within the long electron train of the event which happens to have surpassed the 1 phd/sample threshold. Also of note, if including the high rate CH_3T datasets, another $non-chopped$ event with LUXstamp 8265093586651094 surfaces nearby the previously mentioned event as well. However, being unable to discern high rate CH_3T events from events coincident to themselves or other phenomena, and hence the reason for excluding high rate CH_3T acquisitions from the LIP search, this event remains a mere curiosity and cannot be treated as signal. As a whole, it appears that the full $non-chopped$ live dataset has greater leakage into the simulation population than the 14-day live test dataset, with more events occurring with either lower EPTL or lower std pair θ; therefore, it is not surprising that the now-disqualified event leaked so close to the discrimination line. For $chopped$ events, there are a few which come close to the cut lines, but these are $e-bursts$ and thus of little note.

Applying the BDTs to the entire live data set for both the seven- and 71-parameter BDT at $predict\_proba$ = 0.54 and 0.56, respectively, yielded no potential signal events in either. The handful of events which came within 0.01 to 0.02 of the cutoff of the $predict\_proba$ spectrum, were not $e-bursts$ as noted above regarding the traditional cut method, but instead appeared to be high energy multiple or coincident recoils. For the seven-parameter BDT, the abundance of caution regarding the choice of BDT proved important because although lowering the cut level to 0.52, for instance, would have increased efficiency to $\sim$90% of events with a track, live events

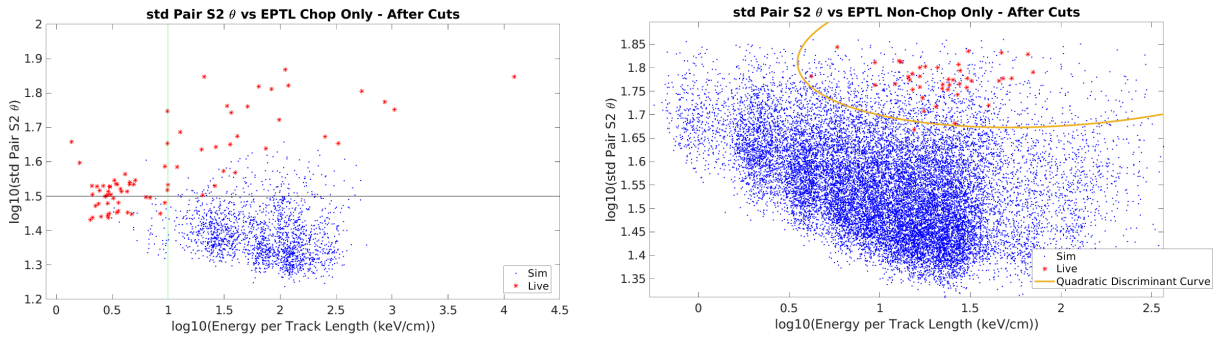

Figure 5.1: These figures represent the std pair θ vs EPTL of the $non-chopped$ (right) and $chopped$ (left) events, for the entire LIP search live set (red) and simulations (blue) following previous cuts. The orange line represents the quadratic discrimination curve best separating the simulation and live populations of the $non-chopped$ set. The one event in the $non-chopped$ space which leaks slightly below the cut line has only four real S2 pulses, the fifth being part of an $e-train$ and is disqualified. Although there are several $chopped$ events near the cut lines, they are $e-bursts$ and of little note.

started to leak into signal at 0.53. The 71-parameter BDT saw one event of live leakage at 0.55; leakage into both BDTs gradually increased as the $predict\_proba$ lowered. The informed choices of BDT $predict\_proba$ levels stemming from multiple runs of the respective BDT using the 14-day live test set proved important.

To arrive at the final limit, the equation for LIP flux from equation 4.3 on page 101, where $\Phi = \dfrac{N}{\epsilon\Omega At}$, must be applied to the results of the simulation efficiency above. The equation for the area A of the dodecagon face is $A = 12a^2\tan(\alpha)$ where α is angle the between the circumradius and the apothem a of the dodecagon. Given a known apothem in LUX to the PTFE of $a = 23.65$ cm [59] then $A = 1.80 \cdot 10^3$ cm^2. The solid angle of the detector $\Omega = 3.78$ sr [123], and livetime $t = 7.3923 \cdot 10^6$ s amounting to 85.5592 live days. Applying the Feldman-Cousins 90% confidence interval for no observations and no background gives an upper value for N of 2.44 [124]. The resulting LIP flux limit is shown in the range of $0.01e$ to $0.3e$ in figure 5.2 for the cut-based efficiency ϵ as well as the seven- and 71-parameter BDTs.

The flux, determined as low as $8.8 \cdot 10^{-11}$ cm^{-2} s^{-1} sr^{-1}, with most charges near approximately 10^{-10} cm^{-2} s^{-1} sr^{-1}, quite reasonably follows the pattern of the efficiency results from

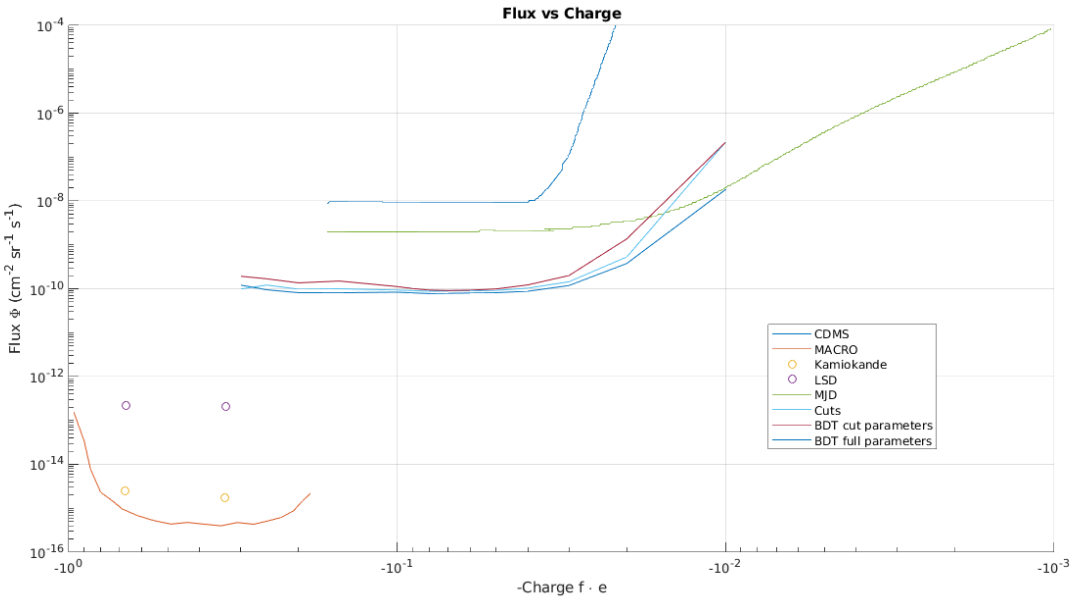

Figure 5.2: This shows the final flux limit range of $0.01e$ to $0.3e$ for the cut method as well as the seven- and 71-parameter BDTs. The results of previous work summarized in figure 4.3 on page 100 are also displayed for reference.

figure 4.27 on page 136. The seven-parameter BDT shows slightly worse performance than the traditional cut method on the seven parameters; however the difference between the two methods remains very slight. Indeed, the closeness of the results of the seven-parameter BDT and the cut method can be looked at as a verification that the BDT can produce results with reasonable associations to more established methods of analysis. The 71-parameter BDT performs best having a lower calculated flux than the other methods, with the exception of $0.3e$, where the cut method has a slightly lower result. The 71-parameter BDT result also performs better than the MJD at all mutually simulated charges including $0.01e$ having a flux of only $1.8 \cdot 10^{-8}$ cm^{-2} s^{-1} sr^{-1}, but of course, the result does not perform better than MACRO with its extremely low flux value at high charge.

5.1 Future Work

Future work could make use of a greater understanding of electron trains and electron bursts in order to better understand these backgrounds and eliminate them. One of the main hindrances of

the LIP search at lower charges came from pulse requirements and analysis cuts made to exclude electron background pulses. Simulations to better understand electron backgrounds would play a critical role, and it is hoped that a future endeavor could incorporate some of the suggestions mentioned at the end of section 4.3 dealing with simulations, such as taking known $e-trains$, $e-bursts$, and even baseline shifts and then adding them on to simulated events; creating simulations in this fashion resembles methods for generating $salt$ events used in the WIMP search. Also, generating LIP simulations with the energy-only portion of the simulation method calculated by simulating the LIP going through a long block of liquid Xe would be a more efficient method than using LUXSim twice, once for getting the energies and then again with the MUSUN generator.

An improved $chopping$ mechanism could improve a future LIP search as well. Being able to better discern a merged S1-S2 pulse as a $chopping$ event candidate would improve efficiency; an event with a merged S1-S2 classified as an S2 pulse would not receive corrected energies and positions. A suggested method of discerning merged S1-S2 pulses can be found in section 3.2.3 on page 71 which deals with pulse classification in the DPF. In the pulse classification section, various $else$ pulses falling into the populations referenced in figure 3.5 on page 72 for the boxcar S1 cut, and in figure 3.8 on page 75 with regard to the width cut, actually contain S1-S2 mergers. If the SRP program could be modified to be able to remove or tag an elevated baseline shift, or $ab\ initio$ exclude merged electron bursts and backgrounds, then this would also improve a future endeavor. An additional method to improve efficiency would be to enable the SRP to $chop$ events with pulses even less than 4,000 samples long, provided it does not become computationally burdensome. Lowering the sample length requirement would save many events which might otherwise not meet the five S2 pulse requirement but have long merged S2 pulses that fall short of the 4,000-sample length. Several of the notions and details for efficiency improvement appear in section 4.4.4 on page 135.

Of course, an elementary method to improve the final limit would be to process the remainder of Run03 with 100 pulses and with the SRP program for $chopping$; to do so would increase the total livetime by approximately 13.8 days. Non-calibration datasets in Run03 still remain, and

appendix A on page 156 details those missing acquisitions. Also, given improvements in position reconstruction and energy analysis, making certain to account for the issue of charge build-up on the detector walls during Run04, the task of performing a LUX LIP search for Run04 remains within the grasp of future scientific endeavors. The LUX Run04 has the advantage of being able to make use of the water tank and its PMTs as an additional trigger and energy check. Similarly, the techniques presented here can apply to the much larger LZ detector, which undoubtedly could push the LIP flux limit even lower.

In parting, there remains much about the universe still not understood by science. Dark matter still serves as one of the great mysteries of the modern era. However, with continued improvements in detector technology, such as LZ, the scientific community will hopefully resolve our understanding of dark matter. The LIP study presented in this work helps to constrain the possibilities of more exotic dark matter and other physical constructions, yet the possibility of fractionally charged particles remains. This work may also serve as a template for further study and exploration for LIPs as well as for additional applications. It is hoped that the information presented here can not only help future work within LUX and LZ but can help mankind to better understand the universe.

REFERENCES

[1] A. A. Michaelson *Annual Register 1894-1895*, p. 150, 1894.

[2] F. Zwicky, "Die Rotreshiebung von Extragalaktishen Nebeln. (German) [The Redshift of Extragalactic Nebulae]," *Helvetica Physica Acta*, vol. 6, pp. 110–127, 1933.

[3] F. Zwicky, "On the Masses of Nebulae and of Clusters of Nebulae," *The Astrophysical Journal*, vol. 86, p. 217, 1937.

[4] G. Bertone and D. Hooper, "History of Dark Matter," *Reviews of Modern Physics*, vol. 90, 2018.

[5] J. H. Oort, "Some Problems Concerning the Structure and Dynamics of the Galactic System and the Elliptical Nebulae NGC 3115 and 4494," *The Astrophysical Journal*, vol. 91, p. 273, Apr 1940.

[6] H. W. Babcock, "The Rotation of the Andromeda Nebula," *Lick Observatory Bulletin*, vol. 19, pp. 41–51, 1939.

[7] V. C. Rubin and W. K. Ford, Jr., "Rotation of the Andromeda Nebula from a Spectroscopic Survey of Emission Regions," *The Astrophysical Journal*, vol. 159, p. 379, Feb 1970.

[8] R. Massey, T. Kitching, and J. Richard, "The Dark Matter of Gravitational Lensing," *Reports on Progress in Physics*, vol. 73, p. 086901, Aug 2010.

[9] D. Clowe, M. Bradač, A. H. Gonzalez, M. Markevitch, S. W. Randall, *et al.*, "A Direct Empirical Proof of the Existence of Dark Matter," *The Astrophysical Journal*, vol. 648, pp. L109–L113, Sep 2006.

[10] M. Markevitch, A. H. Gonzalez, D. Clowe, A. Vikhlinin, W. Forman, *et al.*, "Direct Constraints on the Dark Matter Self-Interaction Cross Section from the Merging Galaxy Cluster 1E 0657-56," *The Astrophysical Journal*, vol. 606, pp. 819–824, May 2004.

[11] M. Markevitch, A. H. Gonzalez, L. David, A. Vikhlinin, S. Murray, *et al.*, "A Textbook Example of a Bow Shock in the Merging Galaxy Cluster 1E 0657-56," *The Astrophysical Journal*, vol. 567, pp. L27–L31, Mar 2002.

[12] W. J. Percival, B. Reid, D. J. Eisenstein, N. Bahcall, T. Budavari, *et al.*, "Baryon Acoustic Oscillations in the Sloan Digital Sky Survey Data Release 7 Galaxy Sample," *Monthly Notices of the Royal Astronomical Society*, vol. 401, pp. 2148 – 2168, Feb 2010.

[13] E. Pease, *Rare-Event Searches in Liquid Xenon with the LUX and LUX-ZEPLIN Detectors*. PhD thesis, Yale University, 2017.

[14] C. Frenk and S. White, "Dark Matter and Cosmic Structure," *Annalen der Physik*, vol. 524, no. 9-10, pp. 507–534, 2012.

[15] G. F. Smoot, "COBE Observations and Results," in *3K Cosmology* (L. Maiani, F. Melchiorri, and N. Vittorio, eds.), vol. 476 of *American Institute of Physics Conference Series*, pp. 1–10, May 1999.

[16] A. A. Penzias and R. W. Wilson, "A Measurement of Excess Antenna Temperature at 4080 Mc/s.," *The Astrophysical Journal*, vol. 142, pp. 419–421, July 1965.

[17] D. Scott and G. F. Smoot, "Cosmic Microwave Background Mini-review," *arXiv e-prints*, p. arXiv:1005.0555, May 2010.

[18] C. H. Faham, *Prototype, Surface Commissioning and Photomultiplier Tube Characterization for the Large Underground Xenon (LUX) Direct Dark Matter Search Experiment*. PhD thesis, Brown University, 2014.

[19] Planck Collaboration, P. A. R. Ade, N. Aghanim, M. Arnaud, M. Ashdown, *et al.*, "Planck 2015 Results. XIII. Cosmological Parameters," *Astronomy and Astrophysics*, vol. 594, p. A13, Sep 2016.

[20] W. Hu, "Lecture Notes on CMB Theory: From Nucleosynthesis to Recombination," *arXiv e-prints*, p. arXiv:0802.3688, Feb 2008.

[21] G. Lazarides, "Introduction to Cosmology," *arXiv e-prints*, pp. hep–ph/9904502, Apr 1999.

[22] C. J. Sofka, *Low Energy Nuclear Recoil Response in Xenon Gas for Low Mass Dark Matter WIMP Search*. PhD thesis, Texas A&M University, 2014.

[23] Planck Collaboration, P. A. R. Ade, N. Aghanim, C. Armitage-Caplan, M. Arnaud, *et al.*, "Planck 2013 Results. XVI. Cosmological Parameters," *Astronomy and Astrophysics*, vol. 571, p. A16, Nov 2014.

[24] C. Alcock, R. A. Allsman, D. R. Alves, T. S. Axelrod, A. C. Becker, *et al.*, "The MACHO Project: Microlensing Results from 5.7 Years of Large Magellanic Cloud Observations," *The Astrophysical Journal*, vol. 542, pp. 281–307, Oct 2000.

[25] P. Tisserand, L. Le Guillou, C. Afonso, J. N. Albert, J. Andersen, *et al.*, "Limits on the MACHO Content of the Galactic Halo from the EROS-2 Survey of the Magellanic Clouds," *Astronomy and Astrophysics*, vol. 469, pp. 387–404, Jul 2007.

[26] P. J. Kernan and L. M. Krauss, "Refined Big Bang Nucleosynthesis Constraints on Ω_B and N_ν," *Physical Review Letters*, vol. 72, pp. 3309–3312, May 1994.

[27] A. Lépine-Szily and P. Descouvemont, "Nuclear Astrophysics: Nucleosynthesis in the Universe," *International Journal of Astrobiology*, vol. 11, pp. 243–250, Oct 2012.

[28] Q. R. Ahmad, R. C. Allen, T. C. Andersen, J. D. Anglin, J. C. Barton, *et al.*, "Direct Evidence for Neutrino Flavor Transformation from Neutral-Current Interactions in the Sudbury Neutrino Observatory," *Physical Review Letters*, vol. 89, p. 011301, Jul 2002.

[29] K. Eitel, "Direct Neutrino Mass Experiments," *Nuclear Physics B - Proceedings Supplements*, vol. 143, pp. 197 – 204, 2005. NEUTRINO 2004.

[30] Y. Fukuda, T. Hayakawa, E. Ichihara, K. Inoue, K. Ishihara, *et al.*, "Evidence for Oscillation of Atmospheric Neutrinos," *Physical Review Letters*, vol. 81, pp. 1562–1567, Aug 1998.

[31] G. Bertone, D. Hooper, and J. Silk, "Particle Dark Matter: Evidence, Candidates and Constraints," *Physics Reports*, vol. 405, pp. 279–390, Jan 2005.

[32] J. Beringer, J. F. Arguin, R. M. Barnett, K. Copic, O. Dahl, *et al.*, "Review of Particle Physics," *Physical Review D*, vol. 86, p. 010001, Jul 2012.

[33] J. L. Feng, "Dark Matter Candidates from Particle Physics and Methods of Detection," *Annual Review of Astronomy and Astrophysics*, vol. 48, pp. 495–545, Sep 2010.

[34] H. Miyazawa, "Baryon Number Changing Currents," *Progress of Theoretical Physics*, vol. 36, pp. 1266–1276, Dec 1966.

[35] A. Ringwald (DESY), L. J. Rosenberg, and G. Rybka, "Axions and Other Similar Particles," *Particle Data Group*, 2017.

[36] D. Wu, "A Brief Introduction to the Strong CP Problem," *Zeitschrift für Naturforschung*, vol. A52, pp. 179–181, 1997.

[37] S. J. Asztalos, L. J. Rosenberg, K. van Bibber, P. Sikivie, and K. Zioutas, "Searches for Astrophysical and Cosmological Axions," *Annual Review of Nuclear and Particle Science*, vol. 56, pp. 293–316, May 2006.

[38] J. L. Hewett, H. Weerts, R. Brock, J. N. Butler, B. C. K. Casey, *et al.*, "Fundamental Physics at the Intensity Frontier," *arXiv e-prints*, p. arXiv:1205.2671, May 2012.

[39] The MACRO Collaboration, "Final Search for Lightly Ionizing Particles with the MACRO Detector," *arXiv e-prints*, pp. hep–ex/0402006, Feb 2004.

[40] K. B. Prasad, *Search for Lightly Ionizing Particles Using CDMS-II Data and Fabrication of CDMS Detectors with Improved Homogeneity in Properties*. PhD thesis, Texas A&M University, 2013.

[41] C. N. Yang, "Charge Quantization, Compactness of the Gauge Group, and Flux Quantization," *Physical Review D*, vol. 1, pp. 2360–2360, Apr 1970.

[42] R. Foot, H. Lew, and R. R. Volkas, "A Model with Fundamental Improper Spacetime Symmetries," *Physics Letters B*, vol. 272, no. 1, pp. 67 – 70, 1991.

[43] B. Holdom, "Two $U(1)$'s and ϵ Charge Shifts," *Physics Letters*, vol. 166B, pp. 196–198, 1986.

[44] B. Holdom, "Searching for ϵ Charges and a New $U(1)$," *Physics Letters B*, vol. 178, no. 1, pp. 65 – 70, 1986.

[45] A. A. Prinz, *The Search for Millicharged Particles at SLAC*. PhD thesis, Stanford University, 2001.

[46] S. A. Abel, M. D. Goodsell, J. Jaeckel, V. V. Khoze, and A. Ringwald, "Kinetic Mixing of the Photon with Hidden $U(1)$s in String Phenomenology," *Journal of High Energy Physics*, vol. 2008, p. 124, Jul 2008.

[47] H. Goldberg and L. J. Hall, "A New Candidate for Dark Matter," *Physics Letters B*, vol. 174, no. 2, pp. 151 – 155, 1986.

[48] P. A. M. Dirac, "Quantised Singularities in the Electromagnetic Field," *Proceedings of the Royal Society of London. Series A, Containing Papers of a Mathematical and Physical Character*, vol. 133, no. 821, pp. 60–72, 1931.

[49] F. A. Bais, *TO BE OR NOT TO BE?: Magnetic Monopoles in Non-Abelian Gauge Theories*, pp. 271–307. World Scientific Publishing Co. Pte. Ltd., 2005.

[50] R. Foot, H. Lew, and R. R. Volkas, "Electric-Charge Quantization," *Journal of Physics G Nuclear Physics*, vol. 19, pp. 361–372, Mar 1993.

[51] R. Foot, "New Physics from Electric Charge Quantization?," *Modern Physics Letters A*, vol. 06, no. 07, pp. 527–529, 1991.

[52] LUX Collaboration, D. S. Akerib, H. M. Araújo, X. Bai, A. J. Bailey, *et al.*, "First Results from the LUX Dark Matter Experiment at the Sanford Underground Research Facility," *Physics Review Letters*, vol. 112, p. 091303, Mar 2014.

[53] D. S. Akerib, C. W. Akerlof, C. M. Ignarra, K. O'Sullivan, P. A. Terman, *et al.*, "Projected WIMP Sensitivity of the LUX-ZEPLIN (LZ) Dark Matter Experiment," *arXiv e-prints*, p. arXiv:1802.06039, Feb 2018.

[54] A. Hitachi, "Properties of Liquid Xenon Scintillation for Dark Matter Searches," *Astroparticle Physics*, vol. 24, no. 3, pp. 247 – 256, 2005.

[55] LUX Collaboration, D. S. Akerib, S. Alsum, H. M. Araújo, P. A. Terman, *et al.*, "Calibration, Event Reconstruction, Data Analysis, and Limit Calculation for the LUX Dark Matter Experiment," *Physical Review D*, vol. 97, p. 102008, May 2018.

[56] E. M. Gushchin, A. A. Kruglov, and I. M. Obodovskii, "Emission of "Hot" Electrons from Liquid and Solid Argon and Xenon," *Moscow Engineering Physics Institute*, May 1982.

[57] P. Sorensen, "Electron Train Backgrounds in Liquid Xenon Dark Matter Search Detectors Are Indeed Due to Thermalization and Trapping," *arXiv e-prints*, p. arXiv:1702.04805, Feb 2017.

[58] J. Xu, B. Lenardo, D. Naim, A. Bernstein, K. Kazkaz, *et al.*, "Electron Extraction Efficiency Study for Dual-Phase Xenon Dark Matter Experiments," *Physical Review D*, vol. 99, p. 103024, May 2019.

[59] R. Mannino, *Measuring Backgrounds from 85-Kr and 210-Bi to Improve Sensitivity of Dark Matter Detectors*. PhD thesis, Texas A&M University, 2017.

[60] J. Verbus, *An Absolute Calibration of Sub-1 keV Nuclear Recoils in Liquid Xenon Using D-D Neutron Scattering Kinematics in the LUX Detector*. PhD thesis, Brown University, 2016.

[61] C. M. B. Monteiro, L. M. P. Fernandes, J. A. M. Lopes, L. C. C. Coelho, J. F. C. A. Veloso, *et al.*, "Secondary Scintillation Yield in Pure Xenon," *Journal of Instrumentation*, vol. 05, p. 05001, May 2007.

[62] D. C. Malling, *Measurement and Analysis of WIMP Detection Backgrounds, and Characterization and Performance of the Large Underground Xenon Dark Matter Search Experiment*. PhD thesis, Brown University, 2014.

[63] R. Platzman, "Total Ionization in Gases by High-Energy Particles: An Appraisal of Our Understanding," *The International Journal of Applied Radiation and Isotopes*, vol. 10, pp. 116–127, Apr 1961.

[64] C. E. Dahl, *The Physics of Background Discrimination in Liquid Xenon, and First Results from Xenon10 in the Hunt for WIMP Dark Matter.* PhD thesis, Princeton University, 2009.

[65] J. Thomas and D. A. Imel, "Recombination of Electron-Ion Pairs in Liquid Argon and Liquid Xenon," *Physical Review A*, vol. 36, pp. 614–616, Jul 1987.

[66] R. Knoche, *Signal Corrections and Calibrations in the LUX Dark Matter Detector*. PhD thesis, University of Maryland, College Park, 2016.

[67] P. Phelps, *The LUX Dark Matter Experiment: Detector Performance and Energy Calibration*. PhD thesis, Case Western Reserve University, 2014.

[68] D. S. Akerib, X. Bai, E. Bernard, A. Bernstein, A. Bradley, *et al.*, "An Ultra-Low Background PMT for Liquid Xenon Detectors," *Nuclear Instruments and Methods in Physics Research A*, vol. 703, pp. 1–6, Mar 2013.

[69] D. S. Akerib, X. Bai, S. Bedikian, E. Bernard, A. Bernstein, *et al.*, "The Large Underground Xenon (LUX) Experiment," *Nuclear Instruments and Methods in Physics Research A*, vol. 704, pp. 111–126, Mar 2013.

[70] F. Neves, A. Lindote, V. Solovov, C. Silva, P. Bras, *et al.*, "Measurement of the Absolute Reflectance of Polytetrafluoroethylene (PTFE) Immersed in Liquid Xenon," *Journal of Instrumentation*, vol. 12, pp. P01017–P01017, Jan 2017.

[71] D. Akerib, X. Bai, E. Bernard, A. Bernstein, A. Bradley, *et al.*, "Technical Results From the Surface Run of the LUX Dark Matter Experiment," *Astroparticle Physics*, vol. 45, pp. 34 – 43, 2013.

[72] D. S. Akerib, S. Alsum, H. M. Araújo, X. Bai, P. Terman, *et al.*, "^{83m}Kr Calibration of the 2013 LUX Dark Matter Search," *arXiv e-prints*, p. arXiv:1708.02566, Aug 2017.

[73] L. W. Kastens, S. B. Cahn, A. Manzur, and D. N. McKinsey, "Calibration of a Liquid Xenon Detector with ^{83m}Kr," *Physical Review C*, vol. 80, p. 045809, Oct 2009.

[74] J. R. Verbus, C. A. Rhyne, D. C. Malling, S. Chan, L., C. H. Faham, *et al.*, "Proposed Low-Energy Absolute Calibration of Nuclear Recoils in a Dual-Phase Noble Element TPC Using D-D Neutron Scattering Kinematics," *Nuclear Instruments and Methods in Physics Research A*, vol. 851, pp. 68–81, Apr 2017.

[75] D. S. Akerib, S. Stephenson, T. J. Sumner, M. Szydagis, P. A. Terman, *et al.*, "Low-Energy (0.7-74 keV) Nuclear Recoil Calibration of the LUX Dark Matter Experiment Using D-D Neutron Scattering Kinematics," *arXiv e-prints*, p. arXiv:1608.05381, Aug 2016.

[76] D. Akerib, H. Araújo, X. Bai, A. Bailey, J. Balajthy, E. Bernard, *et al.*, "Radiogenic and Muon-Induced Backgrounds in the LUX Dark Matter Detector," *Astroparticle Physics*, vol. 62, p. 33–46, Mar 2015.

[77] D. S. Akerib, X. Bai, S. Bedikian, E. Bernard, A. Bernstein, *et al.*, "Radio-Assay of Titanium Samples for the LUX Experiment," *arXiv e-prints*, p. arXiv:1112.1376, Dec 2011.

[78] D. S. Akerib, C. Chiller, T. J. R. Davison, C. Nehrkorn, P. A. Terman, *et al.*, "Chromatographic Separation of Radioactive Noble Gases from Xenon," *Astroparticle Physics*, vol. 97, pp. 80–87, Jan 2018.

[79] F. E. Gray, C. Ruybal, J. Totushek, D. M. Mei, K. Thomas, and C. Zhang, "Cosmic Ray Muon Flux at the Sanford Underground Laboratory at Homestake," *Nuclear Instruments and Methods in Physics Research A*, vol. 638, pp. 63–66, May 2011.

[80] D. R. Tiedt, *The Active Veto of the Large Underground Xenon Detector and the Study of Muons Deep Underground*. PhD thesis, South Dakota School of Mines and Technology, 2018.

[81] D. S. Akerib, P. A. Terman, D. R. Tiedt, W. H. To, M. Tripathi, *et al.*, "LUX Trigger Efficiency," *Nuclear Instruments and Methods in Physics Research A*, vol. 908, pp. 401–410, Nov 2018.

[82] MATLAB, *9.7.0.1190202 (R2019b)*. Natick, Massachusetts: The MathWorks Inc., 2018.

[83] I. Antcheva, M. Ballintijn, B. Bellenot, M. Biskup, R. Brun, *et al.*, "ROOT — A C++ Framework for Petabyte Data Storage, Statistical Analysis and Visualization," *Computer Physics Communications*, vol. 180, no. 12, pp. 2499 – 2512, 2009.

[84] G. Van Rossum and F. L. Drake Jr, *Python Reference Manual*. Centrum voor Wiskunde en Informatica Amsterdam, 1995.

[85] D. S. Akerib, H. M. Araújo, K. Kazkaz, C. Nehrkorn, P. A. Terman, *et al.*, "Improved Limits on Scattering of Weakly Interacting Massive Particles from Reanalysis of 2013 LUX Data," *Physical Review Letters*, vol. 116, p. 161301, Apr 2016.

[86] J. J. Chapman, *First WIMP Search Results from the LUX Dark Matter Experiment*. PhD thesis, Brown University, 2014.

[87] V. N. Solovov, V. A. Belov, F. Neves, C. Silva, C. Thorne, *et al.*, "Position Reconstruction in a Dual Phase Xenon Scintillation Detector," *IEEE Transactions on Nuclear Science*, vol. 59, pp. 3286–3293, Dec 2012.

[88] M. Aglietta, P. Antonioli, G. Badino, C. Castagnoli, A. Castellina, *et al.*, "Search for Fractionally Charged Particles in the Mont Blanc LSD Scintillation Detector," *Astroparticle Physics*, vol. 2, no. 1, pp. 29 – 34, 1994.

[89] S. D. McDermott, H. B. Yu, and K. M. Zurek, "Turning Off the Lights: How Dark is Dark Matter?," *Physical Review D*, vol. 83, p. 063509, Mar 2011.

[90] R. Agnese, S. A. Hertel, K. Prasad, R. Mahapatra, J. Sander, *et al.*, "First Direct Limits on Lightly Ionizing Particles with Electric Charge Less Than $e/6$," *Physical Review Letters*, vol. 114, p. 111302, Mar 2015.

[91] S. I. Alvis, I. J. Arnquist, F. T. Avignone, A. S. Barabash, C. J. Barton, *et al.*, "First Limit on the Direct Detection of Lightly Ionizing Particles for Electric Charge as Low as $e/1000$ with the Majorana Demonstrator," *Physical Review Letters*, vol. 120, p. 211804, May 2018.

[92] S. Davidson, B. Campbell, and D. Bailey, "Limits on Particles of Small Electric Charge," *Physical Review D*, vol. 43, pp. 2314–2321, Apr 1991.

[93] R. Akers, G. Alexander, J. Allison, K. Ametewee, K. J. Anderson, *et al.*, "Search for Heavy Charged Particles and for Particles with Anomalous Charge in e^+e^- Collisions at LEP," *Zeitschrift für Physik C Particles and Fields*, vol. 67, pp. 203–211, Jun 1995.

[94] S. Davidson, S. Hannestad, and G. Raffelt, "Updated Bounds on Milli-Charged Particles," *Journal of High Energy Physics*, vol. 2000, p. 003, May 2000.

[95] S. Chatrchyan, V. Khachatryan, A. M. Sirunyan, A. Tumasyan, W. Adam, *et al.*, "Search for Fractionally Charged Particles in pp Collisions at $\sqrt{s} = 7$ TeV," *Physical Review D*, vol. 87, p. 092008, May 2013.

[96] A. A. Prinz, R. Baggs, J. Ballam, S. Ecklund, C. Fertig, *et al.*, "Search for Millicharged Particles at SLAC," *Physical Review Letters*, vol. 81, pp. 1175–1178, Aug 1998.

[97] R. Mohapatra and S. Nussinov, "Electric Charge Nonconservation and Minicharged Partciles- Phenomenological Implications," *International Journal of Modern Physics A*, vol. 07, no. 16, pp. 3817–3834, 1992.

[98] K. S. Babu and R. R. Volkas, "Bounds on Minicharged Neutrinos in the Minimal Standard Model," *Physical Review D*, vol. 46, pp. R2764–R2768, Oct 1992.

[99] A. I. Studenikin, "New Bounds on Neutrino Electric Millicharge from Limits on Neutrino Magnetic Moment," *Europhysics Letters*, vol. 107, p. 21001, Jul 2014.

[100] A. Badertscher, P. Crivelli, W. Fetscher, U. Gendotti, S. N. Gninenko, *et al.*, "Improved Limit on Invisible Decays of Positronium," *Physical Review D*, vol. 75, p. 032004, Feb 2007.

[101] J. Jaeckel, M. Jankowiak, and M. Spannowsky, "LHC Probes the Hidden Sector," *Physics of the Dark Universe*, vol. 2, pp. 111–117, Sep 2013.

[102] M. Mori, Y. Oyama, A. Suzuki, K. Takahashi, M. Yamada, *et al.*, "Search for Fractionally Charged Particles in Kamiokande II," *Physical Review D*, vol. 43, pp. 2843–2846, May 1991.

[103] Aglietta, "A Study of the LSD-2 Experiment Background," *Nuclear Physics B - Proceedings Supplements*, vol. 14, no. 2, pp. 205 – 209, 1990.

[104] M. Aglietta, P. Antonioli, G. Badino, G. Bologna, C. Castagnoli, *et al.*, "Limits on Low-Energy Neutrino Fluxes with the Mont Blanc Liquid Scintillator Detector," *Astroparticle Physics*, vol. 1, no. 1, pp. 1 – 9, 1992.

[105] K. S. Hirata, T. Kajita, M. Koshiba, M. Nakahata, Y. Oyama, *et al.*, "Observation in the Kamiokande-II Detector of the Neutrino Burst from Supernova SN1987A," *Physical Review D*, vol. 38, pp. 448–458, Jul 1988.

[106] M. Ambrosio, R. Antolini, R. Assiro, G. Auriemma, R. Webb, *et al.*, "The MACRO Detector at Gran Sasso," *Nuclear Instruments and Methods in Physics Research Section A: Accelerators, Spectrometers, Detectors and Associated Equipment*, vol. 486, no. 3, pp. 663 – 707, 2002.

[107] M. Ambrosio, R. Antolini, G. Auriemma, D. Bakari, R. Webb, *et al.*, "Search for Lightly Ionizing Particles with the MACRO Detector," *Physical Review D*, vol. 62, p. 052003, Aug 2000.

[108] R. Agnese, A. J. Anderson, R. Mahapatra, K. Prasad, J. Sander, *et al.*, "Improved WIMP-Search Reach of the CDMS II Germanium Data," *Physical Review D*, vol. 92, p. 072003, Oct 2015.

[109] S. Banik, "Simulation of Energy Deposition of Lightly Ionizing Particles in GEANT4," *DAE Symposium on Nuclear Physics*, vol. 62, pp. 732–733, Dec 2017.

[110] N. Abgrall, E. Aguayo, I. Avignone, F. T., A. S. Barabash, F. E. Bertrand, *et al.*, "The MAJORANA DEMONSTRATOR Neutrinoless Double-Beta Decay Experiment," *arXiv e-prints*, p. arXiv:1308.1633, Aug 2013.

[111] D. S. Akerib, M. Szydagis, J. Thomson, M. Tripathi, J. R. Verbus, *et al.*, "LUXSim: A Component-Centric Approach to Low-Background Simulations," *Nuclear Instruments and Methods in Physics Research A*, vol. 675, pp. 63–77, May 2012.

[112] S. Agostinelli, J. Allison, K. Amako, J. Apostolakis, H. Araujo, *et al.*, "Geant4 - A Simulation Toolkit," *Nuclear Instruments and Methods in Physics Research Section A: Accelerators, Spectrometers, Detectors and Associated Equipment*, vol. 506, no. 3, pp. 250 – 303, 2003.

[113] M. Szydagis, A. Fyhrie, D. Thorngren, and M. Tripathi, "Enhancement of NEST Capabilities for Simulating Low-Energy Recoils in Liquid Xenon," *Journal of Instrumentation*, vol. 8, p. C10003, Oct 2013.

[114] V. Kudryavtsev, "Muon Simulation Codes MUSIC and MUSUN for Underground Physics," *Computer Physics Communications*, vol. 180, pp. 339–346, Oct 2008.

[115] A. Katre, *Searches for Magnetic Monopoles and Highly Ionising Particles at $\sqrt{s} = 8$ TeV at the LHC*. PhD thesis, Universitè de Genevé, 2017.

[116] D. E. Gromm, N. V. Mokhov, and S. I. Striganov, "Muon Stopping Power and Range Tables 10 MeV - 100 TeV," *Atomic Data and Nuclear Data Tables*, vol. 78, no. 2, pp. 183 – 356, 2001.

[117] D. Akerib, M. Szydagis, P. Terman, R. Webb, J. Xu, *et al.*, "Investigation of Background Electron Emission in the LUX Detector," *arXiv e-prints*, p. arXiv:2004.07791, Apr 2020.

[118] G. R. Araujo, T. Pollmann, and A. Ulrich, "Photoluminescence Response of Acrylic (PMMA) and Polytetrafluoroethylene (PTFE) to Ultraviolet Light," *European Physical Journal C*, vol. 79, p. 653, Aug 2019.

[119] B. Tennyson, *Two-Phase Liquid-Gas Xenon Time Projection Chambers: Theory, Applications, and Analysis*. PhD thesis, Yale University, 2017.

[120] P. A. Lachenbruch and M. Goldstein, "Discriminant Analysis," *Biometrics*, vol. 35, no. 1, pp. 69–85, 1979.

[121] S. Kravitz, *Identification of Single Barium Atoms with Resonance Ionization Mass Spectroscopy for the nEXO Neutrinoless Double Beta Decay Experiment*. PhD thesis, Stanford University, 2017.

[122] F. Pedregosa, G. Varoquaux, A. Gramfort, V. Michel, B. Thirion, *et al.*, "Scikit-learn: Machine Learning in Python," *Journal of Machine Learning Research*, vol. 12, pp. 2825–2830, 2011.

[123] K. Kamdin. Personal communication to LUX LIP group, Jul 2018.

[124] G. J. Feldman and R. D. Cousins, "Unified Approach to the Classical Statistical Analysis of Small Signals," *Physical Review D*, vol. 57, p. 3873–3889, Apr 1998.

APPENDIX A

SUMMARY OF PROCESSED ACQUISITIONS

The initial aim of the LIP search was to include all of Run03, and process all Run03 WIMP search acquisitions with 100 pulses and the SRP program. For unknown reasons, a sizable number of the acquisitions did not receive the 100 pulse processing. A potential cause was that the acquisitions failed the initial 100 pulse processing and were not reprocessed thereafter. The loss amounts to approximately 13.6 live days of data, and would have brought the expanded Run03 livetime to almost 100 days. Any acquisition not processed with 100 pulses could not be used as a candidate for SRP; thus, those acquisitions did not have $chopping$ and were excluded from the LIP search. Any data acquisition which received 100 pulse reprocessing (and SRP) will have a unique cp number assigned to it. A number of high rate CH_3T calibration events did receive 100 pulse processing and SRP, but because one could not separate any potential signal coincident with one or more CH_3T events, the LIP search also excluded the high rate CH_3T acquisitions. However, low rate Kr and CH_3T which were later deemed usable for the WIMP search were also included in the LIP search. The following table specifies the acquisition name, its unique cp number if the acquisition had been processed with 100 pulses and SRP, the collection type specifying if it was background or a calibration source initially, and whether or not the LIP search made use of the acquisition.

Acquisition	100 Pulse CP	Collection Type	Used
lux10_20130423T1410	cp26960	Background	Yes
lux10_20130423T1806	cp26961	Background	Yes
lux10_20130423T2231	cp26962	Background	Yes
lux10_20130424T0623	cp26963	Background	Yes
lux10_20130424T1027	cp26964	Background	Yes
lux10_20130424T1236	cp26965	Background	Yes

Continued

Acquisition	100 Pulse CP	Collection Type	Used
lux10_20130424T1315	cp26966	Background	Yes
lux10_20130424T1406		Background	No
lux10_20130424T1740		Background	No
lux10_20130424T2231	cp26967	Background	Yes
lux10_20130425T1017	cp26968	Background	Yes
lux10_20130425T1047		Background	No
lux10_20130425T1530	cp26969	Background	Yes
lux10_20130425T2253	cp26970	Background	Yes
lux10_20130426T0636	cp26971	Background	Yes
lux10_20130426T0951		Background	No
lux10_20130426T1019	cp26972	Background	Yes
lux10_20130426T1625	cp26973	Background	Yes
lux10_20130426T2325	cp26974	Background	Yes
lux10_20130427T0732	cp27027	Background	Yes
lux10_20130427T1042	cp27028	Background	Yes
lux10_20130428T0050	cp27029	Background	Yes
lux10_20130428T0851	cp27030	Background	Yes
lux10_20130428T1554	cp26979	Background	Yes
lux10_20130428T2333	cp27031	Background	Yes
lux10_20130429T0625	cp27032	Background	Yes
lux10_20130429T1447	cp27033	Background	Yes
lux10_20130429T2108	cp27034	Background	Yes
lux10_20130430T0126	cp27035	Background	Yes
lux10_20130430T0808	cp27036	Background	Yes

Continued

Acquisition	100 Pulse CP	Collection Type	Used
lux10_20130430T0851		Background	No
lux10_20130430T0953	cp26986	Background	Yes
lux10_20130430T1714	cp27037	Background	Yes
lux10_20130501T0024	cp26988	Background	Yes
lux10_20130501T0621		Background	No
lux10_20130501T0943	cp26989	Background	Yes
lux10_20130501T1148	cp26990	Background	Yes
lux10_20130501T1336	cp26991	Background	Yes
lux10_20130501T1508		Background	No
lux10_20130501T2037	cp26992	Background	Yes
lux10_20130502T1403	cp26993	Background	Yes
lux10_20130502T1536	cp26994	Background	Yes
lux10_20130502T2051	cp26995	Background	Yes
lux10_20130502T2250	cp26996	Background	Yes
lux10_20130503T0654	cp26997	Background	Yes
lux10_20130503T1457		Background	No
lux10_20130503T2002	cp26998	Background	Yes
lux10_20130503T2359	cp26999	Background	Yes
lux10_20130504T0835		Background	No
lux10_20130504T1527		Background	No
lux10_20130504T2355	cp27000	Background	Yes
lux10_20130505T0712		Background	No
lux10_20130505T1517	cp27001	Background	Yes
lux10_20130505T2310		Background	No

Continued

Acquisition	100 Pulse CP	Collection Type	Used
lux10_20130506T0612	cp27002	Background	Yes
lux10_20130506T1328		Background	No
lux10_20130506T1658	cp27003	Background	Yes
lux10_20130506T2323	cp27004	Background	Yes
lux10_20130507T0633		Background	No
lux10_20130507T1441	cp27005	Background	Yes
lux10_20130507T2253	cp27006	Background	Yes
lux10_20130508T0702	cp27007	Background	Yes
lux10_20130508T1511		Background	No
lux10_20130508T2244		Background	No
lux10_20130509T0703	cp27008	Background	Yes
lux10_20130509T1237	cp27009	Background	Yes
lux10_20130509T1840	cp27010	Background	Yes
lux10_20130509T2301	cp27011	Background	Yes
lux10_20130510T0703	cp27012	Background	Yes
lux10_20130511T0014		Background	No
lux10_20130511T0826	cp27013	Background	Yes
lux10_20130511T1651	cp27014	Background	Yes
lux10_20130511T2308	cp27015	Background	Yes
lux10_20130512T1026	cp27016	Background	Yes
lux10_20130512T1837	cp27017	Background	Yes
lux10_20130512T2258	cp27018	Background	Yes
lux10_20130513T0656	cp27019	Background	Yes
lux10_20130513T1144	cp27020	Background	Yes

Continued

Acquisition	100 Pulse CP	Collection Type	Used
lux10_20130513T2120	cp27021	Background	Yes
lux10_20130513T2258		Background	No
lux10_20130514T0707	cp27022	Background	Yes
lux10_20130514T1153	cp27023	Background	Yes
lux10_20130514T1208	cp27024	Background	Yes
lux10_20130514T1951	cp27025	Background	Yes
lux10_20130514T2359	cp27026	Background	Yes
lux10_20130515T0811	cp26812	Background	Yes
lux10_20130515T1616	cp26813	Background	Yes
lux10_20130515T2232	cp26814	Background	Yes
lux10_20130516T0630	cp26815	Background	Yes
lux10_20130516T1036	cp26816	Background	Yes
lux10_20130516T1841	cp26817	Background	Yes
lux10_20130516T2254	cp26818	Background	Yes
lux10_20130517T0649	cp26819	Background	Yes
lux10_20130517T0942	cp26820	Background	Yes
lux10_20130517T1251	cp26821	Background	Yes
lux10_20130517T1810	cp26806	Background	Yes
lux10_20130517T2315	cp26822	Background	Yes
lux10_20130518T0648	cp26823	Background	Yes
lux10_20130518T1115	cp26824	Background	Yes
lux10_20130518T1748	cp26825	Background	Yes
lux10_20130518T2309	cp26826	Background	Yes
lux10_20130519T0649	cp26869	Background	Yes

Continued

Acquisition	100 Pulse CP	Collection Type	Used
lux10_20130519T1602	cp26827	Background	Yes
lux10_20130519T2247	cp26828	Background	Yes
lux10_20130520T0422	cp26868	Background	Yes
lux10_20130520T1100	cp26853	Background	Yes
lux10_20130520T1218	cp26856	Background	Yes
lux10_20130520T1909	cp26807	Background	Yes
lux10_20130520T2306	cp26863	Background	Yes
lux10_20130521T0654	cp26859	Background	Yes
lux10_20130521T1458	cp26844	Background	Yes
lux10_20130521T2321	cp26850	Background	Yes
lux10_20130522T0747	cp26836	Background	Yes
lux10_20130522T1623	cp26846	Background	Yes
lux10_20130522T2313	cp26855	Background	Yes
lux10_20130523T0748	cp26841	Background	Yes
lux10_20130523T1842	cp26835	Background	Yes
lux10_20130523T2321	cp26843	Background	Yes
lux10_20130524T0742	cp26837	Background	Yes
lux10_20130524T0842	cp26867	Background	Yes
lux10_20130524T1037	cp26851	Background	Yes
lux10_20130524T1829	cp26810	Background	Yes
lux10_20130524T2314	cp26830	Background	Yes
lux10_20130525T0743	cp26829	Background	Yes
lux10_20130525T1504	cp26858	Background	Yes
lux10_20130525T2328	cp26831	Background	Yes

Continued

Acquisition	100 Pulse CP	Collection Type	Used
lux10_20130526T0746	cp26861	Background	Yes
lux10_20130526T1626	cp26862	Background	Yes
lux10_20130526T2333	cp26847	Background	Yes
lux10_20130527T0810	cp26838	Background	Yes
lux10_20130527T1635	cp26854	Background	Yes
lux10_20130527T2321	cp26832	Background	Yes
lux10_20130528T0653	cp26834	Background	Yes
lux10_20130528T1304	cp26808	Background	Yes
lux10_20130528T1546	cp26809	Background	Yes
lux10_20130528T2230	cp26839	Background	Yes
lux10_20130529T0617	cp26842	Background	Yes
lux10_20130529T1105	cp26840	Background	Yes
lux10_20130529T1337	cp26866	Background	Yes
lux10_20130529T1418	cp26865	Background	Yes
lux10_20130529T2003	cp26811	Background	Yes
lux10_20130529T2323	cp26845	Background	Yes
lux10_20130530T0745	cp26852	Background	Yes
lux10_20130530T1407	cp26864	Background	Yes
lux10_20130530T2214	cp26833	Background	Yes
lux10_20130531T0029	cp26848	Background	Yes
lux10_20130531T0620	cp26857	Background	Yes
lux10_20130531T0822	cp26860	Background	Yes
lux10_20130531T2227	cp26849	Background	Yes
lux10_20130601T0502	cp27038	Background	Yes

Continued

Acquisition	100 Pulse CP	Collection Type	Used
lux10_20130601T1300	cp27039	Background	Yes
lux10_20130601T1951	cp27040	Background	Yes
lux10_20130602T0052	cp27041	Background	Yes
lux10_20130602T0701	cp27042	Background	Yes
lux10_20130602T1401	cp27043	Background	Yes
lux10_20130602T2318	cp27044	Background	Yes
lux10_20130603T0725	cp27045	Background	Yes
lux10_20130603T1429	cp27046	Background	Yes
lux10_20130603T2218	cp27047	Background	Yes
lux10_20130604T0355	cp27048	Background	Yes
lux10_20130604T1239	cp27049	Background	Yes
lux10_20130604T1737	cp27050	Background	Yes
lux10_20130604T2137	cp27051	Background	Yes
lux10_20130604T2334	cp27052	Background	Yes
lux10_20130605T0835	cp27053	Background	Yes
lux10_20130605T1539	cp27054	Background	Yes
lux10_20130605T2138	cp27055	Background	Yes
lux10_20130606T0257	cp27056	Background	Yes
lux10_20130606T0953	cp27057	Background	Yes
lux10_20130606T1710	cp27415	Background	Yes
lux10_20130607T0658	cp27059	Background	Yes
lux10_20130607T1834	cp27060	Background	Yes
lux10_20130608T0247	cp27061	Background	Yes
lux10_20130608T1058	cp27062	Background	Yes

Continued

Acquisition	100 Pulse CP	Collection Type	Used
lux10_20130608T1904	cp27063	Background	Yes
lux10_20130609T0321	cp27064	Background	Yes
lux10_20130609T1140	cp27065	Background	Yes
lux10_20130609T2008	cp27066	Background	Yes
lux10_20130610T0424	cp27067	Background	Yes
lux10_20130610T1336	cp27068	Background	Yes
lux10_20130610T1518	cp27069	Background	Yes
lux10_20130610T2151	cp27070	Background	Yes
lux10_20130611T0605	cp27071	Background	Yes
lux10_20130611T1451	cp27072	Background	Yes
lux10_20130611T2234	cp27073	Background	Yes
lux10_20130612T0724	cp27074	Background	Yes
lux10_20130612T1551	cp27076	Background	Yes
lux10_20130612T2217	cp27077	Background	Yes
lux10_20130613T0637	cp27078	Background	Yes
lux10_20130613T1533	cp27079	Background	Yes
lux10_20130613T2123	cp27080	Background	Yes
lux10_20130614T0522	cp27081	Background	Yes
lux10_20130614T1035	cp27082	Background	Yes
lux10_20130614T1623	cp27083	Background	Yes
lux10_20130614T1631	cp27084	Background	Yes
lux10_20130614T1649	cp27085	Background	Yes
lux10_20130614T2217	cp27086	Background	Yes
lux10_20130615T0800	cp27087	Background	Yes

Continued

Acquisition	100 Pulse CP	Collection Type	Used
lux10_20130615T1609		Background	No
lux10_20130615T2230		Background	No
lux10_20130616T0658		Background	No
lux10_20130616T1533		Background	No
lux10_20130616T2157		Background	No
lux10_20130617T0628		Background	No
lux10_20130617T1455		Background	No
lux10_20130617T1457		Background	No
lux10_20130617T2200		Background	No
lux10_20130618T0619		Background	No
lux10_20130618T1442		Background	No
lux10_20130618T2158		Background	No
lux10_20130619T0613		Background	No
lux10_20130619T1451		Background	No
lux10_20130620T0045		Background	No
lux10_20130620T0912		Background	No
lux10_20130620T1138		Background	No
lux10_20130620T1631		Background	No
lux10_20130620T2233		Background	No
lux10_20130621T0639		Background	No
lux10_20130621T1341		Background	No
lux10_20130621T1533		Background	No
lux10_20130622T0033		Background	No
lux10_20130622T0933		Background	No

Continued

Acquisition	100 Pulse CP	Collection Type	Used
lux10_20130622T1526		Background	No
lux10_20130622T2320		Background	No
lux10_20130623T0550		Background	No
lux10_20130623T1522		Background	No
lux10_20130623T2335		Background	No
lux10_20130624T0902		Background	No
lux10_20130626T1028		Background	No
lux10_20130626T1517		Background	No
lux10_20130626T2342		Background	No
lux10_20130627T0814		Background	No
lux10_20130627T1611		Background	No
lux10_20130627T2313		Background	No
lux10_20130628T0652		Background	No
lux10_20130628T0819		Background	No
lux10_20130628T1008	cp27090	Background	Yes
lux10_20130628T1338	cp27092	Background	Yes
lux10_20130628T1444		Background	No
lux10_20130629T0000	cp27094	Background	Yes
lux10_20130629T0855	cp27095	Background	Yes
lux10_20130629T1741	cp27096	Background	Yes
lux10_20130629T2327	cp27097	Background	Yes
lux10_20130630T0916	cp27226	Background	Yes
lux10_20130630T1720	cp27115	Background	Yes
lux10_20130701T0003	cp27224	Background	Yes

Continued

Acquisition	100 Pulse CP	Collection Type	Used
lux10_20130701T0618	cp27121	Background	Yes
lux10_20130701T1646	cp27112	Background	Yes
lux10_20130701T2257	cp27117	Background	Yes
lux10_20130702T0637	cp27227	Background	Yes
lux10_20130702T1040	cp27100	Background	Yes
lux10_20130702T1745	cp27105	Background	Yes
lux10_20130702T2326	cp27118	Background	Yes
lux10_20130703T0738	cp27108	Background	Yes
lux10_20130703T1521	cp27103	Background	Yes
lux10_20130703T2351	cp27111	Background	Yes
lux10_20130704T0857	cp27228	Background	Yes
lux10_20130704T1737	cp27107	Background	Yes
lux10_20130704T2327	cp27104	Background	Yes
lux10_20130705T0802	cp27098	Background	Yes
lux10_20130705T1530	cp27110	Background	Yes
lux10_20130705T2323	cp27120	Background	Yes
lux10_20130705T2330	cp27102	Background	Yes
lux10_20130706T0756	cp27101	Background	Yes
lux10_20130706T1615	cp27109	Background	Yes
lux10_20130706T2336	cp27099	Background	Yes
lux10_20130707T0824	cp27114	Background	Yes
lux10_20130707T1624	cp27113	Background	Yes
lux10_20130707T2202	cp27106	Background	Yes
lux10_20130708T0600	cp27119	Background	Yes

Continued

Acquisition	100 Pulse CP	Collection Type	Used
lux10_20130708T1413	cp27116	Background	Yes
lux10_20130708T2204	cp27122	Background	Yes
lux10_20130709T0627	cp27225	Background	Yes
lux10_20130709T1009	cp27128	Background	Yes
lux10_20130709T1811	cp27130	Background	Yes
lux10_20130709T2221	cp27131	Background	Yes
lux10_20130710T0631	cp27129	Background	Yes
lux10_20130710T1528	cp27132	Background	Yes
lux10_20130710T2313	cp27133	Background	Yes
lux10_20130711T0715	cp27134	Background	Yes
lux10_20130711T1532	cp27135	Background	Yes
lux10_20130711T2157	cp27136	Background	Yes
lux10_20130712T0600	cp27137	Background	Yes
lux10_20130712T1209	cp27138	Background	Yes
lux10_20130712T1351	cp27139	Background	Yes
lux10_20130712T1427	cp27313	Background	Yes
lux10_20130712T2232	cp27312	Background	Yes
lux10_20130713T0631	cp27311	Background	Yes
lux10_20130713T1446	cp27310	Background	Yes
lux10_20130713T2217	cp27309	Background	Yes
lux10_20130716T2014	cp27308	Background	Yes
lux10_20130717T0007	cp27307	Background	Yes
lux10_20130717T0845	cp27306	Background	Yes
lux10_20130717T1424	cp27305	Background	Yes

Continued

Acquisition	100 Pulse CP	Collection Type	Used
lux10_20130717T2212	cp27293	Background	Yes
lux10_20130718T0553	cp27292	Background	Yes
lux10_20130718T1158	cp27291	Background	Yes
lux10_20130718T1629	cp27288	Background	Yes
lux10_20130718T2203	cp27287	Background	Yes
lux10_20130719T1007	cp27286	Background	Yes
lux10_20130720T1908	cp27285	Background	Yes
lux10_20130720T2215	cp27284	Background	Yes
lux10_20130721T0618		Background	No
lux10_20130721T1409	cp27283	Background	Yes
lux10_20130721T2211	cp27282	Background	Yes
lux10_20130722T0633		Background	No
lux10_20130722T1626	cp27281	Background	Yes
lux10_20130722T2238	cp27280	Background	Yes
lux10_20130723T0641	cp27279	Background	Yes
lux10_20130723T1452	cp27278	Background	Yes
lux10_20130723T2205	cp27277	Background	Yes
lux10_20130724T0654	cp27276	Background	Yes
lux10_20130724T1520	cp27275	Background	Yes
lux10_20130724T2301	cp27274	Background	Yes
lux10_20130725T0724	cp27273	Background	Yes
lux10_20130725T1520	cp27272	Background	Yes
lux10_20130725T2233	cp27271	Background	Yes
lux10_20130726T0617	cp27270	Background	Yes

Continued

Acquisition	100 Pulse CP	Collection Type	Used
lux10_20130726T0830	cp27269	Background	Yes
lux10_20130726T1224	cp27268	Background	Yes
lux10_20130726T1431	cp27267	Background	Yes
lux10_20130726T1819	cp27266	Background	Yes
lux10_20130727T0000	cp27265	Background	Yes
lux10_20130727T0803	cp27264	Background	Yes
lux10_20130727T1112	cp27263	Background	Yes
lux10_20130727T1655	cp27290	Background	Yes
lux10_20130728T0055	cp27257	Background	Yes
lux10_20130728T0915	cp27255	Background	Yes
lux10_20130728T1825	cp27254	Background	Yes
lux10_20130728T2255	cp27253	Background	Yes
lux10_20130729T0635	cp27252	Background	Yes
lux10_20130729T1004	cp27251	Background	Yes
lux10_20130729T1752	cp27250	Background	Yes
lux10_20130729T2337	cp27249	Background	Yes
lux10_20130730T0803	cp27248	Background	Yes
lux10_20130730T1532	cp27247	Background	Yes
lux10_20130730T2321	cp27246	Background	Yes
lux10_20130731T0700	cp27245	Background	Yes
lux10_20130731T1524		Background	No
lux10_20130731T2254		Background	No
lux10_20130801T0659	cp27244	Background	Yes
lux10_20130801T1528		Background	No

Continued

Acquisition	100 Pulse CP	Collection Type	Used
lux10_20130801T1901	cp27243	Background	Yes
lux10_20130801T2347	cp27242	Background	Yes
lux10_20130802T0700	cp27241	Background	Yes
lux10_20130802T1440	cp27240	Background	Yes
lux10_20130802T2302	cp27239	Background	Yes
lux10_20130803T0716	cp27238	Background	Yes
lux10_20130803T1751	cp27237	Background	Yes
lux10_20130804T0021	cp27236	Background	Yes
lux10_20130804T0659	cp27235	Background	Yes
lux10_20130804T1322	cp27234	Background	Yes
lux10_20130804T2217	cp27233	Background	Yes
lux10_20130805T0657	cp27232	Background	Yes
lux10_20130805T1529	cp27231	Background	Yes
lux10_20130805T2304	cp27230	Background	Yes
lux10_20130806T0654	cp27229	Background	Yes
lux10_20130806T1442	cp27216	Background	Yes
lux10_20130806T1542	cp27217	Background	Yes
lux10_20130806T2309	cp27218	Background	Yes
lux10_20130807T0650	cp27219	Background	Yes
lux10_20130807T1035	cp27220	Background	Yes
lux10_20130807T1403	cp27221	Background	Yes
lux10_20130807T2233	cp27222	Background	Yes
lux10_20130808T0700	cp27223	Background	Yes
lux10_20130808T1221		CH_3T	No

Continued

Acquisition	100 Pulse CP	Collection Type	Used
lux10_20130808T2134		CH_3T	No
lux10_20130809T0153		CH_3T	No
lux10_20130809T1119		CH_3T	No
lux10_20130809T1934		CH_3T	No
lux10_20130809T2352		CH_3T	No
lux10_20130810T0701		CH_3T	No
lux10_20130810T1500		CH_3T	No
lux10_20130810T2332		CH_3T	No
lux10_20130811T0719		CH_3T	No
lux10_20130811T1531	cp27314	CH_3T	Yes
lux10_20130811T2309	cp27315	CH_3T	Yes
lux10_20130812T0648	cp27316	CH_3T	Yes
lux10_20130812T2259	cp27317	Kr	Yes
lux10_20130813T0652	cp27318	Kr	Yes
lux10_20130813T1120	cp27319	CH_3T	No
lux10_20130813T1909	cp27320	CH_3T	No
lux10_20130814T0044	cp27321	CH_3T	No
lux10_20130814T1008	cp27322	CH_3T	No
lux10_20130814T1712	cp27323	CH_3T	No
lux10_20130815T0204	cp27324	CH_3T	No
lux10_20130815T0818	cp27325	CH_3T	No
lux10_20130815T1052	cp27326	CH_3T	No
lux10_20130815T1531	cp27327	CH_3T	No
lux10_20130816T0024	cp27328	CH_3T	No

Continued

Acquisition	100 Pulse CP	Collection Type	Used
lux10_20130816T0746	cp27329	CH_3T	No
lux10_20130816T1417	cp27330	CH_3T	No
lux10_20130816T2338	cp27331	CH_3T	No
lux10_20130817T0802	cp27332	CH_3T	No
lux10_20130817T1609	cp27333	CH_3T	No
lux10_20130817T2300	cp27334	CH_3T	Yes
lux10_20130818T0740	cp27335	CH_3T	Yes
lux10_20130818T1516	cp27336	CH_3T	Yes
lux10_20130818T2305	cp27337	CH_3T	Yes
lux10_20130819T0744	cp27338	CH_3T	Yes
lux10_20130819T1514	cp27339	CH_3T	Yes
lux10_20130819T1734	cp27340	CH_3T	Yes
lux10_20130819T2254	cp27341	CH_3T	Yes
lux10_20130820T0753	cp27342	CH_3T	Yes
lux10_20130820T0959	cp27343	CH_3T	Yes
lux10_20130820T1222	cp27344	CH_3T	Yes
lux10_20130820T2231	cp27345	CH_3T	Yes
lux10_20130821T0749	cp27346	CH_3T	Yes
lux10_20130821T1522	cp27347	CH_3T	Yes
lux10_20130821T2123	cp27348	CH_3T	Yes
lux10_20130822T0528	cp27349	CH_3T	Yes
lux10_20130822T1100	cp27350	CH_3T	Yes
lux10_20130822T1945	cp27351	CH_3T	Yes
lux10_20130822T2101	cp27352	CH_3T	Yes

Continued

Acquisition	100 Pulse CP	Collection Type	Used
lux10_20130823T0544	cp27353	CH_3T	Yes
lux10_20130823T0953	cp27354	Kr	Yes
lux10_20130823T1717	cp27378	Kr	Yes
lux10_20130823T2119	cp27356	Kr	Yes
lux10_20130824T0533	cp27357	CH_3T	Yes
lux10_20130824T1339	cp27358	CH_3T	Yes
lux10_20130824T2202	cp27359	CH_3T	Yes
lux10_20130825T0627	cp27360	CH_3T	Yes
lux10_20130825T1432	cp27361	CH_3T	Yes
lux10_20130825T2144	cp27362	CH_3T	Yes
lux10_20130826T0551	cp27363	CH_3T	Yes
lux10_20130826T1341	cp27364	CH_3T	Yes
lux10_20130826T2148	cp27365	CH_3T	Yes
lux10_20130827T0537	cp27366	CH_3T	Yes
lux10_20130827T1532	cp27367	CH_3T	Yes
lux10_20130827T2132	cp27368	CH_3T	Yes
lux10_20130828T0700	cp27369	CH_3T	Yes
lux10_20130828T1440	cp27370	CH_3T	Yes
lux10_20130828T2107	cp27371	CH_3T	Yes
lux10_20130829T0554	cp27372	CH_3T	Yes
lux10_20130830T0806	cp27373	Background	Yes
lux10_20130831T1005	cp27374	Background	Yes
lux10_20130901T1035	cp27375	Background	Yes

APPENDIX B

IMPORTANCES OF THE 71-PARAMETER BDT

The expanded BDT made use of 71 S2-only parameters calculated by the LIP filter. Below is a short listing of the 71 parameters used for the BDT. The columns of the table list the ranked order, short parameter description, and the percentage weighting said parameter had on the BDT. Other, non-S2-based LIP RQs were not included, nor were any which might bias against electron backgrounds which are not simulated.

Rank	LIP RQ Description	Percentage
1	Longest S2 pulse (chop identifier)	6.43%
2	Track χ^2/DOF	5.08%
3	std of possible θ between each S2	4.53%
4	Max time of S2 in event between 95% to 99% of PA normalized to pulse length	4.03%
5	Min time of S2 in event between 95% to 99% of PA normalized to pulse length	4.02%
6	TL/L_{data}, Track Length to first-last S2 distance ratio	3.95%
7	std of possible ϕ between each S2	3.84%
8	Min time of S2 in event between 1% to 5% of PA normalized to pulse length	3.61%
9	Track angle θ	3.45%
10	Corrected PA of last S2 in event (bottom array)	3.09%
11	std time of S2s event between 1% to 5% of PA normalized to pulse length	2.92%
12	std raw PAPS of S2 pulses having removed largest	2.64%
13	std raw PAPS of S2 pulses	2.50%

Continued

Rank	LIP RQ Description	Percentage
14	EPTL using both arrays	2.47%
15	std distance between S2 pulses	2.34%
16	std time of S2s event between 95% to 99% of PA normalized to pulse length	2.30%
17	std pair θ, between each S2 pulse	1.96%
18	Min PAPS S2 pulse	1.84%
19	std pair ϕ, between each S2 pulse	1.83%
20	PA before the S1	1.62%
21	Max z-score of S2 PA from mean (raw)	1.51%
22	Max time of S2 in event between 1% to 5% of PA normalized to pulse length	1.50%
23	Sum of corrected S2 PA	1.43%
24	Sum of first two S2 PA (bottom array, raw)	1.43%
25	Number of S2 points used to fit track	1.43%
26	Angle of first to last S2 projection from fit line	1.36%
27	Mean pair θ, between each S2 pulse	1.35%
28	Track Length	1.22%
29	How closely the PA distribution appears as from a moyal distribution	1.22%
30	Track χ^2	1.19%
31	Mean raw PAPS of S2 pulses	1.14%
32	Sum of last two S2 PA (bottom array, raw)	1.12%
33	Sum of first two S2 PA (raw)	0.97%
34	Sum of first two S2 PA (corrected)	0.94%
35	Mean pair ϕ, between each S2	0.94%

Continued

Rank	LIP RQ Description	Percentage
36	L_{data}, distance from first to last S2	0.94%
37	std corrected PAPS	0.92%
38	Mean possible ϕ between each S2	0.91%
39	First S2 PA (corrected)	0.77%
40	EPTL using bottom array	0.75%
41	Sum of last two S2 PA (raw)	0.73%
42	Total corrected energy in keV using both arrays	0.73%
43	Corrected S1 energy in keV	0.71%
44	Ratio of the sum of the first two S2 PA to the last two S2 PA	0.61%
45	std S2 PA (raw)	0.60%
46	Mean raw PAPS of S2 pulses having removed largest	0.58%
47	Mean distance between S2 pulses	0.57%
48	Max z-score of S2 PA from mean (corrected)	0.56%
49	PA of largest S1	0.51%
50	Min corrected S2 area (bottom)	0.51%
51	Last S2 PA (corrected)	0.50%
52	Max corrected PAPS of S2 pulses	0.47%
53	First S2 PA (bottom, corrected)	0.46%
54	Mean possible ϕ between each S2 pulse	0.44%
55	std S2 PA (corrected)	0.41%
56	Min S2 PA (corrected)	0.40%
57	Max S2 PA (corrected)	0.39%
58	Sum of last two S2 PA (corrected)	0.37%
59	Max z-score of S2 PA from mean (bottom, corrected)	0.36%

Continued

Rank	LIP RQ Description	Percentage
60	Total corrected energy in keV using bottom array g_2 value	0.33%
61	Raw total energy in keV using both arrays	0.31%
62	Sum of raw S2 PA	0.31%
63	std S2 PA (bottom, corrected)	0.28%
64	Total S2 energy in keV using both arrays	0.26%
65	Track angle ϕ	0.23%
66	Min S2 PA (raw)	0.23%
67	Max S2 PA (bottom, corrected)	0.21%
68	Max raw PAPS of S2 pulses having removed largest	0.19%
69	Max S2 PA (raw)	0.12%
70	Max raw PAPS of S2 pulses	0.11%
71	Sum of corrected S2 PA (bottom)	0.03%